



UNIVERSITÀ
DEGLI STUDI
FIRENZE

PhD in
Atomic and Molecular Photonics

CYCLE XXXIII


COORDINATOR Prof. Francesco S. Cataliotti

ALL-OPTICAL FUNCTIONAL MAPPING OF
THE FORELIMB MOTOR CORTEX REVEALS
TWO DISTINCT GRASPING CORTICAL
REPRESENTATIONS

Academic Discipline (SSD) FIS/03


Doctoral Candidate

Dr. Montagni Elena


(signature)


Supervisor

Dr. Allegra Mascaro Anna Letizia


(signature)

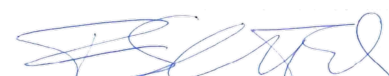
Co-Supervisor

Dr. Resta Francesco


(signature)

Coordinator

Prof. Cataliotti Francesco S.


(signature)

Years 2017/2020

ABSTRACT

The anatomical and functional organization of the motor cortex and its role in forelimb movement control were deeply investigated over the past years. Extensive research showed two spatially segregated functional areas related to forelimb control: the caudal forelimb area (CFA) and the rostral forelimb area (RFA). Many studies suggest that these two areas are a part of a highly integrated computational unit with distinct motor functions. Recently, optogenetic motor mapping revealed that distinct complex movements are related to segregated cortical functional modules. Although studying optogenetically-evoked behaviors already provides a powerful way to investigate the neuronal pathways related to motor output, decoding the functional engagement and interdependence of cortical motor circuits are still two largely unexplored fields. The “all-optical” interrogation of neuronal circuits constitute a successful strategy to causally dissect the functional organization of the motor cortex, since it combines optogenetics and optical indicators to simultaneously record and manipulate the activity of selected neuronal populations using light.

During my Ph.D., I contributed to develop a one-photon all-optical strategy to causally investigate the neuronal activity patterns in RFA and CFA driving optogenetically-evoked complex movements in awake head-fixed mice. To this aim, we first examined four different red-shifted Genetically Encoded Calcium Indicator (GECI), identifying jRCaMP1a as the best indicator for detecting in vivo neuronal activity on multiple cortical areas simultaneously. Then, we combined the widely used blue-sensitive opsin, ChannelRhodopsin2 (ChR2) with jRCaMP1a for detecting in vivo large-scale stimulated cortical dynamics. Once we demonstrated that our one-photon all-optical approach was cross-activation free, we exploited it to causally investigate RFA and CFA cortical activity patterns associated with two optogenetically-evoked complex movements, the grasp-like and the locomotion-like movement. We showed stereotyped and reproducible

spatiotemporal propagation patterns of calcium dynamics per movement category highlighting a direct contribution of defined patterns to complex movement execution. Furthermore, we demonstrated that movement-specific cortical activity maps were bounded on discrete function modules centred on the related light-based motor maps, providing clear evidence of their independent functional organization. Importantly, the visualization of the cortical activity elicited by optogenetic stimulation allowed us to identify a third cortical functional module evoking grasp, which is characterized by segregated large-scale cortical dynamics. We named it Lateral Forelimb Area (LFA).

In conclusion, our one-photon large-scale all-optical system led to a robust classification of the connectivity, independence, and hierarchy of three functional cortical regions involved in performing evoked complex movements. The results obtained during my Ph.D. provide important insights on the physiological interplay of brain activity and motor control which could be further applied to the investigation of the altered cortical activity patterns in pathological conditions.

Content

ABSTRACT	I
CONTENT	III
LIST OF FIGURES.....	V
LIST OF RELEVANT PUBLICATIONS	VII
1. INTRODUCTION	1
1.1. DECONSTRUCTION OF CORTICAL CIRCUITS INVOLVED IN THE CONTROL OF FORELIMB COMPLEX MOVEMENTS	2
1.2. OPTOGENETICS: A NOVEL OPTICAL TOOL FOR FUNCTIONAL MAPPING OF MOTOR CORTEX	8
1.3. SENSORS AND SYSTEMS FOR LARGE-SCALE OPTICAL IMAGING OF NEURONAL ACTIVITY.....	15
1.4. ALL-OPTICAL STRATEGIES FOR FUNCTIONAL MOTOR MAPPING	23
2. METHODS AND PROCEDURES	28
2.1. SURGICAL PROCEDURES.....	29
2.2. WIDE-FIELD MICROSCOPE SETUP	30
2.3. WIDE-FIELD IMAGING IN AWAKE BEHAVING MICE.....	31
2.4. ROBOTIC PLATFORM	32
2.5. OPTOGENETIC STIMULATION	33
2.6. LIGHT-BASED MOTOR MAPPING (LBMM).....	34
2.7. VIDEO TRACKING ANALYSIS	35
2.8. IN VIVO LOCAL FIELD POTENTIAL RECORDING	35
2.9. EX VIVO IMAGING	36
2.10. PHARMACOLOGY TREATMENT	37
2.11. IMAGING DATA ANALYSIS.....	37
2.12. STATISTICAL ANALYSIS.....	42
3. RESULTS.....	43
3.1. CHARACTERIZATION OF FOUR RED-SHIFTED CALCIUM INDICATORS FOR FUNCTIONAL WIDE-FIELD IMAGING.....	44
3.1.1. Stable expression of red-shifted indicators over four weeks	44
3.1.2. In vivo brightness comparison between four red-shifted GECIs.....	46
3.1.3. Characterization of expression profiles on histological brain slices	46
3.1.4. Evaluation of motor task-evoked jRCaMP1a response	50
3.2. DEVELOPMENT OF A CROSSTALK FREE MESOSCALE ALL-OPTICAL SYSTEM.....	54

3.2.1.	Experimental design to perform parallel calcium imaging and light-based motor mapping in awake mice	54
3.2.2.	Wide-field imaging of jRCaMP1a does not ChR2 cross-activation	55
3.2.3.	Stimulation of ChR2 does not induce alteration of jRCaMP1a fluorescence.	58
3.3.	MAPPING MOVEMENT-SPECIFIC SPATIOTEMPORAL CORTICAL ACTIVATION....	62
3.3.1.	Mesoscale movement specific calcium dynamics detected by light-based motor mapping.....	62
3.3.2.	Distinct functional modules are involved in the processing of optogenetically evoked movements within motor cortex.....	63
3.3.3.	Identification of a distinct grasping representation module: The Lateral Forelimb Area (LFA).....	70
3.3.4.	Optogenetically-evoked GRASP RFA and GRASP LFA movements show similar properties.....	75
3.3.5.	Complex movements execution is associated with specific spatiotemporal pattern of activity propagation	76
3.3.6.	Connectivity features associated with evoked complex movements are disrupted by excitatory synaptic block	80
3.3.7.	LFA and RFA are two independent cortical modules	85
4	DISCUSSION	87
4.1.	JRCAMP1A AS THE BEST RED-SHIFTED CALCIUM INDICATOR FOR LARGE-SCALE CORTICAL STUDIES	88
4.2.	ALL-OPTICAL CROSSTALK-FREE MANIPULATION AND READOUT OF CORTICAL DYNAMICS.....	92
4.3.	CORTICAL MODULES ARE NOT FUNCTIONALLY ORGANIZED IN A HIERARCHICAL PREMOTOR-MOTOR ORGANIZATION	94
5	REFERENCES.....	100

List of figures

1.1 ORGANIZATION OF RODENT FRONTAL CORTEX	5
1.2 OPTOGENETIC MOTOR MAPPING.....	12
1.3 GENETICALLY ENCODED OPTICAL INDICATORS	18
1.4 NORMALIZED FLUORESCENCE OPSINS AND GECIS SPECTRA	25
2.1 SCHEMATIC REPRESENTATION OF THE ROBOTIC PLATFORM	32
3.1 EXPERIMENTAL TIMELINE	45
3.2 RED-SHIFTED INDICATORS STABILITY OVER FOUR WEEKS	45
3.3 IN VIVO BRIGHTNESS QUANTIFICATION OF FOUR DIFFERENT RED SHIFTED INDICATORS.....	47
3.4 EX VIVO CHARACTERIZATION OF RED SHIFTED CALCIUM INDICATORS	48
3.5 MOTOR TASK-EVOKED M1 CORTICAL RESPONSE	51
3.6 MOTOR TASK-EVOKED CORTICAL ACTIVITY.....	52
3.7 IN VIVO EXPERIMENTAL DESIGN VALIDATION	56
3.8 IMMUNOHISTOCHEMISTRY QUANTIFICATION.....	57
3.9 CHR2 CROSS-ACTIVATION DURING JRCAMP1A WIDE-FIELD IMAGING	59
3.10 JRCAMP1A CROSS ACTIVATION DURING OPTOGENETIC STIMULATION.....	60
3.11 LARGE SCALE CALCIUM DYNAMICS DURING LIGHT-BASED MOTOR MAPPING ARE MOVEMENT SPECIFIC	64
3.12 CORTICAL DYNAMICS ARE NOT INFLUENCED BY LASER POWER VARIABILITY ACROSS MICE.....	65
3.13 PROCESS FOR OBTAINING THE MOVEMENT SPECIFIC ACTIVITY MAPS (MSAMS)	68
3.14 DISCRETE MODULES OF MOVEMENT-SPECIFIC CORTICAL CONNECTIVITY ARE CENTERED ON THEIR RELATIVE LBMM	69
3.15 IDENTIFICATION OF THE LATERAL FORELIMB AREA (LFA) AS A DISTINCT GRASPING REPRESENTATION MODULE	72
3.16 SPATIAL SEGREGATION OF BOTH LFA LBMM AND MSAM	73
3.18 <i>IN VIVO</i> OPTOGENETICALLY-EVOKED MOVEMENTS.....	77

3.19	OPTOGENETICALLY-EVOKED COMPLEX MOVEMENTS TRAJECTORIES	78
3.20	OPTOGENETICALLY-EVOKED GRASP RFA AND GRASP LFA ARE CHARACTERIZED BY SIMILAR DYNAMICS IN SPACE.....	79
3.21	CORTICAL ACTIVITY PROPAGATION ANALYSIS REVEALS MOVEMENTS-SPECIFIC SPATIOTEMPORAL ACTIVATION MAPS AND FLOW DIRECTION ...	82
3.21	LOCAL CONNECTIVITY IS DISTURBED BY EXCITATORY SYNAPTIC BLOCK.....	83
3.23	EXCITATORY SYNAPTIC BLOCK LEADS TO COMPLEX MOVEMENT INTERFERENCE	84
3.24	LFA GRASPING EXPRESSION IS INDEPENDENT FROM RFA CONNECTIVITY.....	86

List of relevant publications

Some sections of this thesis are also included as part of the following research papers:

- **Montagni Elena**, Resta Francesco, Conti Emilia, Scaglione Alessandro, Pasquini Maria, Micera Silvestro, Allegra Mascaro Anna Letizia, and Pavone Francesco Saverio. 2019. 'Wide-field imaging of cortical neuronal activity with red-shifted functional indicators during motor task execution', *Journal of Physics D: Applied Physics*, 52.
- **Montagni Elena**, Resta Francesco, Allegra Mascaro Anna Letizia, and Pavone Francesco Saverio. 2019. 'Optogenetics in Brain Research: From a Strategy to Investigate Physiological Function to a Therapeutic Tool', *Photonics*, 6.
- Resta Francesco, **Montagni Elena**, de Vito Giuseppe, Scaglione Alessandro, Allegra Mascaro Anna Letizia, and Pavone Francesco Saverio. 'All-optical functional mapping of the forelimb motor cortex discriminates two distinct cortical modules evoking grasp-like movement in awake mice', *under preparation*.

1

Introduction

1.1. Deconstruction of cortical circuits involved in the control of forelimb complex movements

For decades, motor cortex organization and its role in motor control were intensely studied. The earliest evidence that different regions of the cerebral cortex are associated with specific functions was provided by Fritsch and Hitzig in 1870. They found that electrical stimulation of selected regions of the frontal cortex of dogs produced different types of movement, highlighting the role of the motor cortex in movement generation (Gross 2007; Hagner 2012). Further studies discovered that rodent motor cortex shows consistent topographic representations of defined classes of ethologically relevant forelimb-forepaw movements, such as grasp-like movements or forelimb abduction, adduction, extension, retraction and elevation (Bonazzi et al. 2013; Donoghue and Wise 1982; Tennant et al. 2011).

To understand how the motor cortex controls forelimb movement, it is first essential to clarify the anatomical and functional organization of the motor cortex. Anatomically, two distinct motor areas involved in forelimb control were identified in the frontal lobe, the primary (M1) and secondary (M2) motor cortices (Suter and Shepherd 2015) (fig1.1a). Both regions are activated during skilled voluntary movements and their activity is related to defined levels of movement control: from the force needed for a given movement to the integration of sensory feedback (Omrani et al. 2017; Saiki et al. 2014). M1 and M2 are arranged in a hierarchical premotor-motor organization in which the role of M1 is processing concrete motor information and M2 is indirectly involved in movement modulation through the primary motor cortex, such as enabling adaptive choice behavior and linking sensory information to motor actions (Wang et al. 2017; Barthas and Kwan 2017). It should be noted that the same cortical regions may be

named differently across the literature. This condition may lead to conflicting naming schemes, confusing the correspondence between primate and rodent motor areas (Ebbesen et al. 2018). Accordingly, M2 has also been named vibrissae primary motor cortex (vM1), frontal orienting field (FOF) or agranular media area (AGm) and is thought to be homologous to the primate premotor cortex (PM), while M1 also known as agranular lateral area (AGl) is homologous to the primate M1 (Soma et al. 2017; Brecht 2011; Barthas and Kwan 2017).

An alternative representation model of the motor cortex is based on its functional organization. Indeed, the principal body parts of the rodents (forelimb, face and hindlimb) are functionally represented in segregate cortical locations within the motor cortex (Donoghue and Sanes 1988). Based on this criterion, extensive research during the last decades showed two distinct forelimb functional areas, a large caudal forelimb area (CFA) and a smaller rostral forelimb area (RFA), which are spatially separated by topographical representations of other body parts such as trunk, neck and vibrissa (fig1.1b) (Tennant et al. 2011; Ebbesen et al. 2018). Although RFA is thought to be an equivalent of the primate PM and CFA is believed to correspond to the primate M1 (Ebbesen et al. 2018; Hira et al. 2013), many studies suggest that these two areas are a part of a highly integrated computational unit with distinct motor functions rather than a hierarchical premotor-motor organization (Brown and Teskey 2014; Ebbesen et al. 2018). Regardless of their hierarchical status, RFA and CFA are highly involved in the control of complex forelimb movements. The refinement of motor mapping technologies over the years helped to clarify their functional organization, originally investigated with *ex vivo* anatomical tract tracing approaches (Wang et al. 2017). Intracortical microstimulation (ICMS) and surface stimulation with electrode arrays were used to generate or alter motor output pathways (Hosp et al. 2008; Tennant et al. 2011; Mansoori et al. 2014). Interestingly, a variety of different forelimb movements can be elicited by ICMS of rostral and caudal forelimb areas, revealing a somatotopic organization of movements cortical representation (fig1.1c) (Brown and Teskey 2014). Typically, long-duration ICMS

(500ms continuous stimuli) elicit reproducible highly cooperative movements, while short-train stimulations (50ms) evoke brief muscle twitches (Ramanathan et al. 2006; Brown and Teskey 2014; Young et al. 2012; Graziano, et al. 2002). More in detail, long-duration ICMS elicits muscle contraction involving multiple joints, leading to complex movements (Brown and Teskey 2014; Bonazzi et al. 2013). Forelimb- grasping (paw into a grip posture and move to the mouth), retraction, advance or elevation, all belong to this class of movements (fig1.1c) (Brown and Teskey 2014; Ramanathan et al. 2006). Interestingly, complex movements motor mapping using long-duration ICMS revealed that grasping-movement is an exclusive consequence to the RFA stimulation. On the contrary, retraction, advance, or elevation are only elicited by CFA stimulation, highlighting a strong segregation of cortical forelimb representation (fig1.1c) (Brown and Teskey 2014; Singleton 2014). Although there is evidence of a non-localization of grasp movements during development, complex movements cortical representations do not change after motor learning in adult rodents suggesting a consistent and stable functional organization of the motor cortex in adulthood (Ramanathan et al. 2006; Brown and Teskey 2014; Singleton 2014). Previous findings suggested that the RFA and CFA are characterized by two independent circuits which lead to different motor outputs (Brown and Teskey 2014; Karl and Whishaw 2013). This idea was further supported by many studies showing that the output layers of these two areas have independent descending corticospinal projections originating from a subtype of pyramidal tract (PT) neurons, named corticospinal motor neurons (CSN) and mainly localized in layer 5, which send direct projections to the contralateral spinal cord (fig1.1d) (Harris and Shepherd 2015; Baker et al. 2018; Economo et al. 2018). Interestingly, CSNs were also found as a small, circumscribed cluster in a third area in the secondary somatosensory cortex, which has been named PL-CFA (fig1.1d) (Wang et al. 2017; Wise et al. 1979). Depending on the cortical region (RFA, CFA or PL-CFA), CSNs have distinct and parallel spinal cord projections that engage premotor neurons of different muscle groups. Consequently, they are activated during separate phases of voluntary

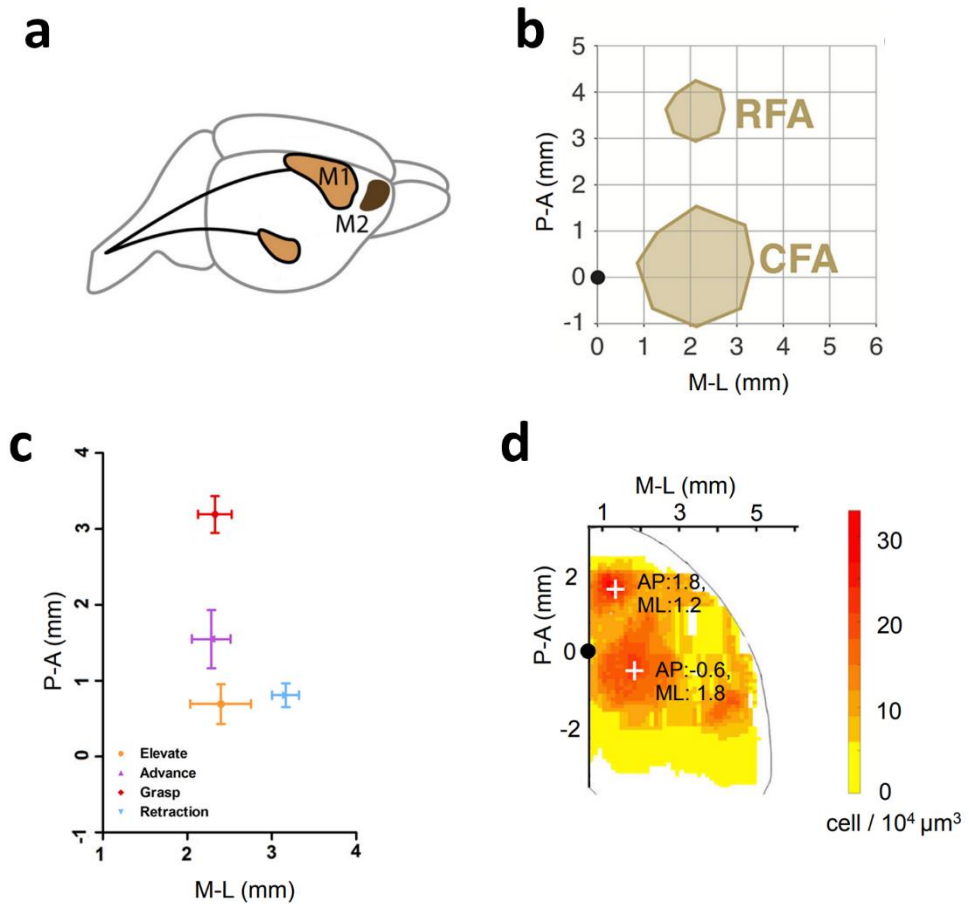


Figure 1.1: Organization of rodent frontal cortex. (a) Schematics anatomical locations of M1 and M2. Adapted with permission from (Suter and Shepherd 2015). (b) RFA and CFA representation evoked by microstimulation. The black dot indicates bregma. Adapted with permission from (Ebbesen et al. 2018). (c) Representative complex movement cortical representation evoked by long-duration ICMS. Individual movements are showed in different colours. Adapted with permission from (Brown and Teskey 2014). (d) Heatmap of CSNs cortical distribution. The crosses show the two CSNs centres of mass with their respective coordinates in black. Bregma indicated by black dot. Adapted with permission from (Wang et al. 2017).

movements. For instance, in the reach-to-grasp movement CFA-CSNs control reaching and RFA-CSNs control grasping (Wang et al. 2017). This result further confirmed the strong spatial segregation of the cortical forelimb representation according to the functions and the positions of the muscles, providing direct evidence of a dual system with parallel features (Wang et al. 2017). Interestingly, PL-CFA CSNs mainly overlap with the RFA-CSNs premotor neurons in the spinal cord (Wang et al. 2017). However, how and if reciprocal cortical connections are required for coordinating complex movements remain a crucial question. Tracking of the asymmetrical functional connections between rodent CFA and RFA was achieved by anatomical tracing in combination with stimulation techniques and electrical recordings. These studies show that RFA receives strong functional projections from layer 2/3 and layer 5a (L5a) of the CFA while CFA receives strong projections from L5b neurons of the RFA (Hira et al. 2013; Kunori and Takashima 2016). These cortico-cortical pathways are involved in the transmission of forelimb-related sensory inputs, which seem to be firstly processed by the CFA (Kunori and Takashima 2016). Moreover, similarly to premotor areas, RFA produces strong modulation of CFA output (Deffeyes et al. 2015). Nevertheless, it should be noted that when rodents participate in voluntary forelimb movements the functional activity (task-related) in CFA- and RFA-neurons is similar, highlighting that the RFA neuron repertoire is functionally correspondent to the CFA neuron repertoire (Hira et al. 2013; Saiki et al. 2014).

Different loss-of-function strategies were applied to further determine the modulatory impact of RFA or CFA on motor outputs and consequently reveal whether forelimb complex movements depend on activation of one or both these two areas. The unilateral lesion, pharmacological inactivation, cooling deactivation, or optogenetic silencing of rodent motor cortex, all result in a loss of movement-evoked cortical representations (Morandell and Huber 2017; Boychuk, et al. 2011). With these tools, researchers showed that simultaneous inactivation of RFA and CFA leads to a deficit in movement execution (Morandell and Huber 2017; Kimura et al. 2017). Interestingly, CFA unilateral inactivation did not

significantly alter the performance of grasping in a task-related movement. Conversely, the inactivation of the RFA alone strongly inhibited task performance, suggesting that RFA plays a crucial role in forelimb movement initiation (Kimura et al. 2017; Brown and Teskey 2014). This finding stands out from other studies which showed that unilateral inhibition of either RFA or CFA led to a deficit in task-related or evoked-movements (Hira et al. 2013; Harrison et al. 2012). Other controversial studies suggested that movement execution deficits were specific to CFA inactivation, thus implying that RFA would not be able to evoke movements in absence of normal CFA (Morandell and Huber 2017). These contrasting results may be partially due to (i) the different approaches for inducing loss-of-function, (ii) the severity of the injury, (iii) the large size of the CFA which could prevent full coverage by the inhibitor. Moreover, it is not yet clear if these alterations are due to a loss of motor control, loss of muscle tone, or sensory feedback changes. Interestingly, silencing CFA / RFA neighbouring areas (like barrel cortex or posterior parietal cortex) did not result in motor execution deficits (Morandell and Huber 2017).

In conclusion, CFA and RFA are both critically involved in controlling movements and intracortical connections between these areas play crucial roles in complex forelimb movement generation. Nevertheless, to what extent CFA and RFA are necessary for movement selection and execution is still a crucial question. An indispensable tool to unravel this issue is optogenetics, that exploits light to manipulate specific neuronal populations. Indeed, optogenetic motor mapping is a minimally invasive approach that can be successfully used to investigate cortical connections between RFA and CFA and consequently to understand their coordination during movements.

1.2. Optogenetics: A novel optical tool for functional mapping of motor cortex

Functional mapping of the motor cortex requires associating a defined motor output pathway to a specific cortical stimulus. Traditionally, electrode-based methods (ICMS and surface stimulation with electrode arrays) have been used to manipulate neuronal circuits. Despite being extensively employed, electrical stimulation is not precise enough to target neuronal subpopulations, additionally, it requires invasive surgery making long-term experiments difficult (Ayling et al. 2009; Harrison et al. 2012).

In the last decade, it has become possible to stimulate neurons over large portions of the cortex using less-invasive techniques based on light (Ayling et al. 2009). Indeed, under appropriate conditions, neuronal circuit activation can be triggered by light, with the advantage of manipulating only defined neuronal populations and without the need for a craniotomy (Silasi et al. 2013; Watanabe et al. 2020). Therefore, optogenetics is becoming the gold standard for circuit manipulation in living organisms.

Optogenetics exploits genetically encoded proteins called opsins to control the activity of targeted cell populations by light. Opsins are a group of light-activated transmembrane proteins of both microbial and animal derivation, which are categorized according to biophysical properties in ion channels, pumps, and G-protein coupled receptors (Kalanithi and Purger 2017; Eickelbeck et al. 2018). Over the last years, bioengineering efforts have made it possible to expand the variety of available opsins allowing different electrochemical responses of the same neuronal circuits, which can now be excited or silenced simply by adjusting the light wavelength applied. The most common opsin used to excite neurons is the blue light-activated nonspecific cation channel Channelrhodopsins 2 (ChR2,

470 nm spectral peak), which is permeable to mono- (Na^+ , K^+ , H^+) and divalent cations (Ca^{2+}). Channelrhodopsins 2 was the first opsin discovered from the unicellular alga *Chlamydomonas reinhardtii* by Georg Nagel and colleagues in 2003 (Eickelbeck et al. 2018; Lin 2011). In parallel, the yellow light-activated anion channel named Halorhodopsin (NpHR, 590nm spectral peak), from *Natronomonas pharaonis*, is the opsin widely used to silence excitable cells (Raimondo et al. 2012).

Optogenetic actuators have subsequently been engineered to optimize selected properties like activation and deactivation kinetics leading to faster, slower, or step function opsins that best meet the increasing experimental requirements. Based on those criteria, many studies during the last decade used a humanized version of ChR2, namely ChR2(H134R), which entails a single point mutation at position H134 (Lin 2011). It is characterized by (i) a modest reduction in desensitization, (ii) a slower channel closing rate, and (iii) a slight increase in light sensitivity than the wild-type (wt) ChR2. These properties allow generating larger photocurrents, but the slower kinetics lead to a less temporally precise indicator than ChR2(wt) (Nagel et al. 2005; Berndt et al. 2011). Moreover, the development of color-tuned chimeras opened the way to multiwavelength optogenetics, that is the simultaneous use of optogenetic actuators with a minimal spectral overlap in the living brain (Prigge et al. 2012; Zhang et al. 2007). The first red-shifted opsin was VChR1 (with maximum absorption at 535nm), from which C1V1 was derived (Guru et al. 2015). Chronos (~500nm) and Chrimson (~590nm) were derived from ChR2 (Klapeotke et al. 2014). Although long-wavelength sensitive opsins allow a less-invasive light delivery due to a reduced scattering and a deeper penetration into scattering tissue, they exhibit some residual absorption of blue light which does not make them optimal for a multimodal, bidirectional control of neuronal circuit in living organisms using two different optogenetic actuators (Guru et al. 2015; Zhang et al. 2007).

Regardless of the opsin used, efficient delivery is crucial for achieving cell type-specific expression. Currently, there are two main strategies: (1) viral vector targeting methods based on AAV or (2) transgenic animal lines.

1) AAV-based brain transduction can be achieved through a variety of delivery routes: direct intraparenchymal injection, intraventricular infusion, and intravenous administration (Li and Daly 2002). The first method is widely used when a small local transfection in a specific brain region is required but suffers from high variability in transduction efficiency (Sheffield, Adoff, and Dombeck 2017; Allegra Mascaro et al. 2019). Intraventricular injections have failed to produce widespread CNS transduction in adult rodents (Warren et al. 1999). The efficiency of intravenous administration is limited by the blood-brain barrier (BBB), which restricts the transport of these vectors to the adult central nervous system (CNS). Consequently, intraventricular and intravenous administration can be successfully applied only in neonatal animals (Foust et al. 2009; Gombash et al. 2014; Li and Daly 2002) .

2) Transgenic lines are endowed with homogeneous protein expression in wide regions of the nervous system (Zeng and Madisen 2012; Hausser 2014). Nevertheless, abnormal axonal morphology has been identified as a possible toxic effect of long-term expression of hexogen proteins in transgenic mice (Miyashita et al. 2013). Moreover, the development of transgenic lines is strictly dependent on the number of available genetic promoters used to drive the process, which is still limited (Montagni et al. 2019).

Another field of the optogenetic deeply investigated regards the opsins excitation strategies, which requires high temporal and spatial precision to finely control neuronal activity. Over the years, two approaches based on one-photon (1P) or two-photon (2P) stimulation have been extensively used. Two-photon (2P) stimulation is used to target single cells or cell compartments below the first layer of the cortex (fig1.2a). Indeed, the scattering properties of biological tissues prevent deeper fluorescence excitation via visible light, unless transparent animals are used (e.g., zebrafish larvae). Two-photon (2P) stimulation uses the simultaneous absorption of two near-infrared photons (usually at 1064 nm) to excite light-sensitive proteins (Helmchen and Denk 2005). Consequently, this technique allows for stimulating deeper in the biological tissue with the additional advantage of the single-cell resolution (Montagni, Resta, Mascaro, et al. 2019;

Papagiakoumou et al. 2013). Alternatively, one-photon (1P) wide-field illumination is the first and most common method to perform optogenetic stimulation using visible light (fig1.2a). Traditionally, it was possible to drive optogenetic stimulation of opsin-expressing neurons in a large field of view (FOV) using an epifluorescent lamp or a light-emitting diode (LED) as a light source (Papagiakoumou 2013). An advantage of 1P illumination is the low-power density required to achieve the minimum level of irradiance to generate action potentials (Packer et al. 2013; Papagiakoumou 2013). At the same time, the low spatial resolution of 1P wide-field illumination does not reach single-cell excitation (Oron et al. 2012). To increase the spatial resolution, the light source can be changed, for example by replacing the LED with micro-LED (μ LED) or laser, which allow to selectively excite a significantly smaller region of interest using light in the visible spectrum (Grossman et al. 2010; Wu et al. 2015). Moreover, in order to perform sequential cortical stimulation patterns with light, spatial excitation sequences are needed. Different approaches are applicable depending on the complexity of the excitation pattern required. Although it does not allow a fast change of the excitation point, the most adaptable and low-cost method is moving the plane in which the animal is positioned (Lim et al. 2014). Instead, a fast point by point spatial control of the laser beam is provided by surface light delivery systems, such as acousto-optic deflectors (AOD) or galvanometer mirrors (Hausser 2014; Conti et al. 2019). This technique is an important resource for mesoscale mapping the functional networks at the cortical level (Silasi et al. 2013; Vanni et al. 2017). Light-based motor mapping (LBMM) penetration is limited by the light scattering from the intact skull to under a few hundred microns ($<1\text{mm}$) from the cortical surface in living animals. The motor map size is often influenced by the stimulation of axons and dendrites from neurons that have the soma outside the activation area (Silasi et al. 2013). Additionally, both the brain state (anesthetized or awake) and the stimulus parameters impact the capacity to evoke movements and correctly identify non-response cortical sites (Silasi et al. 2013; Harrison et al. 2012; Hira et al. 2015). Harrison and colleagues in 2012 showed that prolonged optogenetic

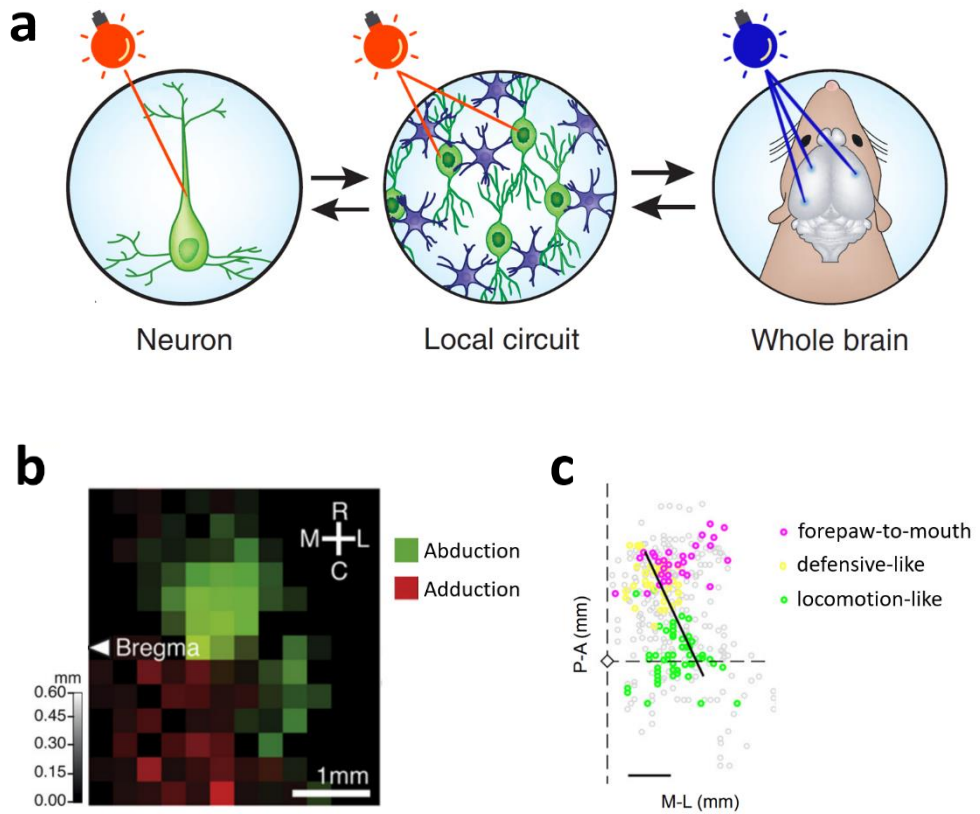


Figure 1.2: Optogenetic motor mapping. (a) Representative image of optogenetic manipulation at different spatial resolution. Left, two-photon (2P) excitation method, which provides temporally precise control of neuronal firing rate. Middle, 2P spatially patterned excitation sequences for mapping and modulating the connectivity of individual neurons within local circuits. Right, One-photon (1P) patterned illumination to trigger extensive cortical network dynamics and mimic natural activity patterns for inter- and intra-cortical interactions investigation. Adapted with permission from (Montagni et al. 2019). (b) Light-based motor map of abduction (green) and adduction (red) movements in anesthetized mice. Adapted with permission from (Harrison et al. 2012). (c) Light-based motor map of three complex movements: forepaw-to-mouth movement (magenta), defensive-like movement (yellow) and locomotion-like movement (green). Adapted with permission from (Hira et al. 2015).

stimulation (500 ms, 100Hz) of excitatory pyramidal neurons in anesthetized and awake mice evoked two reproducible complex movements of the contralateral forelimb, which were divided into two classes depending on the direction of forelimb movement: abduction and adduction (fig1.2b) (Harrison et al. 2012). Three years later, Hira and colleagues found that three types of complex movements were mapped into distinct functional modules in awake mice (fig1.2c) (Hira et al. 2015). They showed that long-train stimulation (500 ms, 2 or 4 ms pulses delivered at 50 Hz) of different motor cortex domains led to (i) forepaw-to-mouth, (ii) defensive-like, or (iii) locomotion-like movements (Hira et al. 2015). Interestingly, in both those studies, the modules required to evoke movements occupied the same cortical territory of mouse CFA and RFA. Nevertheless, these modules often were contiguous and equal in area, while CFA and RFA size are different and separated by representations of other body parts (Tennant et al. 2011; Harrison et al. 2012; Hira et al. 2015). Surprisingly, blocking excitatory cortical synaptic transmission between RFA and CFA did not abolish movements induced by photostimulation of these two functional regions, highlighting the functional and anatomical independence of these two modules (Hira et al. 2015; Harrison et al. 2012). Despite excitatory opsins expressed in excitatory neurons are the main combination used to dissect the role of RFA and CFA, optogenetic loss-of-function experiments played a key role in dissecting the role of forelimb motor representation. Optogenetic silencing of neuronal activity relies on two schemes: ‘silencing by excitation’ which requires the expression of excitatory opsins in inhibitory interneurons, or ‘direct photoinhibition’ involving inhibitory opsins expressed directly in neuron populations to be silenced (Wiegert et al. 2017; Li et al. 2019). Based on those methods, studies showed that termination of inhibitory activity in the sensorimotor cortex was sufficient to drive a full action sequence in skilled mice, demonstrating the necessity and sufficiency of cortical activity for enacting a learned skill (Guo et al. 2015). Additionally, Morandell and colleagues in 2017 studied the effects of single area inactivation (RFA or CFA) in goal-directed actions by performing transcranial optogenetic excitation of cortical

inhibitory interneurons. Their findings “suggest that both areas are involved in processing choice and movement execution in a transient and partially distributed manner” (Morandell and Huber 2017). Although studying optogenetically-evoked behaviors already provides a powerful way to investigate neuronal control of motor output pathways, decoding how optogenetic manipulation affects the dynamic of neuronal circuits in vivo remains an open question. To this aim, optogenetics has been largely combined with neuronal activity readout techniques, such as electroencephalography (EEG) or Local Field Potential (LFP), thus achieving simultaneous readout and manipulation of neuronal circuits (Lee et al. 2019; Zhang et al. 2019; Silasi et al. 2013). A recent revolutionary approach in functional cortical circuits mapping is the “all-optical” interrogation of neuronal circuits, which combines optogenetics with fluorescence microscopy. This non-invasive approach allows simultaneous functional imaging and manipulation of neuronal patterns in living animals (Mancuso et al. 2011; Emiliani et al. 2015). In the next section (1.3) we will describe commonly used and advanced functional fluorescence imaging techniques, while in the following (1.4) we will provide a detailed discussion on the newly developed all-optical approaches, including their application to motor mapping.

1.3. Sensors and systems for large-scale optical imaging of neuronal activity

Investigating the organization and function of the motor cortices requires to monitor neuronal activity from multiple cortical regions simultaneously and chronically *in vivo*. Ideally, techniques of monitoring activity with a high spatial and temporal resolution are necessary in order to study the relationship between neuronal activity propagation dynamic and animal behavior. Although electrophysiological techniques, such as intracranial recordings of single-unit activity (SUA), multi-unit activity (MUA), local field potential (LFP) satisfy both temporal and resolution parameters (Mehring et al. 2003; Burns et al. 2010), they are invasive approaches characterized by limited neuronal coverage, inability to identify the cell types recorded and difficulty in repeating the recordings multiple times on the same animal (Bin et al. 2011; Grinvald et al. 1988). Optical recording techniques, instead, offer millisecond time resolution, simultaneous recording from multiple sites, and the possibility to repeat measurement from the same areas over days and months. The most widely approach for *in vivo* optical detection of neuronal activity is fluorescence imaging (Rao et al. 2007), which is based on the excitation of a fluorophore with a light source (Tungsten filament lamps, LED or laser illumination) in a specific range of the visible wavelength (450-750nm). After its excitation, the fluorophore emits longer wavelength photons detected by a photosensitive surface that generates a digital image (Grinvald et al. 1988; Dunst and Tomancak 2019; Kerr and Denk 2008).

Commonly used fluorescence microscopy technologies include confocal microscopy, two-photon fluorescent microscopy (TPFM) and wide-field fluorescence microscopy (WFFM). They differ in sample illumination and signal detection strategies providing useful tools for a wide range of biological questions

and contexts (Weisenburger and Vaziri 2018). In confocal microscopy, the visible light laser beam is scanned over the sample and the out-of-focus emission light is blocked by a pinhole located in the detection pathway. The scattered light, coming from outside the focal plane, is therefore blocked by the spatial filter (Nwaneshiudu et al. 2012; Pawley 2006). Consequently, confocal microscopy has the advantage of rejecting out-of-focus light thus ensuring high-contrast imaging of the sample. However, confocal microscopy is limited in the achievable imaging depth (around 200 μm) and thus requires thin sections of tissue (Nwaneshiudu et al. 2012). Instead, TPFM is a non-linear optical microscopy technique that can provide subcellular-resolution three-dimensional imaging into the intact living brain. It exploits the absorption of two infrared photons that arrive simultaneously (within 0.5fs) on the sample, combining their energies and promoting the molecule to the excited state (Helmchen and Denk 2005; Oheim et al. 2001). Therefore, it is heavily dependent on the photon concentration, that is the light intensity, and requires a powerful light source like pulsed lasers (Imanishi et al. 2007). Importantly, TPFM is less sensitive to scattering providing cellular resolution imaging in intact tissues at depths up to one millimetre (Helmchen and Denk 2005). The main limitations of this technique for mesoscopic brain mapping are both the small field of view and the invasiveness of the cranial window required for optical access (Silasi et al. 2016). In fact, it is mainly used for small-networks behavior studies.

Instead, WFFM has several advantages for long-term imaging of large-scale cortical dynamics *in vivo*. It requires a small light dose to illuminate a large field of view that usually covers both hemispheres in mice, consequently phototoxicity and photobleaching of fluorophores are reduced (Ma et al. 2016; de Kernier et al. 2019; Cramer et al. 2019). Moreover, the semi-transparent nature of the mouse skull allows it to be left intact or partially thinned to gain optical access (Silasi et al. 2016; Guo et al. 2014). Thus, only skin retraction is required for a chronic transcranial window, reducing the risk of inflammation or brain damage, and making it a low invasive procedure (Silasi et al. 2016). Wide-field optical

recordings are limited to accessible areas of the brain, such as the cortex, with a recording depth of about 0.5mm (Homma et al. 2009). The main factors that limit the spatial resolution and depth sensitivity of this technique are the background scattering and absorption properties of the brain (Ma et al. 2016). Consequently, the contrast of the images is lower than confocal or TPF microscopy due to the collection of a significant background signal from out-of-focus areas, and it is difficult to identify how deep in the tissue the fluorescence originated from (Dunst and Tomancak 2019; Shaw 2006).

There are other mesoscopic imaging modalities, such as functional magnetic resonance imaging (fMRI) or Optical Coherence Tomography (OCT), which are not based on exogenous fluorophores' emission and are mainly used for hemodynamic or optical intrinsic signal (OIS) studies of the mouse brain (Kim et al. 2017; Kim et al. 2000; Park et al. 2018). However, their application in mice is limited by both the small body size of these animals and by the long procedure times, which is often combined with anaesthesia for the immobilization of the head to avoid imaging artefact (Van der Linden et al. 2007; Cramer et al. 2019). Hence, WFFM remains the most effective approach for *in vivo* studies of large-scale cortical dynamics in awake mice.

In order to longitudinally monitor the activity of many neurons with fluorescence microscopy, genetically encoded fluorescent indicators are needed. The field of fluorescence optical indicators began after the discovery of green fluorescence protein (GFP) (Tsien 1998), a spontaneously fluorescent protein isolated from the Pacific jellyfish, *Aequorea Victoria*, which transduces the blue chemiluminescence of another protein, aequorin, into green fluorescent light by energy transfer (Yang, Moss, and Phillips 1996). GFP main excitation peak is centered at 395 nm with a minor peak at 475 nm, while the emission peak is at 508 nm (Yang et al. 1996). GFP-based indicators have the advantage of allowing repeated recordings from awake animals. Moreover, the tolerance of GFPs for circular permutations and insertions of foreign proteins provided two benefits: the creation of a palette of FPs within the range of the visible spectrum (Stepanenko et al. 2018) and a new

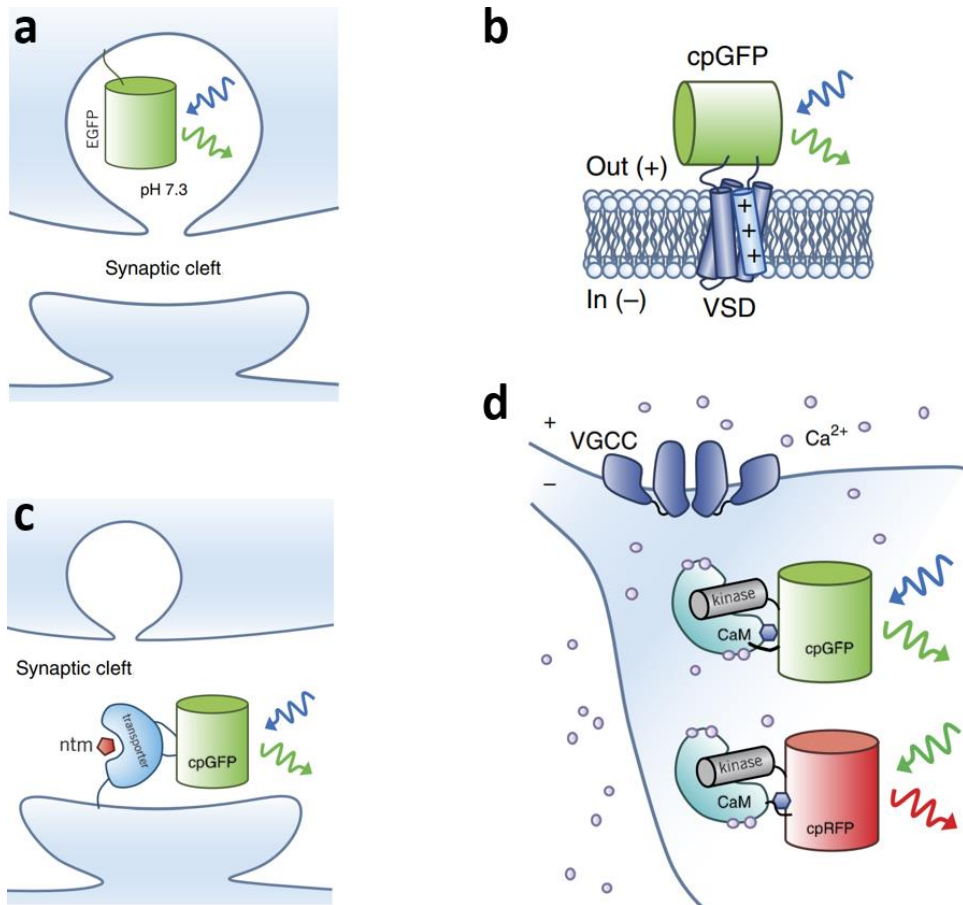


Figure 1.3: Genetically Encoded Optical Indicators. (a) Representative image of a Genetically Encoded pH Indicator (GEPI). Fusion of the synaptic vesicle induces loss of the proton from the chromophore, allowing excitation by 488-nm which results in green emission. (b) Representative image of a Genetically Encoded Voltage Indicator (GEVI). Changes of the membrane potential cause the VSD to move into or out of the membrane, leading to relatively linear changes in the fluorescence or absorbance. (c) Representative image of a Genetically Encoded Transmitter Indicator (GETI). The binding of the neurotransmitter (ntm) to its transporter induces a conformational change resulting in green emission. (d) Representative image of Genetically Encoded Calcium Indicators (GECIs). Once voltage-gated calcium channels (VGCC) are open the cytosolic calcium concentration changes. GECIs detect cytosolic calcium transients and modify their conformation modulating the green or red emission depending on the FP type bounded, cpGFP or cpRFP respectively. Adapted with permission from (Lin and Schnitzer 2016).

strategy for developing genetically encoded optical indicators (Homma et al. 2009). The wide and growing use of these indicators in the neuroscience field is due to their selective expression in genetically defined neuronal populations. There are multiple classes of genetically encoded optical indicators which are useful for different types of experiments (Lin and Schnitzer 2016). Genetically Encoded pH indicators (GEPIs) can be used as vesicular release probes (Lin and Schnitzer 2016; Rossano et al. 2013) (fig1.3a). Genetically Encoded Transmitter Indicators (GETIs) allow studying neurotransmission at presynaptic or postsynaptic level (Lin and Schnitzer 2016; Liang et al. 2015) (fig1.3c). Voltage changes in neurons are detected by Genetically Encoded Voltage Indicators (GEVI), which can be used to visualize single action potential *in vivo* (Yang and St-Pierre 2016) (fig1.3b). Another class of optical indicator is instead obtained from the fusion of GFPs with calmodulin (CaM) (Porumb et al. 1994), a ubiquitous Ca^{2+} -binding protein with large Ca^{2+} -dependent conformational changes, which led to the generation of Genetically Encoded Calcium Indicators (GECIs) (Oh, Lee, and Kaang 2019) (fig1.3d). Calcium indicators are located intracellularly and act as a buffer of calcium, a second messenger tightly coupled to membrane excitation and neuronal activity (Baker et al. 2005).

GEVIs and GECIs can both be used to detect action potential. The major limitations of GECIs are that they can bind and interfere with endogenous signalling molecules, their decay kinetics is relatively slow since it is based on the timescale of calcium dynamics and they cannot report hyperpolarizations and subthreshold depolarizations (Hires et al. 2008; Paredes et al. 2008; Lim et al. 2013; Scanziani and Häusser 2009). These limitations make their use as trackers of single action potential difficult (Yang and St-Pierre 2016). On the other hand, although GEVIs are able to detect signal action potential *in vivo*, they suffer from photodamage and/or photobleaching after prolonged illumination and the speed at which bleached GEVI molecules are replaced is slower than that of GECI (Scanziani and Häusser 2009; Yang and St-Pierre 2016). Indeed, GECI molecules are located at cytoplasmic level and cytoplasmic diffusion is faster than diffusion

in lipid membranes where instead GEVI are expressed (Fujiwara et al. 2016). This condition limits GEVI application for within-animal longitudinal studies.

Currently, stable expression of GECIs is achievable using AAV-based gene delivery methods or transgenic lines. The AAV-based gene delivery is subjected to the same problems we discussed for optogenetic actuator expression (see chapter 1.2). Therefore, of the four delivery routes approachable when this project started, the only one that could be successfully applied to adult mice was intraparenchymal AAV injection (Richard and Philippe 2011). Although it is a minimally invasive approach, intraparenchymal injection still requires surgical procedures and the expression is spatially inhomogeneous, with the highest concentration found near the injection site. Moreover, expression levels increase with time, which limits GECI imaging to a few weeks after the injection. The imaging time window mainly depends on the promoter construct, viral titer, injection volume and other factors (Badea et al. 2018). Conversely, GECI expression is stable over time in transgenic mice and it does not require surgeries. However, it should be noticed that some transgenic lines expressing genetically encoded calcium sensors show aberrant cortical activity, such as epileptiform events (Steinmetz et al. 2017). This issue is most likely related to the expression of calcium buffers during development. GECIs are categorized in two classes based on the number of fluorescence proteins (FPs) present in the indicator: FRET-based GECIs and single-FP GECIs (Perez and Nagai 2013). The first class of GECIs is based on the principle of Fluorescence Resonance Energy Transfer (FRET) whereby the energy released from a donor FP is transferred to an acceptor FP (Suzuki et al. 2016). The second class of GECI is instead based on a circularly permuted FP and a Ca^{2+} responsive element. Conformational changes due to bonds with Ca^{2+} lead to a change in the fluorescence intensity. Single-FP GECIs have some advantages over FRET-based GECI: a higher dynamic range and narrower excitation and emission spectra which allow simultaneous observation of multiple single-FP GECI in the same sample (Suzuki et al. 2016). The most widely used and best performing indicators are the GCaMP series consisting of a cpGFP with a CaM and M13- peptide on the N-

terminous and C-terminous, respectively (Deo and Lavis 2018). The GCaMP family is based on (and thus has spectral properties similar to) the GFP protein (Dana et al. 2019). Despite GCaMP indicators having already been successfully used *in vivo* in different animal models to detect distributed neuronal activity over time (Turrini et al. 2017; Scott et al. 2018), they have several limitations due to their excitation and emission spectra. Indeed, the blue excitation light used in one-photon fluorescence microscopy can cause photodamage and is highly scattered in tissue. Furthermore, the blue excitation light and the green emission of GCaMP are absorbed by haemoglobin (Svoboda and Block 1994) and other endogenous molecules like FAD (Yang et al. 2017), which reduces the penetration depth of the imaging *in vivo*. Finally, the GCaMP excitation spectrum overlaps with that of commonly used light-sensitive ion channels, such as ChR2, which limits the simultaneous use of green GECIs and optogenetic stimulation (Nagel et al. 2003; Dana et al. 2016). These limitations led to an increasing interest in developing a red variant of GECIs, namely RGECIs, with a structure similar to GCaMP but with a longer emission wavelength. RGECIs are composed of a circular permuted thermostable red fluorescent protein (RFP) (Suzuki et al. 2016; Nagai et al. 2014; Montagni et al. 2019). Among the most commonly RGECIs used, there are two variants based on two different RFPs: mRuby (like in jRCaMP1a and jRCaMP1b) and mApple (jRGECO1a and jRECO1b) which have similar spectral profiles, with excitation peaks around 558 nm and 568 nm, and emission peaks at 605 nm and 592 nm, respectively (Dana et al. 2016; Akerboom et al. 2013; Montagni et al. 2019). Although red-GECIs have a lower affinity to calcium than green-GECI, they show multiple advantages for *in vivo* imaging. First of all, they are characterized by a longer excitation wavelength, which allows deeper penetration into tissue due to a reduced scattering by endogenous fluorophores (Billinton and Knight 2001). In addition, red fluorescence is less absorbed than green fluorescence by both endogenous fluorophores and haemoglobin in mammalian tissue (Dana et al. 2016). The growing interest in red-GECI calcium indicators is mainly due to the well-separated excitation and emission spectrum between

RGECI and ChR2, which allows the simultaneous use of these two proteins to monitor and manipulate neuronal activity. The combination of wide-field imaging of RGECI and laser activation of ChR2-expressing neurons we chose in this thesis represents a new all-optical approach to study large scale cortical dynamics across multiple cortical regions during light-evoked complex movements.

1.4. All-optical strategies for functional motor mapping

As discussed in the previous chapter, a fruitful approach to study cortical functional maps at mesoscale level requires to record neural activation patterns within large cortical areas while targeted neurons are focally perturbed. One of the first attempts to achieve this aim was coupled ICMS with electrophysiological recordings or optical imaging of intrinsic signal (OIS) (Brock et al. 2013; Riehle et al. 2013). Since ICMS lacks control of targeted neuronal population, OIS was combined with finer techniques, such as blue-sensitive opsin, to study optogenetically-evoked hemodynamic signals and provide effective connectivity maps (Bauer et al. 2017; Nakamichi et al. 2019). Although hemodynamic mapping produces maps topographically similar to those obtained using VSDs and does not require surgical procedures, hemodynamic response is an indirect measurement of neuronal activity and is ~ 5 -100 times slower than imaging sensors (Cramer et al. 2019; Ma et al. 2016). Recently, optogenetics was combined with advanced optical indicators leading to the development of a new strategy for neuronal circuits interrogation: the “all-optical” approach. This strategy exploits the ability to simultaneously manipulate and record the activity of selected neuronal populations by using light. First of all, this low-invasive approach allows long term investigation of the same neuronal circuits in intact brains across time (Torricelli et al. 2014). Secondly, it is multiplexable, which implies the simultaneous use of lights with different wavelengths in the same samples (Emiliani et al. 2015). Nevertheless, critical aspects must be considered when developing an efficient all-optical system. Indeed, two spectrums are involved in the all-optical readout and manipulation of the same cells: the optogenetic actuator activation spectrum and the fluorescence reporter excitation spectrum. An overlap of these two spectra may

lead to unintended perturbation of the neuronal circuit when the optogenetic actuator is sensitive to wavelengths used for imaging or to imaging artefacts due to excitation of the fluorescent activity reporter if it is sensitive to photostimulation wavelengths (Soor et al. 2019; Emiliani et al. 2015). This is the case of one of the first all-optical approaches used successfully in mice *in vivo* (Wilson et al. 2012), in which one-photon excitation of ChR2 was combined with two-photon imaging of a green calcium dye. This study takes advantage of ChR2's low 2P excitation efficiency via laser scanning, a condition that cannot be exploited in mesoscale studies (Soor et al. 2019). Another all-optical approach that was exploited *in vivo* despite presenting the same crosstalk problem was combining ChR2 with GCaMP calcium reporter. Although this approach benefits from the use of two long term stable genetically encoded proteins, there is a large one-photon spectra overlap between actuator and reporter, which often involves a block of the readout during the crucial photostimulation period and it doesn't allow to perform imaging without unintended ChR2 stimulation (Guo et al. 2009; Szabo et al. 2014; Allegra Mascaro et al. 2019). These limitations can be reduced either by minimizing imaging light intensities, to the detriment of the signal-to-noise ratio, or by separating the optical paths for ChR2 excitation and fluorescence imaging (fig1.4b) (Guo et al. 2009; Szabo et al. 2014; Allegra Mascaro et al. 2019).

Therefore, to perform simultaneous optical readout and manipulation of neuronal circuits, the crosstalk between the imaging and manipulation channels can be minimized or even eliminated by taking advantage of two different approaches: pairing blue-green fluorescence reporters with red absorbing optogenetic actuators or blue actuators with red indicators. For the first approach, the main reporter used was the GCaMP indicator. It was combined with the red-shifted opsin C1V1 for two-photon optogenetic activation and calcium imaging with negligible optical crosstalk (Packer et al. 2015; Dagleish et al. 2020; Yang et al. 2018; Liu et al. 2020) (fig1.4b). GCaMP was also combined with another variant of red-shifted opsin (ChrimsonR) (Oda et al. 2018) to study neuronal circuits in behaving zebrafish by using one-photon stimulation of the optogenetic actuator

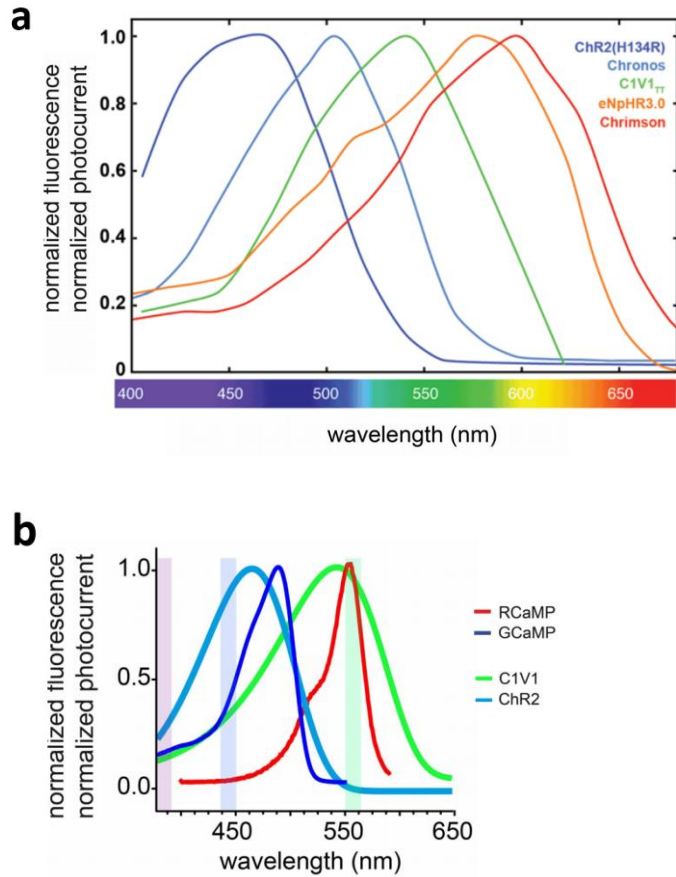


Figure 1.4: Normalized fluorescence opsins and GECIs spectra. (a) Normalized excitation spectra of the opsins (ChR2(H134R) in blue, Chronos in light blue, C1V1 in green, eNpHR3.0 in orange, Chrimson in red). Adapted with permission from (Olofsson et al. 2015). (b) Normalized excitation spectra of the optogenetically actuator (ChR2 in light blue and C1V1 in green) and of the GECIs (RCaMP in red and GCaMP in blue). Adapted with permission from (Akerboom et al. 2013).

(Förster et al. 2017; Jiao et al. 2018). Nevertheless, there is still a small crosstalk between the two proteins, as C1V1 and ChrimsonR have a blue absorption shoulder, and GCaMP6 has a red shifted absorption tail even in the one-photon configuration required for mesoscale studies (Yang et al. 2018; Oda et al. 2018; Olofsson et al. 2015) (fig1.4a-b).

Conversely, one-photon low spectral-overlap has been successfully achieved using a combination of blue actuator with red indicator. The successful combination of a blue-green absorbing optogenetic actuator (Chronos) (Hight et al. 2015) with a deep red-emitting fluorescent calcium dye (CaSiR-1) was demonstrated in slice and *in vivo* preparations (Egawa et al. 2011; Soor et al. 2019). Although the temporal resolution of Chronos is higher than that of ChR2 (Hight et al. 2015), a combination of this actuator with red-shifted indicators may cause unintended perturbation of the neuronal circuit since one-photon Chrono's spectrum is redder than ChR2's (fig1.4a). Another strategy to minimise the one-photon crosstalk with ChR2 is the use of red voltage sensitive dyes (VSD) (Lim et al. 2012a), organic membrane-bound molecules that provide direct, fast and linear measure of changes in membrane potential (Zhou et al. 2007; Lim et al. 2013). This approach was implemented *in vivo* for revealing reciprocal relationships between cortical areas at mesoscale level. Nevertheless, the lower sensitivity of dyes compared to GECI and the invasive procedures required for VSD imaging, such as craniotomy and removal of the dura mater that alter cortical physiological dynamics, don't make them suitable for longitudinal studies of cortical dynamics (Scanziani and Häusser 2009; Yang and St-Pierre 2016; Mohajerani et al. 2010). Moreover, dyes can hardly be targeted to specific neuronal populations, which is instead an essential condition for motor mapping since cellular responses in the motor cortex vary greatly between cell types (Ebbesen et al. 2018). Finally, blue-sensitive optogenetic actuators were combined with red-shifted GECIs (RCaMP or RGECO indicators). Despite R-GECO displays higher Ca^{2+} affinity and larger dynamic range than RCaMP, it exhibits significant photoactivation with blue and green light that could lead to artefacts when combined with blue-sensitive opsins (Akerboom

et al. 2013). Instead, RCaMP family is well suited for all-optical interrogation of behavioural circuits *in vivo* using ChR2 as optogenetic actuator (fig1.4b). Two-photon RCaMP2 imaging and one-photon ChR2 excitation have already been used in *C. Elegans*, but not on the same cells (Inoue et al. 2015). Indeed, this study combined presynaptic stimulation with postsynaptic recording. Recently, a similar approach combining two-photon holographic ChR2 stimulation and two-photon imaging of the red-shifted indicator jRCaMP1a was tested in mouse neocortex *in vivo* (Forli et al. 2018). The authors demonstrated that this configuration drastically reduces the crosstalk, preserving enough laser power for both imaging and optogenetics.

One of these approaches was used to perform large-scale connectivity mapping. Lim and colleagues, in 2012, combined ChR2 with VSD to perform functional mapping of the interhemispheric and interhemispheric connectivity during sensory stimulation or local photostimulation (Lim et al. 2012b). Few years later, the same group successfully exploited this approach to map connectivity changes after a targeted cortical stroke (Lim et al. 2014). Nevertheless, this combination is not suitable for longitudinal studies. We therefore took advantage of the all-optical approach used by Forli et colleagues and tested it in a one-photon mesoscale configuration in order to investigate the functional organization in RFA and CFA during optogenetically-evoked complex movements, a field still unexplored. Our approach allowed correlating the effective local connectivity evoked during complex movements with the light-based motor maps, thus providing an important tile to our understanding of how the motor cortex drives complex behaviours.

2

Methods and procedures

2.1. Surgical procedures

All procedures were approved by Italian Minister of Health (aut. n. 871/2018). Adult animals examined in this study were C57B/6 of both sexes (age 6-12 months). Surgical procedures were conducted under isoflurane anaesthesia (3% for induction, 1-2% for maintenance). Animals were placed into a stereotaxic apparatus (KOPF, model 1900). The skin and the periosteum were cleaned and removed and bregma was signed with a black fine-tip pen. Different surgical procedures were used for viral injections, depending on the experiment.

For the characterization of four red-shifted indicators, the viral vectors (CliniSciences) used were:

- jRCaMP1a: pGP-AAV9-syn-NES-jRCaMP1a-WPRE.211.1488
- jRCaMP1b: pGP-AAV9-syn-NES-jRCaMP1b-WPRE.211.1519
- jRGECO1a: pGP-AAV9-syn-NES-jRGECO1a-WPRE.111.1670
- jRGECO1b: pGP-AAV9-syn-NES-jRGECO1b-WPRE.111.1721.

To achieve widespread indicator transduction over the right hemisphere, a small hole (\varnothing 0,4 mm) was drilled at coordinate ML +1,5 mm, AP -1,5 mm from bregma. A 500 nl volume of virus (per indicato, $n_{\text{mice}} = 4$) was pressure-injected through a pulled glass micropipette (\varnothing of the tip: 50 μm) at two depths per site (-0,4 mm and -0,8 mm ventral from dura surface) using an electrically gated pressure injector (Picospritzer III—Science Products™, 3 Hz, ON 4 ms).

For testing the indicator responsiveness to two different behavioural states, 500 nl of jRCaMP1a construct (pGP-AAV9-syn-NES-jRCaMP1a-WPRE.211.1488) was injected into the primary motor cortex ($n = 3$; +1,75 mm ML, +0,5 mm AP from bregma) at one depth (-0,5 mm ventral from dura surface) using an electrically gated pressure injector (Picospritzer III—Science Products™, 3 Hz, ON 4 ms).

For simultaneous one-photon imaging and optogenetic stimulation, to achieve widespread expression of both jRCaMP1a and ChR2 over the right hemisphere, small holes were drilled at two coordinates (AP +2.0 mm, ML +1.7 mm; AP -0.5 mm, LM +1,7 mm from bregma). A 500 nl volume of mixed virus (pGP-AAV9-syn-NES-jRCaMP1a-WPRE.211.1488 and pAAV9-CaMKII-hChR2(H134R)-

Cerulean, 1x10¹³ GC ml⁻¹, CliniSciences, 250 nl respectively) was pressure-injected through a pulled glass micropipette at two depths per site (-0.4 and -0.8 mm ventral from dura surface) using an electrically gated pressure injector (Picospritzer III—Science Products™, 3 Hz, ON 4 ms) for a total volume of 1 µl per mouse.

A custom-made aluminium head-bar placed behind lambda and a cover glass implanted on the exposed skull were fixed using transparent dental cement (Super Bond C&B – Sun Medical) to allow the fixation of the head for awake imaging and free optical access to the cortex respectively. After the surgery, mice were recovered in a temperature- and humidity-controlled room, with food and water ad libitum for two weeks before recordings.

2.2. Wide-field microscope setup

For the characterization of four red-shifted indicators, A custom-made wide-field imaging setup was used to image the fluorescence signal of the GECIs. This setup was equipped with an excitation source for R-GECIs fluorescence imaging (595 nm LED light, M595L3 Thorlabs, New Jersey, United States), and a bandpass filter (578/21 nm, Semrock, Rochester, New York, USA) allowed the selection of the excitation band. A dichroic filter (606nm, Semrock, Rochester, New York USA) above the objective (2.5× EC Plan Neofluar, NA 0.085) deflected the excitation light beam towards the sample. Finally, a 3D motorized platform (M-229 for xy plane, M-126 for z-axis movement; Physik Instrument, Karlsruhe, Germany) allowed animal positioning under the objective. The fluorescence signal was collected through a bandpass filter (630/69, Semrock, Rochester, New York, USA) and focused by a tube lens (500mm) on the sensor of a high speed complementary metal-oxide semiconductor (CMOS) camera (Orca Flash 4.0 Hamamatsu Photonics, NJ, USA).

For simultaneous one-photon imaging and optogenetic stimulation we took advantage of a second excitation source to simultaneously excite the opsin (ChR2-*cerulean*) and the calcium indicator (jRCaMP1a) (Conti, Allegra Mascaro, and Pavone 2019). The excitation source was a continuous wavelength (CW) laser ($\lambda = 473$ nm, OBIS 473 nm LX 75mW, Coherent, Santa Clara, CA, USA). The excitation beam was overlaid on the imaging pathway using a second dichroic beam splitter (FF484-Fdi01-25 \times 36, Semrock, Rochester, New York, NY, USA) before the objective. The system has a random-access scanning head with two orthogonally mounted acousto-optical deflectors (DTSXY400, AA Opto-Electronic, Orsay France). The jRCaMP1a fluorescence signal emitted was collected through a band-pass filter (630/69, Semrock, Rochester, New York, USA) and focused by a tube lens (500 nm) on the sensor of a demagnified (20X objective, LD Plan Neofluar, 20 \times /0.4 M27, Carl Zeiss Microscopy, Oberkochen, Germany) high speed complementary metal-oxide semiconductor (CMOS) camera (Orca Flash 4.0 Hamamatsu Photonics, NJ, USA).

2.3. Wide-field imaging in awake behaving mice

The camera acquired images at a resolution of 100 by 100 px² covering a square field-of-view of 5,2 by 5,2mm² of the cortex. 14 days after the injection, head-fixed imaging sessions were performed for three consecutive weeks. An animal specific-FOV template was used to manually adjust the imaging field daily.

For the characterization of four red-shifted indicators, an imaging session consisted of 40s of recording in resting state (sampling rate: 25 Hz, LED power 23 mW, 32 mW cm⁻²). During the last week, one experimental group (AAV9-jRCaMP1a, viral transfection in motor cortex, $n_{\text{mice}} = 3$) was subjected to behavioural training for five consecutive days (see section 2.4 below).

For simultaneous one-photon imaging and optogenetic stimulation, each recording session consisted of 5-10 s in resting state followed by the stimulus and other 30 s of imaging (sampling rate: 50Hz). The waiting time for consecutive sessions was 3 minutes per animal. LED light intensity was 4 mW after the objective.

2.4. Robotic platform

Mice expressing jRCaMP1a in the motor cortex (n=3) performed five consecutive days of training in the robotic platform device (Spalletti et al. 2013). A resting state imaging session was recorded each day before the training. The single daily session consisted in 15 cycles or ‘trials’ of active retraction of the left forelimb associated with a sweetened condensed milk reward (10 μ l) upon reaching the target position (fully-retracted).

The robotic device (M-platform) is based on the one described in Spalletti et al 2013. It was composed of a linear actuator, a 6-axis load cell (Nano 17, ATI Industrial Automation, USA), a precision linear slide with an adjustable friction system and a custom-designed handle where the left wrist of the mouse was allocated, which allowed a transfer of the force applied by animals to the sensor.

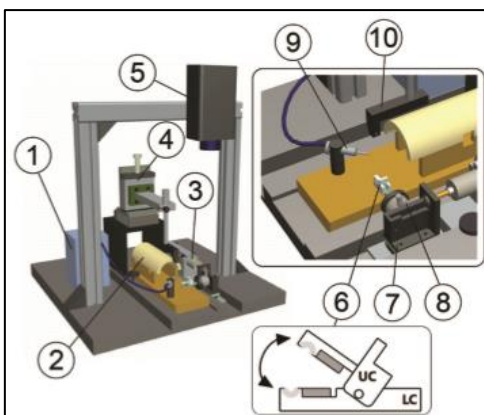


Figure 2.1: Schematic representation of the robotic platform. (1) peristaltic pump for reward release. (2) Snout suspension device. (3) Linear motor. (4) Micromanipulator for mouse head positioning. (5) Camera. (6) Handle. (7) Slide. (8) Load cell. (9) Gaving-feeding needle. (10) Head fixing system. Bottom on the right the diagram of the handle with the upper (UC) and lower (LC) components, the two magnets (gray) and the semi-circular groove (light gray). (Spalletti et al. 2013)

For each trial, a linear motor pushed the slide and extended the mouse left forelimb by 10mm (passive phase). Two acoustic signals informed the mouse of the end of passive phase (0.5s) and the reaching of a target position (1 s), which was associated with reward. Then, the motor was quickly decoupled from the slide and the mouse was free to voluntarily pull the handle back (active phase). During the exercise, the robotic device integrated in the wide-field microscope allowed simultaneous recording of: (i) cortical activity over the right hemisphere, measured as a change in fluorescence signal, (ii) the force applied by left forelimb and (iii) the limb position, estimated by the movement of the slide using an IR position sensor located on the slide and recorded by an IR camera (EXIS WEBCAM #17003, Trust).

2.5. Optogenetic stimulation

Laser stimulation patterns were generated using two orthogonally mounted acousto-optical deflectors controlled by a custom-written LabView 2013 software (National Instruments). A reference image of the FOV was used to target the laser beam on a selected cortical area. Laser stimulation was manually triggered and synchronized with the animal movements by a mirror, which deflected part of the laser beam into the FOV of the camera used for behavioral recording.

Single pulse laser stimulation consisted of one pulse (10ms ON) randomly repeated for 8 times in one imaging session at different laser power (0,22 – 1,3 – 2,5 – 5,2 – 7,7 – 13,2 mW, after the objective).

The train stimulus consisted of 2 s, 16 Hz, 10ms ON repeated once per imaging session. For laser power calibration experiments the train's laser power used were: 1,3- 2,5 - 5,2 - 7,7 - 13,2 mW. For light-based motor mapping, connectivity studies and pharmacological inhibition laser power was the minimum power required to evoke the movement per animal (from 1,3 mW to 13,2 mW).

2.6. Light-based motor mapping (LBMM)

The LBMM for locomotion-like (TAP) and grasping-like (GRASP) movements were obtained in separate experiments. A virtual grid (14 x 14, 364 μm spacing) was superimposed on the animal-specific FOV template using ImageJ. The stimulus train was delivered once for all sites of the grid in a random order. The left forepaw position during imaging sessions was monitored using a camera equipped with a red light focused on the forepaw, which did not interfere with imaging. Forelimb movements were evaluated by two different expert observers and visually categorized as (i) grasping-like movements: contralateral forepaw was closed, the wrist turned and moved toward the mouth (ii) locomotion-like movements: contralateral forelimb was retracted and lifted up at least 2 times, simulating a walking movement (iii) no-movements and movement interference: the absence of both the movements showed before during the stimulus.

Lateral Forelimb Area (LFA) LBMM. 4 out of 8 animals presented a discrete LFA and RFA light-based motor map. Those maps were firstly aligned to each other using three points in the FOV as reference (bregma and the injection sites). Secondly, the aligned LFA LBMM were overlaid across all mice and then a threshold (100%, high restriction) was applied to identify the region on which the overlap was total (n=4). The average LFA LBMM was used as a mask for identifying the LFA border in those animals that presented a unified LBMM which covered both the grasping areas (n=4).

2.7. Video tracking analysis

A machine vision camera (PointGrey flir Chamaleon3, CM3-U3-13Y3C-CS) was orthogonally set 100 mm in front of the mouse to evaluate the left forelimb movement induced by contralateral optogenetic stimulation (frame rate 100Hz). The camera acquired images at a resolution of 800 by 600 px² covering a field-of-view of 24 by 18 mm² of the cortex (0,03mm per pixel). Visible light at 630nm used as the light source was focused on the left forepaw, to avoid imaging interference. Five individual trains per movement category for one animal were filmed (nmice = 1; ntrains = 5). Videos were analyzed using the ImageJ plugin AnimalTracker, obtaining XY coordinates of the forelimb in each frame from a starting point (Gulyàs, MB et al., 2016 for details). To compare evoked complex movements we analyzed the tracked forelimb medio-lateral displacement, the elevation and the speed (mm/s) for each train.

2.8. In vivo Local Field Potential recording

Local field potentials (LFPs) were recorded in the site of injection, six weeks after the surgery in jRCaMP1a+/ChR2+ mice. Glass pipettes were used to avoid light-induced artifacts during the electrophysiological recordings and filled with a 2mM NaCl solution. The electrode was advanced, through a little hole in the skull, into the motor cortex L5 (800 µm ventral from the dura surface) using a motorized micromanipulator (EXFO Burleigh PCS6000 Motorized Manipulator). A 3000 AC/DC differential amplifier was used to amplify the signal recorder, which was sampled at 10 kHz, high-pass filtered at 0.1 Hz and lowpass filtered at 3 kHz. A reference and ground screws were placed on the occipital bone. LFP signal was recorded during a random activated pattern of led ON / led OFF (2 seconds each, 4,5 mW). As a control, an optogenetic single-pulse stimulus was delivered close

to the pipette tip, resulting in a fast-downward deflection, indicating that Chr2 was effectively transfected and functioning.

2.9. Ex vivo imaging

For the *ex vivo* characterization of four red-shifted indicators, mice were perfused with 20–30ml of 0.01 M PBS (pH 7.6) and 150ml of 4% paraformaldehyde (PFA) four weeks after injection. After the perfusion, brain coronal slices (100 μm thick) were obtained using a vibratome (Vibratome Series 1500—Tissue Sectioning System). The rostro-caudal transfection extension was evaluated by acquiring each slice by WFFM (exposure time 12 ms, LED power 23 mW).

The signal to noise ratio (SNR) was calculated on the average of the three brightest slices for each group as follows:

$$SNR = \frac{S}{R}$$

where S was the average fluorescence intensity of a ROI (0,24 mm²) centered on the brightest area in the slice, while R was the mean intensity of noise obtained from a ROI placed in the darkest area on the same slice, which was far from the site of injection then.

For *immunohistochemistry procedures* mice were perfused six weeks after injection. Brain coronal slices were washed with PBS and incubated in PBS/0.3% Triton X-100 containing 1% bovine serum albumin (BSA) for 60 min while shaking at room temperature (RT). Then, slices were washed with PBS/0.1% Triton X-100 (T-PBS) and incubated with the primary antibody NeuN (1:200, Sigma, ABN78) in T-PBS for 1 day at 4°C while shaking. Following incubating, slices were washed with T-PBS and incubated with anti-rabbit fluorescent Alexa 514 antibody (1:250, ThermoFisher, A-31558) in T-PBS for 2 h at RT while shaking. Finally, slices were washed and mounted on a glass slide. Imaging was

performed with a confocal laser scanning microscope (CLSM, Nikon Eclipse TE300, with the Nikon C2 scanning head), equipped with a Nikon Plan EPO 60× objective, N.A. 1.4, oil-immersion). The setup was equipped with a 408 nm, 488 nm and 561 nm laser to simultaneously excite ChR2, Alexa 514 and jRCaMP1a respectively. A triple-band dichroic mirror 408/488/543 was used for simultaneous 3-channel fluorescence imaging. Emission filters were 472/10 nm, 520/35 nm and 630/69 nm, respectively.

2.10. Pharmacology treatment

For pharmacological interference experiments, a small craniotomy (\varnothing 1 mm) was performed on a region of interest. For the animals that undergo both pharmacological inhibition of GRASP and TAP the experiments were performed in a 3-day separate section. The craniotomies were then sealed with Kwik-seal (World Precision Instrument) after the experiment sections. Glutamate receptor antagonist CNQX 1 mM (C127 Sigma-Aldrich) and vehicle (physiological solution containing 0.01 % DMSO) were applied to the craniectomy and the solutions were replenished (at the same concentration) every 10' to compensate tissue drying. Trains of stimulation were performed every 10'.

2.11. Imaging data analysis

Analysis has been performed using ImageJ, OriginPro and Mesoscale Brain Explorer software (MBE). For each imaging session, changes in the fluorescence signal were expressed as $\Delta F/F$ according to the following formula:

$$\Delta[Ca^{2+}] \propto \frac{\Delta F}{F} = \frac{[F_t - F_0]}{F_0}$$

where F_0 was the average of baseline fluorescence intensity and F_t was the fluorescence issued at a given time.

For simultaneous one-photon imaging and optogenetic stimulation experiments, the laser in the visible range (470 nm) used for the optogenetic stimulation of ChR2 generated a strong artifact in the imaging channel during the stimulation. Since the optical elements along the collection path (emission filter and the dichroic) should cut off the reflections from the laser, a strong component of this signal could be attributed to the autofluorescence excited from the intact skull. Therefore, we optimized the stimulation frequency (16Hz) according to the sampling rate of the imaging channel (50Hz) to simultaneously optogenetically-evoke a complex behavior and collect sufficient artifacts-free imaging frames, thus saving one frame over three and avoiding the blocking of the imaging readout during the photostimulation period. Daily individual mask was created using the maximum intensity projection of the first imaging session (baseline) per animal. Masks were thresholded at two times the mean value of the non-transfected hemisphere. For each imaging session, the fluorescence ratio change ($\Delta F/F$) was calculated averaging the first 50 frames before the stimulus onset (baseline fluorescence signal; F_0).

In vivo quantification of red-shifted GECIs average activity was performed on the whole field of view weekly. Only fluorescence peaks with intensity 20% higher than the baseline were considered.

The full width at half-maximum spatial distribution of the fluorescence profiles was evaluated on the average of the three brightest frames in the imaging session. For the *in vivo* characterization of four red-shifted indicators FWHM was calculated over two orthogonal lines that crossed the injection sites (rostral-caudal and medial-lateral plane), four weeks after injection. The peak amplitude was evaluated as the maximum intensity value achieved in the FWHM profile. *In vivo* jRCaMP1a and ChR2 spatial distribution was evaluated during the third

and fourth weeks after injection. The FWHM of the fluorescence profile was calculated on the resting state imaging session and over two parallel lines that crossed the injection sites in the mediolateral plane.

For testing the indicator responsiveness to two different behavioural states, five regions of interest (ROIs, area 0.24 mm²) located on specific functional areas were analysed: primary and secondary motor cortex (M1 and M2), primary sensory cortex of barrel field and forelimb region (S1BL and S1FL) and retrosplenial cortex (RS). The anatomical localization of these areas was aided by using illustrations in a stereotaxic atlas (Paxinos and Franklin 2019).

The correlation matrices were realized using data from a single mouse and analyzed by mesoscale brain explorer (MBE) software (mesoscale). Cortical activity correlation index (r) was related to both the synchronicity of fluctuations in signal intensity and the delays with which peaks occur in different areas. It was calculated between the following five cortical regions: (1) primary motor cortex (M1); (2) somatosensory representation of forelimb region (S1FL); (3) secondary motor cortex (M2); (4) retrosplenial cortex (RS); (5) sensory cortex in barrel-field region (S1BF). The correlation matrix was calculated for both the resting state condition and during a motor task execution on the same mouse. The ‘resting state’ correlation matrix was obtained on a collated sequence of 12 randomly selected baseline imaging datasets. The ‘motor task’ correlation matrix was instead calculated on 12 of 15 consecutive retraction trials on the motor platform. Imaging subsets analyzed were selected based on two conditions: when the peak force necessary to pull the slide in an attempt managed to produce displacement of the slide and when it was associated with a rewarded pull. We discarded the trials where the paw slipped away from the slide. The scatter distribution was obtained by correlating the force peaks exerted by the mouse with the corresponding activity peaks in M1 ($n_{\text{peak}} = 19$). The scatter distribution threshold was instead obtained averaging the maximum value of the intensity peaks in resting state condition ($n_{\text{peak}} = 19$).

Single-pulse correlation was performed during the third and fourth weeks after injection. Single-pulse laser stimulation was delivered to the cortex region on which there was the maximum expression level of both Chr2 and jRCaMP1a. The consequently evoked calcium dynamics were then extracted from a region of interest (ROI, area 0,24mm²) placed over the stimulation site.

Power calibration. The optogenetic stimulus was delivered in the centre of the optogenetic map. The stimulus train was repeated 3 times at increasing laser power to select the minimum power required to evoke GRASP and TAP movements. Calcium dynamics (time series) were extracted from a region of interest (ROI, area 0,24 mm²) placed over the site of stimulation.

Movement specific calcium map. An imaging session was recorded for each site of the grid stimulated during the light-based motor mapping (14 x 14, 364µm spacing). For each acquisition, the Maximum-Intensity Projection (MIP) was obtained and subsequently spitted in five experimental group based on evoked-movement category: (i) GRASP RFA movement, (ii) GRASP LFA movement, (iii) TAP movement. Since optogenetic maps for TAP and GRASP were obtained in separate experiments, there were two different groups of no-movement: (iv) GRASP-related no-movement and (v) TAP-related no-movement. The average maximum activity value was then calculated for GRASP RFA/LFA and TAP categories based on all MIPs, and half of that value has been used for thresholding the individual MIPs per experimental group. Thresholded MIPs were then averaged and an additional threshold of 2x SD was applied, obtaining the average calcium map for all five experimental groups. In order to obtain movement specific activity maps (MSAMs), the no-movement average calcium map was spatially subtracted from the related movement average calcium map per movement category (GRASP RFA, GRASP LFA and TAP).

Maps overlap. The LBMM was then spatially overlaid to the related MSAM to assess the percentage of overlap between them, which was quantified as a percentage of the total dimension of both the maps used to obtain the value (LBMM/MSAM or MSAM/LBMM).

The Spatiotemporal propagation analysis was performed with custom-made Python (Python Software Foundation, Beaverton, Oregon, U.S.A.) scripts. In a pre-processing step, image sequences were masked and frames containing the laser stimulations were manually eliminated and replaced with their temporal linear interpolation. Then a Gaussian smoothing was performed along the temporal dimension before computing the $\Delta F/F_0$ signal. F_0 was set as the average fluorescence value observed before the first laser stimulus. Active pixels were identified setting a pixel-based threshold. This threshold was set where the maximum value of the $\Delta F/F_0$ signal after the first laser stimulus was larger than the average value plus the double of the standard deviation value, both computed before the first stimulus. In active pixels, the time-frame corresponding to the first crossing of a pixel-based threshold was used to identify the timing of the response to the laser stimulus. For imaging acquisitions pertaining to CNQX manipulation, the standard deviation values used to identify the active pixels and to define the timing thresholds were computed solely on the data acquired before CNQX administration (vehicle). For the data acquired after CNQX administration, the average of the standard deviations computed before CNQX administration was employed. In all cases, the timing values were then rank-transformed. The rank values of the active pixels related to the same animal and the same condition were averaged and the standard deviation was computed, while the non-active pixel values were discarded. Starting from these averaged results, for data related to CNQX manipulation, rank distributions were computed in a region of interest (ROI) overlapping the optogenetic maps. The distributions before and after CNQX administration were then compared using Wilcoxon signed-rank test to test their differences. Moreover, to summarize the distribution characteristics, their medians and interquartile ranges were computed. Finally, to trace the propagation direction, for each averaged result, pixels placed along a circumference centered on the laser-stimulated area and with varying radius were selected, discarding non-active or masked pixels. For each circumference radius, the averaged rank distribution was computed and values composing its first quintile were sub-selected. Then the

circular mean of the angular position (relative to the circumference center) of these values was computed (Mardia 1999). Finally, all the computed circular means were used to calculate the final, radius-dependent, circular mean and circular standard deviation (Mardia).

2.12. Statistical analysis

All statistical analysis was computed in OriginLab 2018 except for the Spatio-temporal propagation analysis that was performed with custom-made Python scripts (Python Software Foundation, Beaverton, Oregon, U.S.A.). Data are shown as mean \pm SEM. Parametric tests were used after the Shapiro-Wilk and Kolmogorov-Smirnov normality test results. The error bars and shadows in graphs represent the SEM. For spectral bands comparison (multiple comparisons), two-way ANOVA with Bonferroni post-hoc test was used. For average calcium transient comparison (multiple comparisons) one-way ANOVA with Bonferroni post-hoc test was used. The level of significance was set at * $p < 0.05$, ** $p < 0.01$, and *** $p < 0.001$.

3

Results

3.1. Characterization of four red-shifted calcium indicators for functional wide-field imaging

In this section we examined four different commercially available red-shifted calcium indicators, characterizing their properties (brightness, width of expression and stability) for long-term *in vivo* mesoscale studies. Second, we compared the response of the best performing indicator under two different behavioral states, i.e. resting state versus active behavior (execution of a motor task), to evaluate its sensitivity in detecting *in vivo* neuronal activity on multiple cortical areas simultaneously.

3.1.1. Stable expression of red-shifted indicators over four weeks

To assess the transduction stability of four different red-shifted GECIs (jRCaMP1a, jRCaMP1b, jRGECO1a, jRGECO1b) on the right cortical hemisphere over weeks, intraparenchymal injections of an AAV expressing one of the red-GECI variants was performed in adult mice (fig3.1). The expression stability was compared across indicators by examining 40s of resting state spontaneous cortical activity in the somatomotor cortex, averaged across time. Results showed no significant variability of the averaged activity over weeks except for the jRCaMP1b indicator, which failed to exhibit significant responses. jRCaMP1b mice showed so low activity levels to be comparable to the background noise. Among the other three indicators, jRGECO1a showed the best average values over weeks (figure 3.2, $n_{\text{mice}} = 4$ exp-group). This result highlights the stability of these indicators for weeks after the injection.

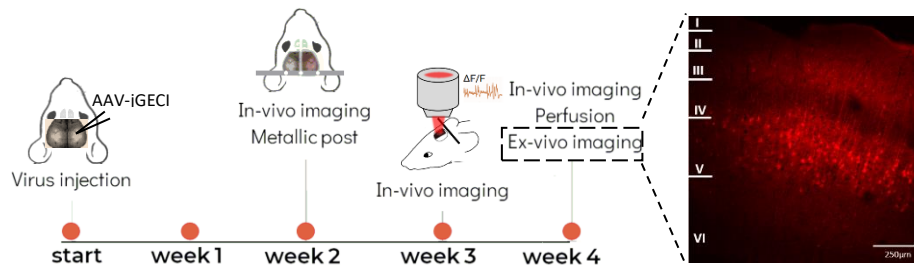


Figure 3.1 Experimental timeline . AAV-GECI injection is performed at cortical level. After two weeks from the surgery, a metallic post is implanted. Imaging sessions is repeated weekly. At the end of *in vivo* experiments, mice are sacrificed and brain slices are analysed in wide-field microscopy. The ex vivo image on right is acquired by a standard confocal microscope (Nikon Eclipse TE300).

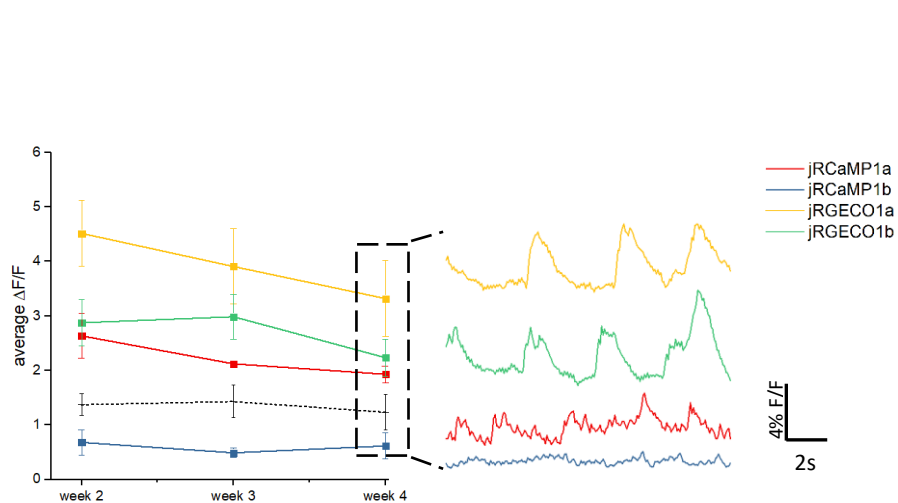


Figure 3.2 Red-shifted indicators stability over four weeks. Left, average cortical activity of four different red-shifted indicators across 4 weeks. Right, representative traces of *in vivo* fluorescence activity for each indicator during the fourth week. jRCaMP1a: $\Delta F/F_{W2} = 2.6 \pm 0.4 \%$; $\Delta F/F_{W3} = 2.1 \pm 0.1 \%$; $\Delta F/F_{W4} = 1.9 \pm 0.1 \%$; jRCaMP1b: $\Delta F/F_{W2} = 0.6 \pm 0.2 \%$; $\Delta F/F_{W3} = 0.5 \pm 0.1 \%$; $\Delta F/F_{W4} = 0.6 \pm 0.2 \%$; jRGECO1a: $\Delta F/F_{W2} = 4.5 \pm 0.6 \%$; $\Delta F/F_{W3} = 4.0 \pm 0.1 \%$; $\Delta F/F_{W4} = 3.3 \pm 0.7 \%$; jRGECO1b: $\Delta F/F_{W2} = 2.9 \pm 0.4 \%$; $\Delta F/F_{W3} = 3.0 \pm 0.4 \%$; $\Delta F/F_{W4} = 2.2 \pm 0.3 \%$; Threshold: $\Delta F/F_{W2} = 1.3 \pm 0.2 \%$; $\Delta F/F_{W3} = 1.4 \pm 0.3 \%$; $\Delta F/F_{W4} = 1.2 \pm 0.3 \%$). Values are reported as average \pm SEM

3.1.2. *In vivo* brightness comparison between four red-shifted GECIs

Four weeks after injection, the brightness of fluorescence was quantified by examining the three brightest frames in resting state. The pixel values were obtained along both a rostral-caudal and a medio-lateral line passing through the site of injection for each indicator (fig3.3a). On the spatial fluorescence profiles, the full width at half maximum (FWHM) and the peak amplitude was evaluated (fig2.4a). Our results showed that the fluorescence distribution was isotropic from the injection site along both the planes for all the indicators. Additionally, jRCaMP1a and jRGECO1b exhibited the largest *in vivo* spatial distribution on both rostral-caudal (RC) and medio-lateral (ML) plane (fig3.3b, results in table 1. jRCaMP1b fluorescence was comparable to noise values). jRCaMP1a also produced the brightest basal level of fluorescence (fig3.3c, results in table 1). Taken together, these results showed that the spatial distribution of the jRCaMP1a indicator was significantly larger than the other.

3.1.3. Characterization of expression profiles on histological brain slices

To finely quantify the indicators expression profile throughout the entire right hemisphere, the *ex vivo* rostral-caudal extension of the transfection and its fluorescence level was assessed. Our results confirmed that three out of four indicators were successfully transfected, while the expression level of jRCaMP1b indicator was not detectable in our analysis (fig3.4a). Compared to the other indicators, jRCaMP1a construct showed both the widest *ex vivo* transfection at cortical level (fig3.4b, results in table 2; $n_{\text{mice}} = 4$ exp-group); and the best signal to noise ratio (fig3.4c and table 2). Consistent with other results in this study, jRCaMP1a resulted as the highest performing indicator for mesoscale imaging.

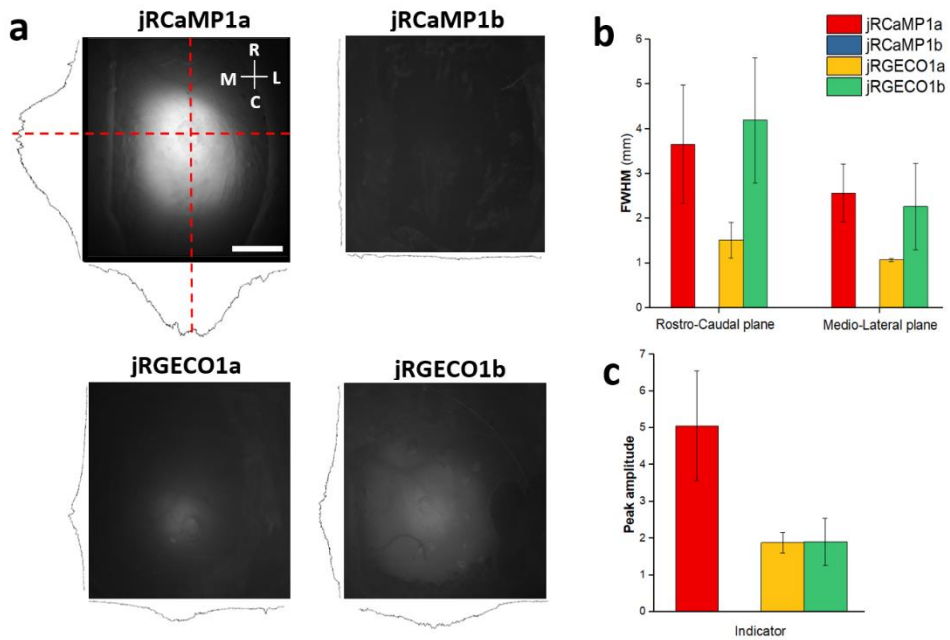


Figure 3.3: *In vivo* brightness quantification of four different red-shifted indicators. (a) Representative images of fluorescence spatial distribution for each indicator. On the bottom and on the left of each image, the fluorescence profiles along both the medium-lateral and rostro-caudal plane are reported. Scale bar, 1 mm. (b) Full width at half maximum (FWHM) of fluorescence profiles along both rostro-caudal (left) and medio-lateral plane (right) per indicator, four weeks after surgery. (c) Average $\Delta F/F$ values of fluorescence profile, four weeks after AAV injection. Values reported as average \pm SEM.

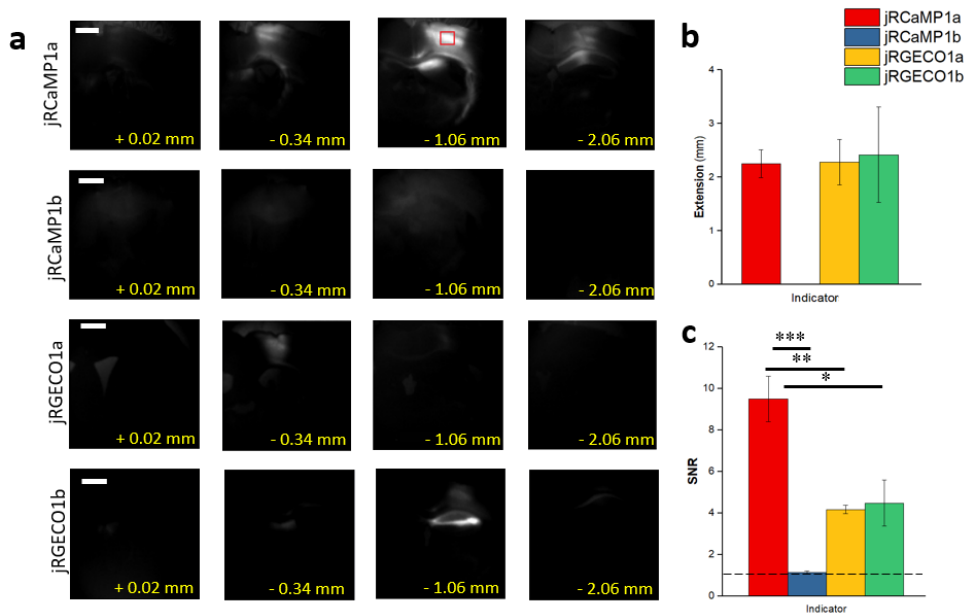


Figure 3.4: Ex vivo characterization of red-shifted calcium indicators. (a) Representative brain slice sequences showing rostro-caudal extension of transfection for the indicators. The images are selected at the same distance from bregma (from +0,02 mm to -2,06 mm relative to bregma) one month after AAV injection. The red rectangle shows the ROI used for signal-to-noise ratio analysis. (b) Average rostro-caudal extension of transfection (c) Signal-to-noise ratio for each indicator. For SNR comparison, one-way ANOVA followed by the Bonferroni test is used: * $P < 0,05$, ** $P < 0,01$, *** $P < 0,001$. Values are reported as average \pm SEM. Scale bar, 1mm.

Table 1. *In-vivo* comparison among subgroups of the fluorescence profiles.
Values reported as average \pm SEM.

	FWHM – RC (mm)	FWHM – LM (mm)	$\Delta F/F$ %
jRCaMP1a	3.7 ± 1.3	2.6 ± 0.6	5.1 ± 1.5
jRGECO1a	1.5 ± 0.4	1.1 ± 0.1	1.9 ± 0.3
jRGECO1b	4.2 ± 1.4	2.3 ± 1.0	1.9 ± 0.5

Table 2. *Ex-vivo* comparison of fuor red-shifted calcium indicators.
Values reported as average \pm SEM.

	Extension (mm)	SNR
jRCaMP1a	2.6 ± 0.2	9.4 ± 1.1
jRCaMP1b	0 ± 0.1	1.1 ± 0.1
jRGECO1a	2.3 ± 0.4	4.2 ± 0.1
jRGECO1b	2.8 ± 1.2	4.5 ± 1.1

3.1.4. Evaluation of motor task-evoked jRCaMP1a response

The sensitivity of jRCaMP1a was further tested by studying motor cortex response evoked by the execution of a motor task. We monitored the neuronal activity for four weeks in resting state before the training on a robotic device (M-platform (Spalletti et al. 2013)). The robotic platform allowed to record simultaneously the force and position of the left forelimb while monitoring the contralateral cortical activity (fig3.5b-c and fig3.6a). The motor task consisted of 15 consecutive active retractions of left forelimb. Once reaching the target position (the left limb was fully-retracted), the mouse received a milk reward. This training session was performed daily for 5 days.

Five different functional areas were selected for the analysis: M1, M2, RS, S1FL and S1BF (fig3.5a). The neuronal activity correlation matrices were computed for both the resting state and during task execution. In the last case, we selected only the timeframes of the imaging dataset corresponding to force peaks associated with forelimb movements (peak 4 in fig.3.5d). The forelimb retraction produced a strong positive change in fluorescence signal, highlighting a high and widespread correlation of neuronal activity during the motor task compared to resting state. The higher variation of correlation index took place between two ROIs pairs: R-M2/R-S1FL and R-RS/R-S1FL (fig3.6b). We also analyzed the strength of the motor cortex evoked response associated with a broad range of forces applied. Interestingly, we found that when the force applied during the active retraction by the forelimb has small intensity, the M1 activity associated was detectable and slightly higher than the average value measured in resting state condition. As the applied force increases, the maximum activity of M1 increases linearly (fig3.6c). In conclusion, the extension of jRCaMP1a transfection covered an area large enough to simultaneously record neuronal activity on cortical regions

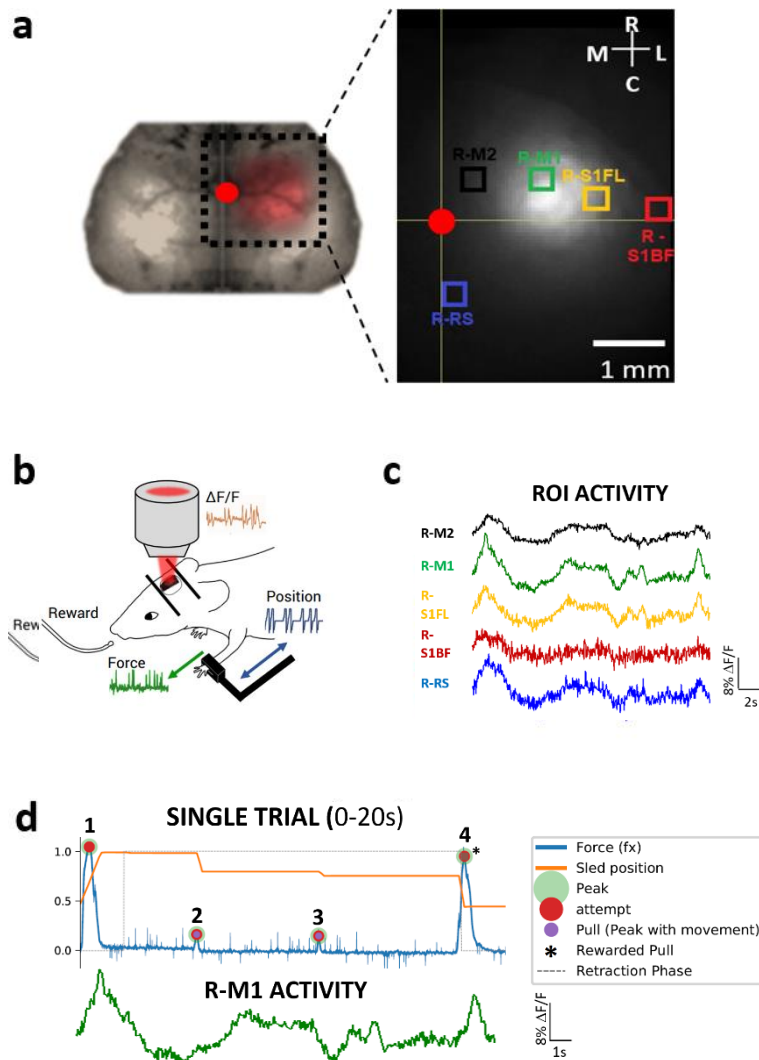


Figure 3.5: Motor task-evoked M1 cortical response (a) Representation of both the position of our field of view on the right hemisphere (right) and the 5 cortical functional areas used for the correlation matrixes (left). The ROIs are primary and secondary motor cortex (M1 and M2, green and black respectively), primary sensory cortex in barrel field and forelimb region (S1BF and S1FL, red and yellow respectively) and retrosplenial cortex (RS, blue). Red spot represented the bregma. Scale bar, 1mm. (b) Schematic view of the M-platform used for the training, which is integrated with the wide-field microscope. It allows simultaneous recording of three data: the force applied by forelimb (green), the position of left forelimb (blue) and the contralateral cortical activity as a change in the indicator fluorescence intensity (red). (c) Representative traces of neuronal activity recorded simultaneously on the 5 cortical areas during the trial shown on the bottom. (d) Top: Representative force trace during a single trial in the forelimb active retraction phase. In orange the forelimb position. In blue the force applied by mouse. Red spots are the mice attempts to move the slide. Purple spots are the force peaks associated with slide movements. Black stars show the pulling associated with reward. Bottom: M1 calcium response recorded simultaneously with the force trace shown on top.

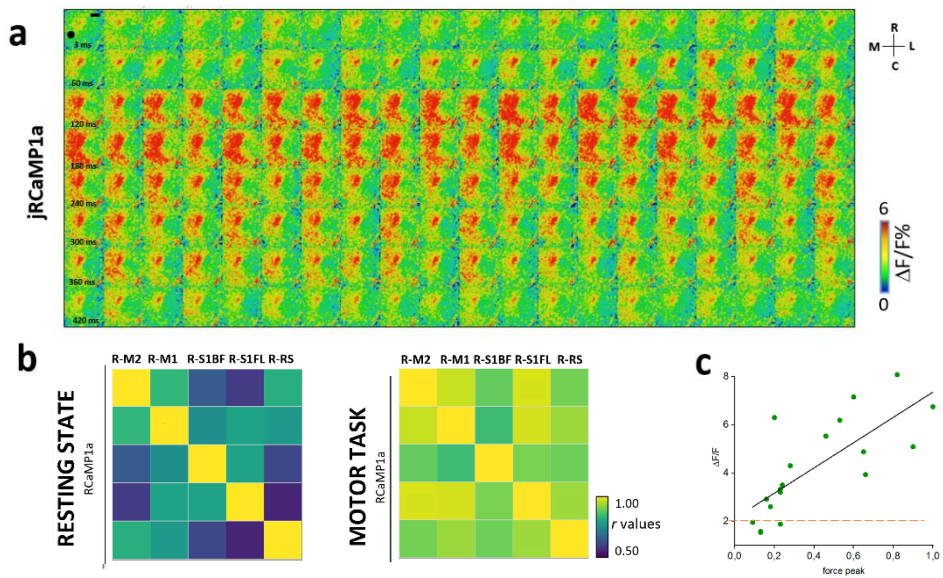


Figure 3.6: Motor task evoked cortical activity (a) Representative image sequence of cortical activation during a rewarded pull over 480 ms. The black dot indicates bregma. Scale bar: 1mm (b) Linear average correlation matrices between five selected ROIs, obtained during both resting state condition (left, $n_{\text{trials}} = 12$) and the last day of motor task execution (right, $n_{\text{trials}} = 12$) in the same mouse. (c) Scatter distribution of the relationship between the M1 fluorescence activity and the corresponding force peak during the last day of training ($n_{\text{mice}} = 1$, $n_{\text{peak}} = 19$). The black line shows the best fit (intercept = 2.1 ± 0.5 , slope = 5 ± 1). Orange dashed line is the threshold, which is measured as the average of M1 maximum activity in resting state condition in the same mouse ($n_{\text{peak}} = 19$; $\Delta F/F = 2.06$). Values reported as average \pm SEM.

several millimetres distant from the injection site (fig3.5a). Moreover, jRCaMP1a sensitivity was strong enough to visualize resting state activity, which we compared to the neuronal activity associated with the execution of a complex movement.

3.2. Development of a crosstalk free mesoscale all-optical system

In the previous chapter we selected the most performing red-shifted GECI for one-photon imaging, jRCaMP1a. In this section, we developed an experimental approach for simultaneous large-scale all-optical manipulation and recording of mouse motor cortex in vivo by combining one-photon imaging of jRCaMP1a with laser stimulation of ChR2.

3.2.1. Experimental design to perform parallel calcium imaging and light-based motor mapping in awake mice

In mice expressing the optogenetic actuator ChR2 in the motor cortex, several classes of limb movements can be evoked depending on the cortical site stimulated (Ayling et al. 2009; Hira et al. 2009; Hira et al. 2015). For investigating large-scale cortical activation dynamics underlying optogenetically evoked-movements with low invasiveness, an all-optical system to simultaneously monitor and manipulate neuronal activity is required. Therefore, we performed a double-path illumination of both AAV9-Syn-jRCaMP1a and AAV9-CaMKII-ChR2, which were transduced on the frontal right cortical hemisphere. The illumination system was integrated into a custom-made wide-field fluorescence microscope allowing laser stimulation of the opsin and cortical imaging of the red-shifted GECI (fig.3.7a).

Achieving a wide and stable expression of the all-optical system was crucial to perform reliable mesoscale motor mapping and imaging, thus the transfection extension was evaluated along 4 weeks starting from the second week after the viral injection. The FWHM of the spatial fluorescence profiles were measured for two mediolateral planes which crossed the injection sites (fig.3.7b, data in table 3;

n=7). Consistent with other results in this study, chapter 3.1. (Montagni, Resta, Conti, et al. 2019), ChR2 and jRCaMP1a showed a highly stable and wide expression over time that covered all the motor cortices of the right hemisphere. Besides, to finely quantify the expression profile of synapsin-targeted jRCaMP1a in cortical neurons, brain slices of transfected mice (4 weeks after viral injection) were stained with the neuronal marker NeuN, revealing that the jRCaMP1a⁺ neurons were 70.2 ± 4.9 % of all labeled cells (fig3.8; n=4). In conclusion, these results suggested that the double transduction of ChR2 and jRCaMP1a was wide enough to cover distinct cortical areas over the motor cortex. Moreover, the expression levels of both jRCaMP1a and ChR2 were maintained stable several weeks after injection.

3.2.2. Wide-field imaging of jRCaMP1a does not induce ChR2 cross-activation

For evaluating the cross-activation of ChR2 during wide-field one-photon imaging of jRCaMP1a (LED 595 nm), the local field potential (LFP) in layer 5 (L5) of jRCaMP1a+/ChR2+ mouse motor cortex was recorded during a randomly started pattern of led ON / led OFF (2 seconds each, 4,5 mW). Peristimulus analysis (-2 s to +2 s from the LED ON trigger) showed no changes in the average LFP signal (fig3.9a, $n_{\text{stimuli}} = 10$; black line = average signal). Moreover, the normalized power content of the standard neurophysiological spectral bands, δ , θ , α , β and γ did not show significant difference (δ OFF = 0.377 ± 0.110 ; δ ON = 0.531 ± 0.169 ; θ OFF = 0.182 ± 0.106 ; θ ON = 0.182 ± 0.105 ; α OFF = 0.027 ± 0.016 ; α ON = 0.047 ± 0.026 ; β OFF = 0.043 ± 0.024 ; β ON = 0.105 ± 0.071 ; γ OFF = 0.008 ± 0.004 ; γ ON = 0.01 ± 0.007 ; n = 10) (fig3.9b and c), highlighting that there were not relevant neurophysiological alterations caused by imaging cross-activation.

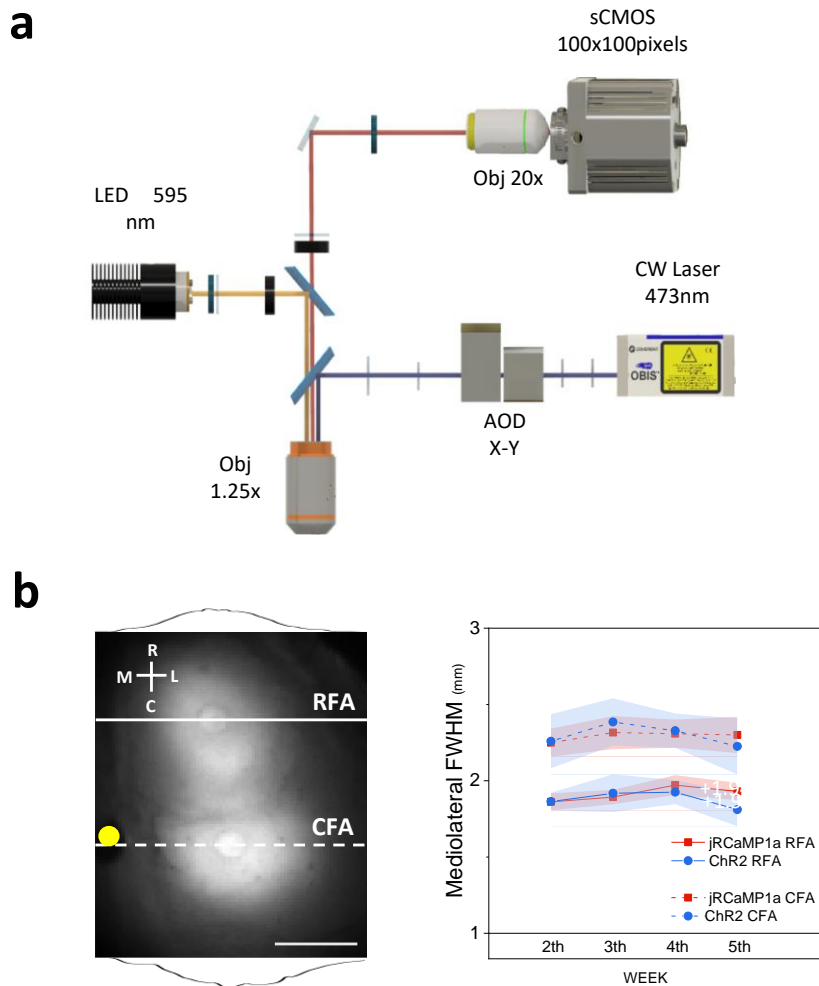


Figure 3.7: *In vivo* experimental design validation. (a) Schematic representation of the wide-field fluorescence microscope implemented by the double-path illumination system. (b) Left, representative image of *in vivo* jRCaMP1a spatial distribution. The fluorescence profile along the medium-lateral plane is reported for both the injection sites (RFA and CFA, on the top and on the bottom of the image respectively). Right, *in vivo* FWHM of jRCaMP1a (red) and ChR2 (blue) spatial distribution along two mediolateral planes passing through RFA ($n = 7$; solid line) and CFA ($n = 7$; dashed line) injection site respectively. Values reported as average \pm SEM. Black dot is the bregma. Scale bar, 1 mm.

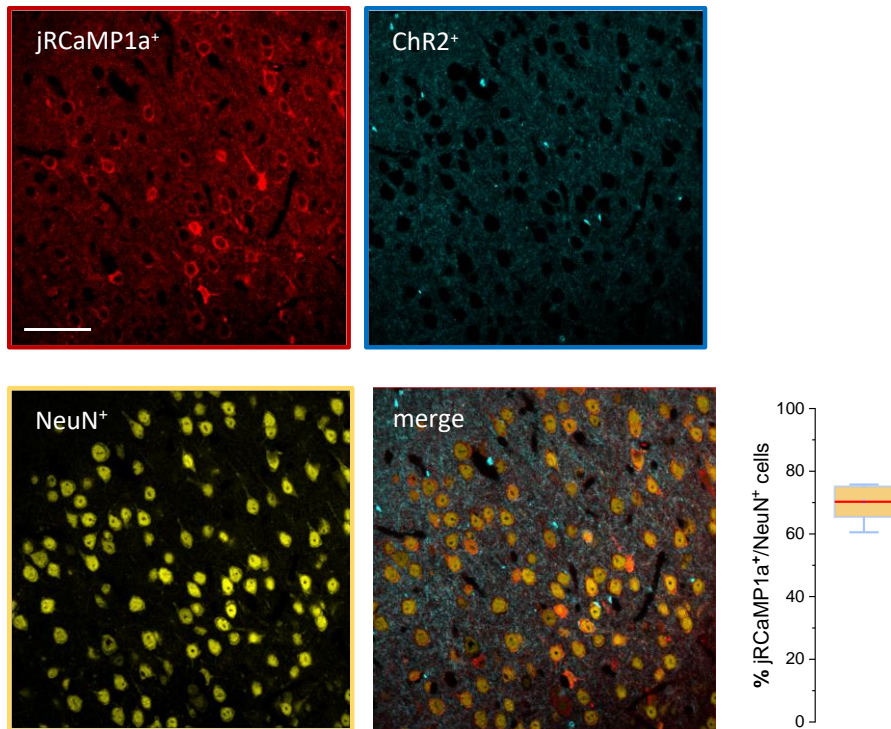


Figure 3.8: Immunohistochemistry quantification. Representative immunohistochemistry images showing the expression of NeuN (yellow), jRCaMP1a (red) and ChR2 (blue) in neurons of the motor cortex. Bottom-right, quantification of the colocalization ratio jRCaMP1a+/NeuN+ (n=4), scale bar = 200 μ m.

3.2.3. Stimulation of ChR2 does not induce alteration of jRCaMP1a fluorescence

Although the reduced crosstalk between ChR2 and jRCaMP1a was already demonstrated in a 2P configuration (Forli et al. 2018), we evaluated whether the laser (473 nm) used for optogenetic stimulation altered the jRCaMP1a signal at mesoscale level. Single laser pulses at increasing intensity were delivered in both mice expressing (jRCaMP1a⁺/ChR2⁺) or lacking the optogenetic actuator (jRCaMP1a⁺/ChR2⁻) (fig3.10a). Our results showed a clear asymptotic increase of the jRCaMP1a response in jRCaMP1a⁺/ChR2⁺ mice (0.2 mW = $0.7 \pm 0.1 \Delta F/F$; 1.3 mW = $2.5 \pm 0.5 \Delta F/F$; 2.5mW = $3.7 \pm 0,6 \Delta F/F$; 5.2 mW = 4.8 ± 0.7 ; 7.6 mW = 5.4 ± 0.7 ; 13.2 mW = $6.1 \pm 0.6 \Delta F/F$; 21.1 mW = $6.8 \pm 0.7 \Delta F/F$; n = 8). Conversely, there was not jRCaMP1a response up to 20mW of laser pulse in jRCaMP1a⁺/ChR2⁻ mice (0.2 mW = $0.118 \pm 0.429 \Delta F/F$; 1.3 mW = $-0.259 \pm 0.213 \Delta F/F$; 2.5 mW = $-0.068 \pm 0.007 \Delta F/F$; 13.2 mW = $-0.088 \pm 0.058 \Delta F/F$; 21.1 mW = $0.156 \pm 0.248 \Delta F/F$; n = 2). We also evaluated the jRCaMP1a maximum response to single pulse optogenetic stimulation over weeks in jRCaMP1a⁺/ChR2⁺ mice (fig3.10c; data in table 4). Our results showed that calcium response to optogenetic stimulation did not change between weeks highlighting a long-term stability of both the calcium indicator and the optogenetic actuator. In conclusion, we confirmed that the double expression of jRCaMP1a and ChR2 combined with single-photon wide-field represented a stable and cross-activation free mesoscale all-optical system.

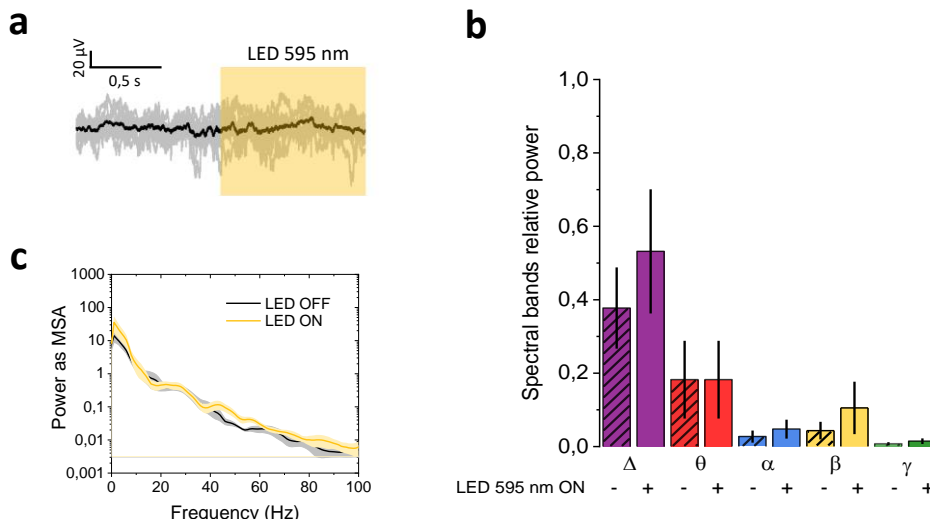


Figure 3.9: ChR2 cross-activation during jRCaMP1a wide-field imaging. (a) Representative traces showing the LFP signal (gray; $n = 10$) during 2 s of stimulus (LED ON) period (average trace in black). (b) Bar graph showing the spectral band relative power quantification during 2 s of peri-stimulus period ($n = 4$ mice; 10 stimuli per mice). Columns represent the averaged relative power for LFP frequency bands (Δ ; θ ; α ; β ; γ) during the dark period (-2 - 0 s; patterned) and the LED ON period (0 - 2 s; monochrome). (c) Representative averaged LFP power spectrum in the dark period (grey) and during the LED ON stimulus (Yellow). Data are presented as means \pm SEM, for frequency bands comparison two-way ANOVA with Bonferroni post-hoc test was used.

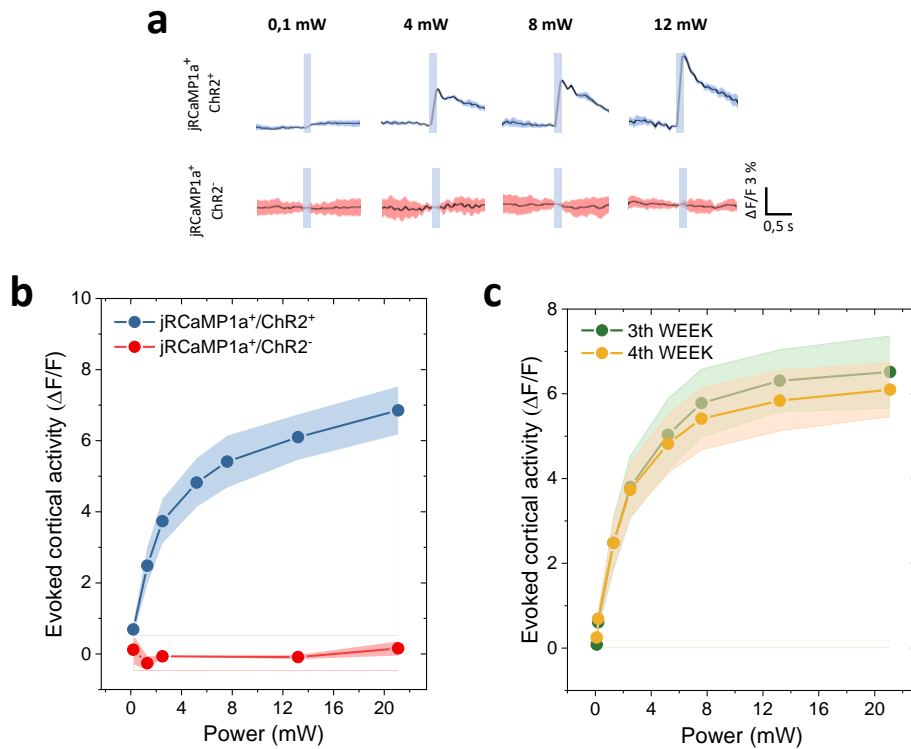


Figure 3.10: jRCaMP1a cross-activation during optogenetic stimulation. (a) Representative traces showing the average calcium response (black) and the SEM (shadows) at increasing laser power (0,1 – 12 mW) in mice expressing jRCaMP1a + Chr2 (blue) and only jRCaMP1a (red). (b) Correlation of evoked calcium activity and single pulse laser power in mice expressing jRCaMP1a⁺/Chr2⁺ (blue; n = 8) and jRCaMP1a⁺/Chr2⁻ (red; n = 2). (c) Correlation of the calcium activity evoked by single pulse laser stimulation between the third (green) and the fourth (yellow) week after injection in jRCaMP1a⁺/Chr2⁻ mice. Data are presented as means \pm SEM.

Table 3. *In vivo FWHM of jRCaMP1a and ChR2 spatial distribution along two mediolateral planes passing through RFA and CFA. Values reported as average \pm SEM*

	Week			
	3 th (mm)	4 th (mm)	5 th (mm)	6 th (mm)
RFA - jRCaMP1a	1.86 \pm 0.06	1.89 \pm 0.05	1.97 \pm 0.07	1.92 \pm 0.06
RFA - ChR2	1.86 \pm 0.06	1.92 \pm 0.12	1.93 \pm 0.08	1.81 \pm 0.11
CFA - jRCaMP1a	2.25 \pm 0.09	2.32 \pm 0.11	2.31 \pm 0.09	2.30 \pm 0.12
CFA - ChR2	2.26 \pm 0.18	2.38 \pm 0.16	2.23 \pm 0.11	2.22 \pm 0.18

Table 4. *jRCaMP1a maximum response to single pulse optogenetic stimulation over weeks in jRCaMP1a+/ChR2+ mice. Values reported as average \pm SEM*

	Laser power					
	0.2mW	2.5mW	5.2mW	7.6mW	13.2mW	21.2mW
WEEK 3th						
$\Delta F/F$ (%)	0.7 \pm 0.1	3.7 \pm 0.6	5.0 \pm 0.8	5.9 \pm 0.7	6.3 \pm 0.7	6.5 \pm 0.7
WEEK 4th						
$\Delta F/F$ (%)	0.7 \pm 0.2	3.8 \pm 0.6	4.8 \pm 0.7	5.4 \pm 0.7	5.8 \pm 0.7	6.1 \pm 0.6

3.3. Mapping movement-specific spatiotemporal cortical activation

CFA and RFA of the motor cortex play critical roles in complex movement generation. In this section, we exploited the wide-field all-optical approach validated in the previous chapters to causally investigate both the functional connectivity between RFA and CFA and the cortical activity patterns driving two different optogenetically-evoked complex movements, a grasp-like movement and a locomotion-like movement.

3.3.1. Mesoscale movement-specific calcium dynamics detected by light-based motor mapping

Using the mesoscale all-optical system developed in the past chapters has been possible to study cortical activity dynamics underlying optogenetically-evoked complex movements in awake mice transduced with AAV9-Syn-jRCaMP1a and AAV9-CaMKII-ChR2 on the right cortical hemisphere.

To map the cortical representation of two evoked complex movements (GRASP and TAP), we used a stimulation pattern composed of 10 ms of laser pulse at a frequency of 16 Hz for 2 s. Light-based motor mapping started from the stereotaxic references for the Rostral Forelimb Area (RFA; + 2 mm AP, +1.25 mm LM) and the Caudal Forelimb Area (CFA; + 0.25 mm AP, + 1.5 mm LM) that are reported to induce the GRASP and the TAP forelimb movements respectively (Tennant et al. 2011; Hira, Ohkubo, Ozawa, et al. 2013; Hira et al. 2015). Stimulation with increasing laser power was used to identify the mouse-specific minimum power required to elicit a clear motor behavior in a 2 s stimulation session (fig.3.11a and

b). Although there was high variability of the minimum laser power between mice (fig3.11c, from 1.3 mW to 13.2 mW), our results showed a limited variability in the evoked-calcium response highlighting instead a stereotyped and reproducible spatiotemporal propagation of calcium dynamics across mice per movement (fig3.11c; GRASP average $\Delta F/F_{\text{peak}} = 15.5 \pm 1\%$; TAP average $\Delta F/F_{\text{peak}} = 12.7 \pm 1\%$; $n = 11$). The wide range of laser power required across mice was probably ascribable to both biological differences and ChR2 local concentration. Subsequently, to assess a correlation between the laser power and the evoked-calcium response intensity, the optogenetically-evoked jRCaMP1a peak amplitude recorded from a ROI centred in the stimulation site was related to the laser power used. Interestingly, no linear relationship was observed across subjects (fig.3.12a; $\text{TAP}_{\text{intercept}} = 16.7 \pm 1.8$; $\text{TAP}_{\text{slope}} = -0.3 \pm 0.4$; $\text{GRASP}_{\text{intercept}} = 11.4 \pm 1.7$; $\text{GRASP}_{\text{slope}} = 0.2 \pm 0.2$; $n = 11$). The mouse- and movement-specific minimum laser power was then used to perform light-based motor mapping of GRASP and TAP cortical representations. Mouse-specific LBMMs were aligned and overlaid for evaluating the mean position of the LBMM center of gravity per movement category (fig.3.12b; $\text{GRASP}_{\text{RC}} = 1.8 \pm 0.2$ mm; $\text{GRASP}_{\text{LM}} = 1.8 \pm 0.2$ mm; $\text{TAP}_{\text{RC}} = -1 \pm 0.2$ mm; $\text{TAP}_{\text{LM}} = 1.6 \pm 0.2$ mm; $n = 8$).

3.3.2. Distinct functional modules are involved in the processing of optogenetically evoked movements within motor cortex

To study the cortical activation feature underneath the optogenetically-evoked complex movements, Maximum Intensity Projections (MIPs) of the calcium dynamic recorded during the optogenetic-stimulation of both GRASP and TAP

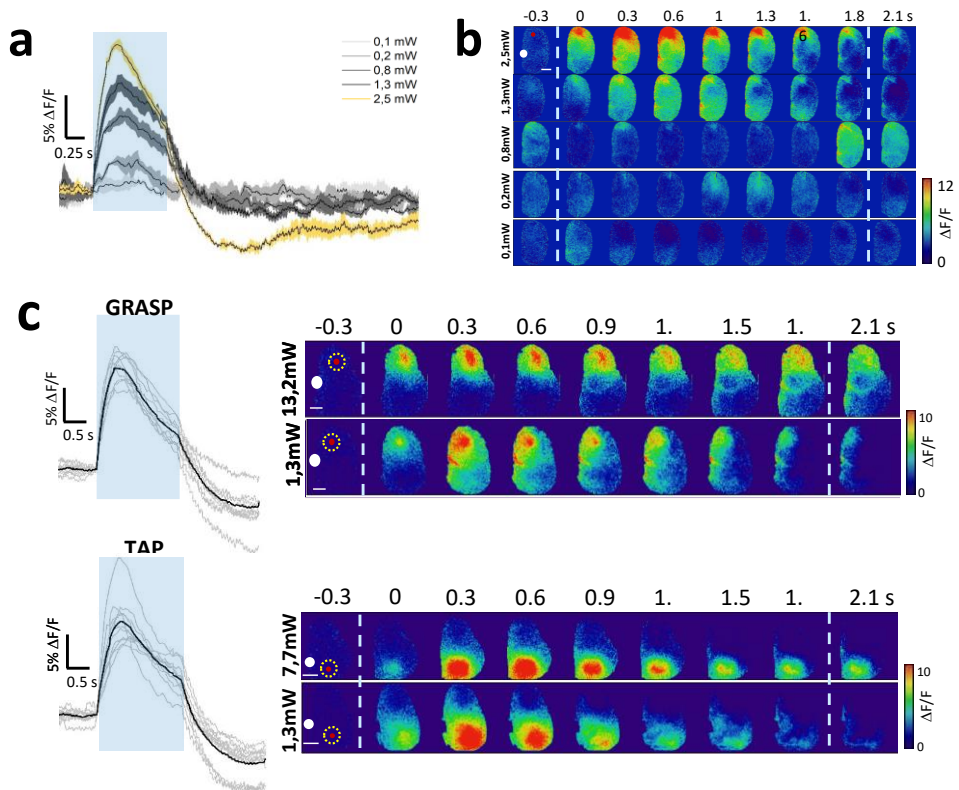


Figure 3.11: Large scale calcium dynamics during light-based motor mapping are movement-specific (a) Representative average calcium responses to the optogenetic stimulus train (10 ms on; 16 Hz; 2 s) at increasing laser powers. Yellow line represents the calcium response associated with the minimum laser power necessary to evoke complex movement. Blue shadow = stimulation period. (b) Representative wide-field image sequences of cortical activation at different laser powers. White dot indicates bregma. Red dot is the site of stimulus. Dashed lines show the stimulus period. Scale bar = 1 mm. (c) Left, Calcium responses at the minimum laser power in different animals. Mean calcium response per movement category in black, (TAP, n=11; GRASP, n=11). Right, representative image sequences of cortical activation at minimum evoking power in two opposite cases (low and high power. Red dot is the site of stimulus. Dashed lines show the stimulus period. Yellow dashed dots are the ROI analyzed. White dot is bregma. Scale Bar, 1mm.

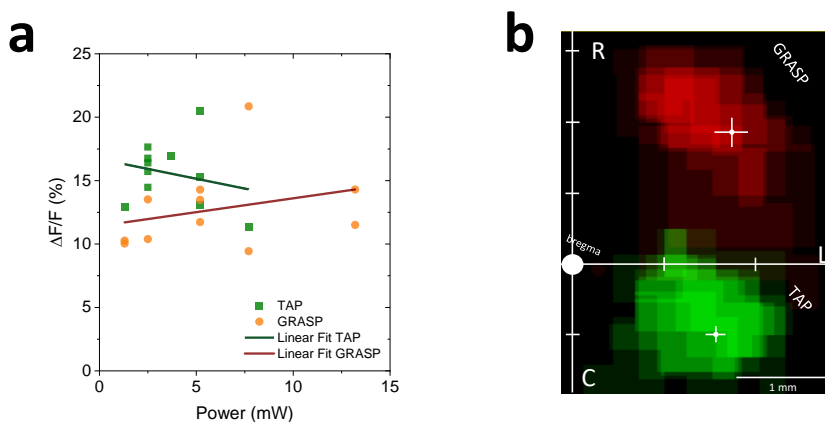


Figure 3.12: Cortical dynamics are not influenced by laser power variability across mice. (a) Linear regression between calcium peak amplitude and minimum evoking power for TAP ($n = 11$; green) and GRASP ($n = 11$; orange) (b) Average light-based motor maps of the right hemisphere motor cortex. Grasping-like movement in red and locomotion-like movement in green. Withe crosses represent the mean centres of gravity respect to bregma, the variability of the coordinates (standard error) are represented by the lengths of the crossbars (TAP, $n=8$; GRASP, $n=8$).

movements were obtained (fig.3.13). Average MIP obtained stimulating all the site inside the LBMM (fig3.13a; e.g. RFA or CFA) were subtracted from that obtained stimulating the close no-movement-evoking points outside the map boundary (fig3.13b) and the resulting difference was considered the movement-specific activity map (MSAM) per mouse (fig3.13c). Based on these criteria, the area dimension of each individual map was evaluated. Interestingly, no significant difference between MSAM and LBMM area dimension has been showed per movement category (fig3.14c; $MSAM_{TAP} = 0.53 \pm 0.06 \text{ mm}^2$; $LBMM_{TAP} = 0.40 \pm 0.04 \text{ mm}^2$; $n_{TAP} = 8$; $MSAM_{GRASP} = 0.48 \pm 0.06 \text{ mm}^2$; $LBMM_{GRASP} = 0.64 \pm 0.14 \text{ mm}^2$; $n_{GRASP} = 7$). In addition, the analysis of the MSAM and LBMM centre of gravity per movement category revealed a strong overlap between them across mice ((fig3.14b; data in table 5). These results suggested a spatial localized recruitment of brain areas overlapping with the LBMM per movement category. Consequently, the overlap percentage between MSAM and its related LBMM was quantified by assessing how much of the activation map was involved in the optogenetic map and vice versa (fig3.14d; $\text{Overlap } TAP_{MSAM/LBMM} = 54 \pm 5 \%$; $\text{Overlap } TAP_{LBMM/MSAM} = 69 \pm 3 \%$; $\text{Overlap } GRASP_{MSAM/LBMM} = 67 \pm 12 \%$; $\text{Overlap } GRASP_{LBMM/MSAM} = 55 \pm 4 \%$). Combined, these results consistently showed that the cortical activity elicited during the optogenetically driven forelimb movements was bounded in areas that overlapped with their light-based cortical representations. Overall, our data suggest that the movement-specific cortical connectivity is bounded on discrete functional modules centered on the related LBMMs.

Table 5. Centres of mass coordinates for the light-based movement maps and the movement specific activation maps of both GRASP and TAP. Values reported as average \pm SEM.

Centre of gravity coordinates				
(mm)	MSAM _{RC}	MSAM _{LM}	LBMM _{RC}	LBMM _{LM}
GRASP	1.9 \pm 0.2	1.7 \pm 0.1	1.8 \pm 0.2	1.7 \pm 0.2
TAP	-1.0 \pm 0.2	1.5 \pm 0.1	-1.0 \pm 0.2	1.6 \pm 0.2

Table 6. Centres of mass coordinates for the light-based movement maps and the movement specific activation maps of both GRASP RFA and GRASP LFA. Values reported as average \pm SEM

Centre of gravity coordinates				
(mm)	MSAM _{RC}	MSAM _{LM}	LBMM _{RC}	LBMM _{LM}
GRASP RFA	1.7 \pm 0.1	1.9 \pm 0.2	2.0 \pm 0.2	1.7 \pm 0.2
GRASP LFA	0.6 \pm 0.2	2.1 \pm 0.1	0.6 \pm 0.1	2.3 \pm 0.6

Table 7. Multiple comparison between GRASP LFA MSAM and LBMM with the other movement category maps. Values reported as average \pm SEM

Overlap				
%	MSAM	MSAM	LBMM	LBMM
	TAP	GRASP RFA	TAP	GRASP RFA
LBMM GRASP LFA	1 \pm 1	9 \pm 5	3 \pm 2	0 \pm 1
MSAM GRASP LFA	10 \pm 6	20 \pm 7	20 \pm 9	12 \pm 5

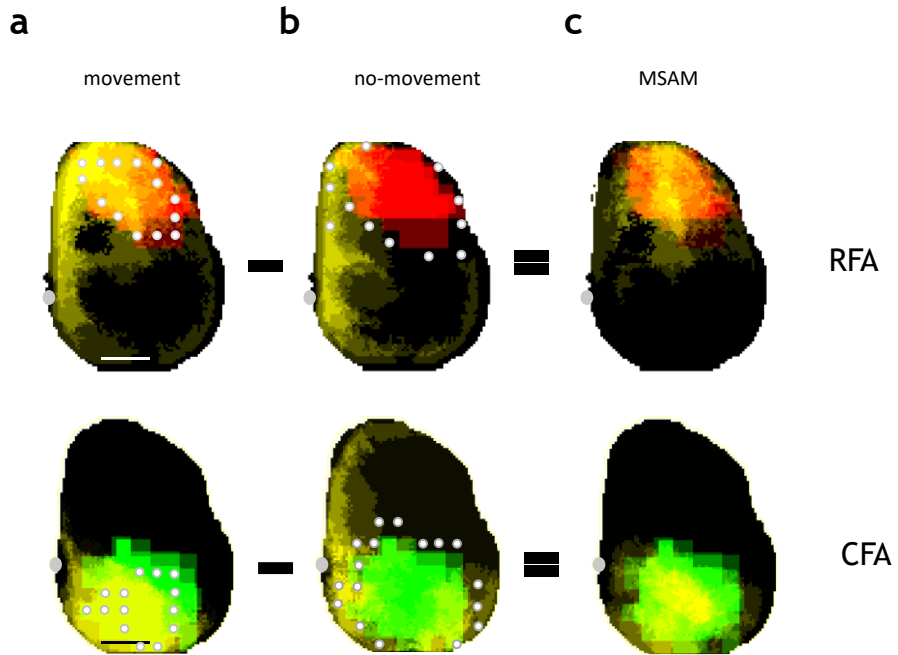


Figure 3.13: Process for obtaining the movement-specific activity maps (MSAMs). (a) Average calcium dynamic (yellow) obtained by stimulating the internal perimeter (white dots) of the LBMM (red, GRASP; green, CFA). (b) Average calcium dynamic (yellow) evoked by stimulating no-movement points (whited dots) outside the LBMM (red, GRASP; green, TAP). (c) Representative movement-specific activity map (MSAM) obtained by subtracting no-movement related average calcium dynamic from that obtained stimulating inside the LBMM (red, GRASP; green, TAP).

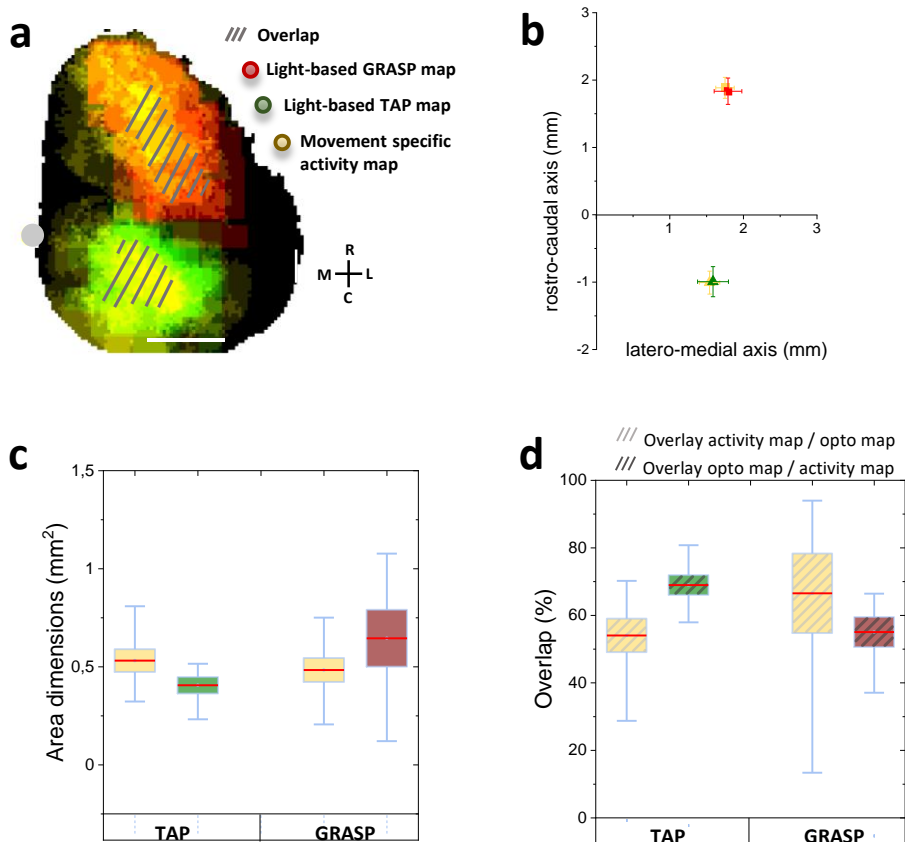


Figure 3.14: Discrete modules of movement-specific cortical connectivity are centered on their relative LBMM. (a) Representative scheme of average movement light-based representations (TAP, red; GRASP, green) and related average activity maps (yellow). Gray dot is bregma. Scale bar = 1 mm (b) Centres of mass of light-based movement maps (TAP, red, n=8; GRASP, green, n=7) and movement specific activity maps (yellow). (c) Quantification of the LBMM (TAP, green; GRASP, red) and activity maps (yellow) area dimensions. (d) Quantification of the overlay between MSAM (yellow) and its related LBMM (light grey pattern) and vice versa (dark grey pattern, TAP, green; GRASP, red). Red lines correspond to means, boxes show the standard error range, whiskers length are the extreme data points.

3.3.3. Identification of a distinct grasping representation module: The Lateral Forelimb Area (LFA)

Although optogenetically-evoked movements were elicited in areas corresponding canonically to the RFA and CFA, our light-based motor mapping revealed two distinct GRASP expressing areas in half of the mice analyzed (fig3.15a). One area was located in the frontal position and perfectly matched the RFA. The other one was well separated from the first one. It was near to the lateral border of the CFA and we named it as the lateral forelimb area (LFA) (fig3.15a). In the remaining subjects (4 out of 8) a single larger map, covering both the areas, was observed (fig3.14a). To understand if the distinct more lateral GRASP representation was an extension of the RFA or represented a distinct module, we analyzed the spatial features of the movement-related cortical activity evoked on two GRASP motor maps, which were named GRASP RFA and GRASP LFA respectively. Consequently, in those animals presenting a single larger area, we split it into two smaller ones (see methods for segmentation criteria) and both MSAMs and their related LBMMs were re-analyzed considering the LFA as a discrete GRASP representation (fig3.15). Our results showed that, as for RFA and CFA, the LFA MSAM presented a strongly overlapping centre of gravity with that of his related LBMM. Moreover, both of LFA maps centre of gravity were drastically separated from those of the other areas reinforcing the hypothesis of separate modules (fig.3.15b; data in table 6). The areas dimension did not present significant differences (fig.3.15c; $MSAM_{GRASP\ RFA} = 0.44 \pm 0.06\ mm^2$; $LBMM_{GRASP\ RFA} = 0.31 \pm 0.07\ mm^2$; $MSAM_{GRASP\ LFA} = 0.61 \pm 0.09\ mm^2$; $LBMM_{GRASP\ LFA} = 0.26 \pm 0.04\ mm^2$). Moreover, the spatial overlap of the LBMM with its related MSAM achieved high percentage values for both the movement category analyzed (fig3.15d; GRASP RFA = $61 \pm 3\ %$; GRASP LFA = $77 \pm 2\ %$), albeit the inverse ratio was lower (fig3.15d; GRASP RFA = $50 \pm 12\ %$; GRASP LFA = $38 \pm 6\ %$).

According to the past observation, these results confirmed a large activation of the LBMM following its point stimulation. In addition, the low overlap between LFA MSAM and LFA LBMM suggested that this grasping representation module expresses wide-spread connectivity. To understand whether the LFA represented a distinct module or it was an extension of the RFA network, we analyzed the LFA connectivity and its relationship with the RFA and CFA maps (fig3.16a and 3.16b, data in table 7). Interestingly, the three MSAM showed a strong spatial segregation, suggesting peculiar cortical connectivity linked to the evoked behavioral output. This result demonstrates that the LFA relates to a wider and specific intracortical connectivity. Which is different from the RFA module that is even avoided. In addition to the strong segregation of the GRASP LFA MSAM, our results also highlighted a spatially distinct representation of its LBMM. Surprising, average calcium transient proprieties evoked inside the GRASP LFA mirrored those evoked in GRASP RFA or TAP (fig.3.17; $\Delta F/F$ TAP = $13.4 \pm 1 \%$; GRASP RFA = $11.1 \pm 1 \%$; GRASP LFA = $11.8 \pm 0.8 \%$). Moreover, the comparison of the average calcium transient elicited inside the GRASP LFA LBMM with that obtained by stimulating the adjacent sites evoking non-specific movements highlighted a significantly different calcium recruitment during complex movements (fig3.17b; TAP: Movement = $13.4 \pm 1.0 \%$ $\Delta F/F$ vs Non-specific movement $8.3 \pm 0.9 \%$ $\Delta F/F$; GRASP RFA: Movement = $11.1 \pm 1.0 \%$ $\Delta F/F$ vs Non-specific movement $6.3 \pm 0.7 \%$ $\Delta F/F$; GRASP LFA: Movement = $11.8 \pm 0.8 \%$ $\Delta F/F$ vs Non-specific movement $8.1 \pm 1.0 \%$ $\Delta F/F$). Taken together these results strengthen our hypothesis of three distinct modules in the motor cortex (RFA, LFA, and CFA) with specific optogenetic maps and effective connectivity.

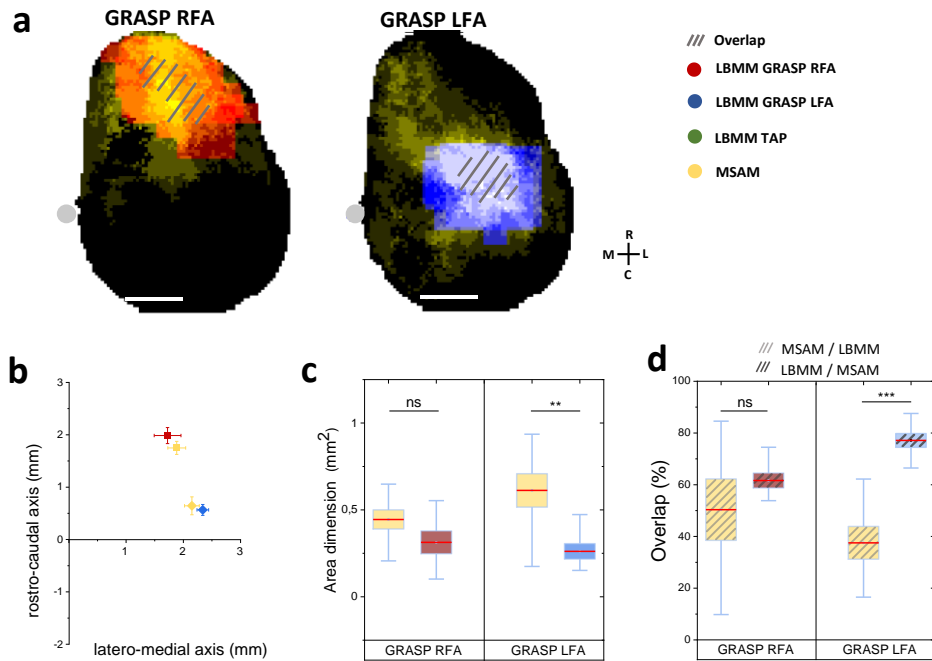


Figure 3.15: Identification of the Lateral Forelimb Area (LFA) as a distinct grasping representation module (a) Representative schemes of LBMM per movement category (left, GRASP RFA in red; right, GRASP LFA in blue) and their related MSAM (yellow). Gray dot is bregma. Scale bar = 1 mm. (b) Centers of mass of light-based movement maps (GRASP RFA, red; GRASP LFA, blue), movement specific activity maps (yellow) and their overlay (gray). (c) Quantification of the area dimensions of the light-based motor maps (GRASP RFA, red; GRASP LFA, blue) and activity maps (yellow) ($n = 7$, $** p < 0,01$ two sample t-test). (d) Quantification of the overlap between MSAM (yellow) and its related LBMM per movement category (GRASP RFA, red; GRASP LFA, blue). Red lines correspond to means, boxes show the standard error range, whiskers length are the extreme data points ($n=7$; $*** p < 0,001$ two sample t-test).

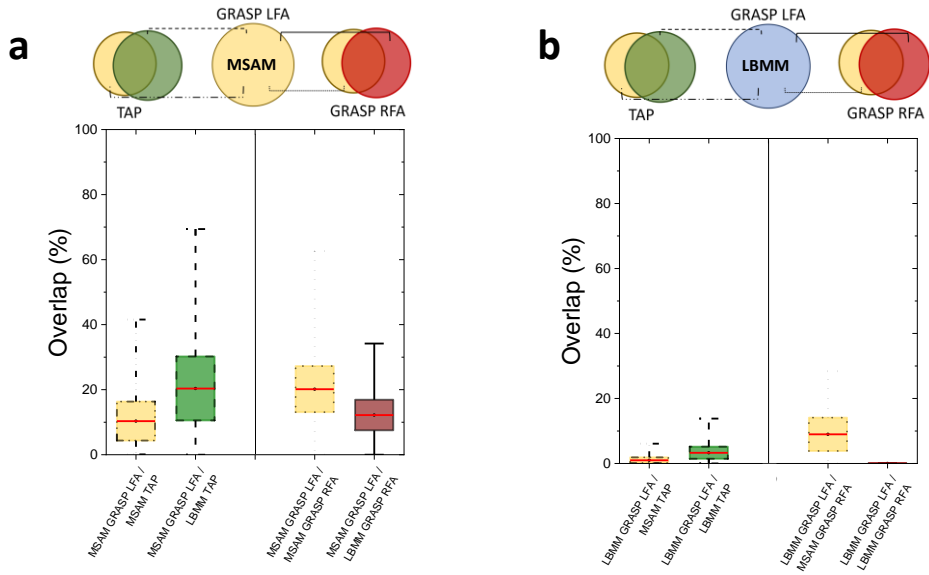


Figure 3.16: Spatial segregation of both LFA LBMM and MSAM. (a) Multiple comparison between GRASP LFA MSAM and the other movement category maps (n = 7). (b) Multiple comparison between GRASP LFA LBMM and the other movement category maps (n = 7).

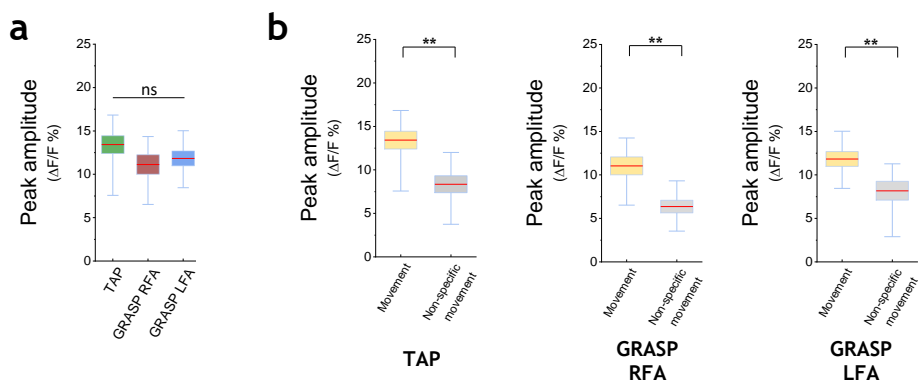


Figure 3.17: Comparison of average calcium transient properties between movement categories. (a) Comparison of evoked calcium transient amplitude between movement categories ($n = 7$, non sign. one-way ANOVA) (b) Comparison of the calcium transient amplitude obtained stimulating within the LBMM (Movement) and outside the LBMM (non-specific movement) per movement classes, $n = 7$, ** $p < 0,01$ two sample t-test.

3.3.4. Optogenetically-evoked GRASP RFA and GRASP LFA movements show similar properties

Since we initially observed that grasp-like movements evoked in RFA or LFA modules were likely the same, we next examined the kinematic properties of the optogenetically-evoked contralateral forelimb movements. For GRASP RFA and GRASP LFA movements, the trajectory of the left-forelimb from its starting position involved an initial displacement mainly towards the midline followed by elevation towards the mouth (fig3.18a and 3.19a), which was often coupled with tongue movements and twisting of the forepaw (fig3.18c). Although, GRASP RFA was slightly wider in the medial-lateral plane than GRASP CFA (fig3.20; GRASP RFA = 12.7 ± 0.9 mm vs GRASP CFA = 11.4 ± 1.6 mm; $n_{\text{mice}} = 1$, $\text{train} = 5$), they achieved the same elevation at the end of the stimulus (GRASP RFA = 8.7 ± 0.7 mm; GRASP CFA = 8.2 ± 0.5 mm). Moreover, the movement onset was exactly the same (fig3.20c; GRASP RFA = 0.10 ± 0.04 s; GRASP CFA = 0.10 ± 0.04 s). For TAP movements instead the forelimb displacement was rhythmic (fig3.18b), spatially localized in the medial-lateral plane (fig3.19 and 3.20a; TAP = 5.1 ± 0.4 mm) and lower than GRASP in elevation (fig3.20b; TAP = 5.3 ± 0.4 mm). TAP movements were also opposite in the medial-lateral directionality (fig3.18a) and showed a slower onset than the two GRASP (fig3.20c; TAP = 0.46 ± 0.07 mm). Moreover, even if the two class of evoked-complex movements showed different spatial properties they were characterized by no significant difference in the average speed (fig3.20d; GRASP RFA = 16.9 ± 0.7 mm/s; GRASP CFA = 18.2 ± 1.0 mm/s; TAP = 15.0 ± 1.2 mm/s; NO-MOV = 1.2 ± 0.2 mm/s). As expected, the irradiation of no-movement-evoking sites in the cortex resulted in a remarkably reduced and non-specific forelimb displacement from its starting position (fig3.20a; Max lateral distance = 3.0 ± 0.8 mm; Max elevation = 0.9 ± 0.5 mm). Indeed, even though this type of movement showed an onset (fig3.20c; NO MOV

= $0,2 \pm 0,07$ mm), it did not involve complex spatial performance if compared to the other movements analyzed (fig.3.18b and c). These results are in accordance with the classification of the GRASP as a forepaw-to-mouth movement, and the TAP as a locomotion-like movement. Moreover, the strong similarity between GRASP RFA and GRASP CFA kinematics suggested the existence of multiple cortical modules evoking the same movement. Finally, stimulation of cortical points outside the LBMMs are related to non-specific forelimb movements.

3.3.5. Complex movements execution is associated with specific spatiotemporal pattern of activity propagation

Spatial analysis of the activation maps highlighted that optogenetically-evoked complex movements were characterized by distinct modules of cortical activation. We then hypothesized that each module was associated with a different, movement-specific flow of activation through the cortex. To investigate this issue, we performed a spatiotemporal propagation analysis of cortical activity obtaining propagation maps that represent the ranked sequence of cortical activation. The associated polar plots describe the propagation direction (fig.3.21). The results showed that during RFA stimulation there was a rapid isotropic activation of the area around the site of stimulus followed by a latero-caudal activation flow as shown in fig.3.21a. A specular rostromedial flow of activation was observed during CFA stimulation (fig.3.21b). Interestingly, LFA stimulation evoked a more complex pattern of cortical activation, which was more isotropic compared to the other two activations, and the analysis pipeline hardly provides a clear direction in the activation flow in this case (fig.3.21c). In addition, the stimulation of

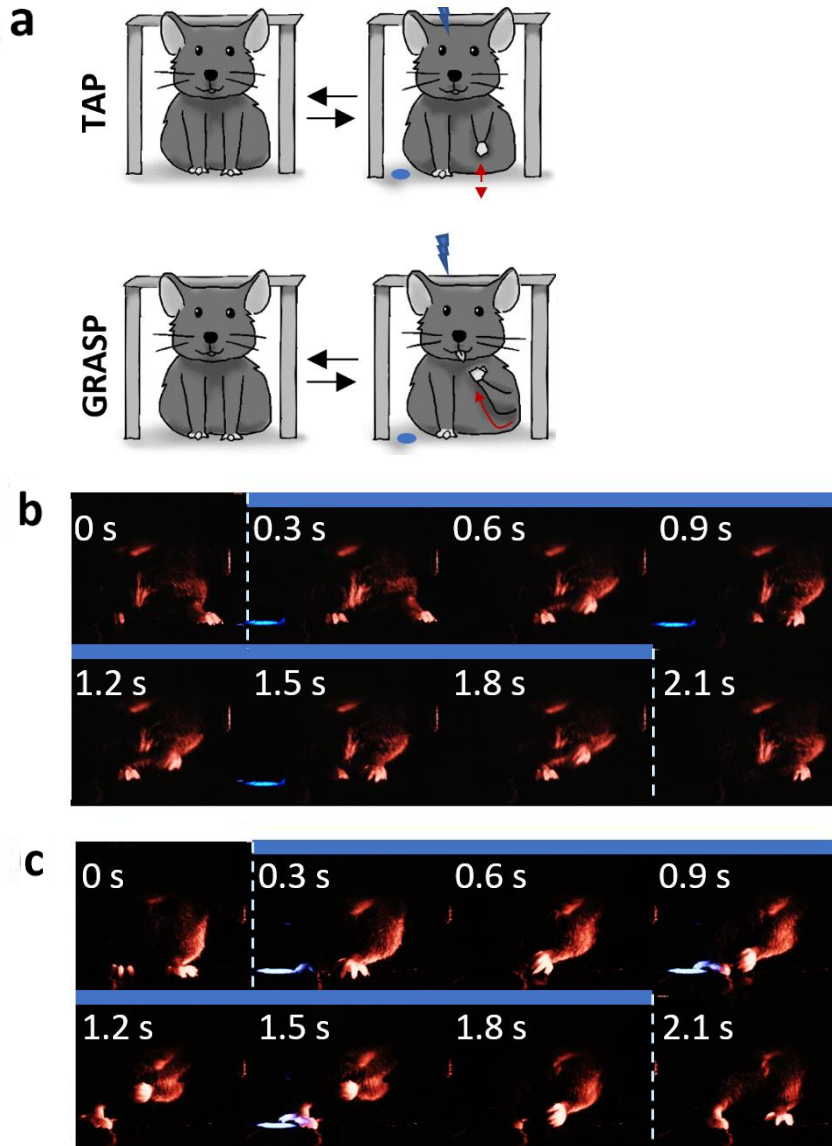


Figure 3.18: *In vivo* optogenetically-evoked movements. (a) Schematic sequence of drawings showing evoked movement (TAP, top; GRASP, bottom). Blue dots are the reflected laser stimuli representation. Red arrows indicate movement trajectories. (b) Example frames from video recording during a tap-like movement. Dashed white lines show and blue bar show the stimulus period. (c) Example frames from video recording during a grasp-like movement. Dashed white lines show and blue bar show the stimulus period.

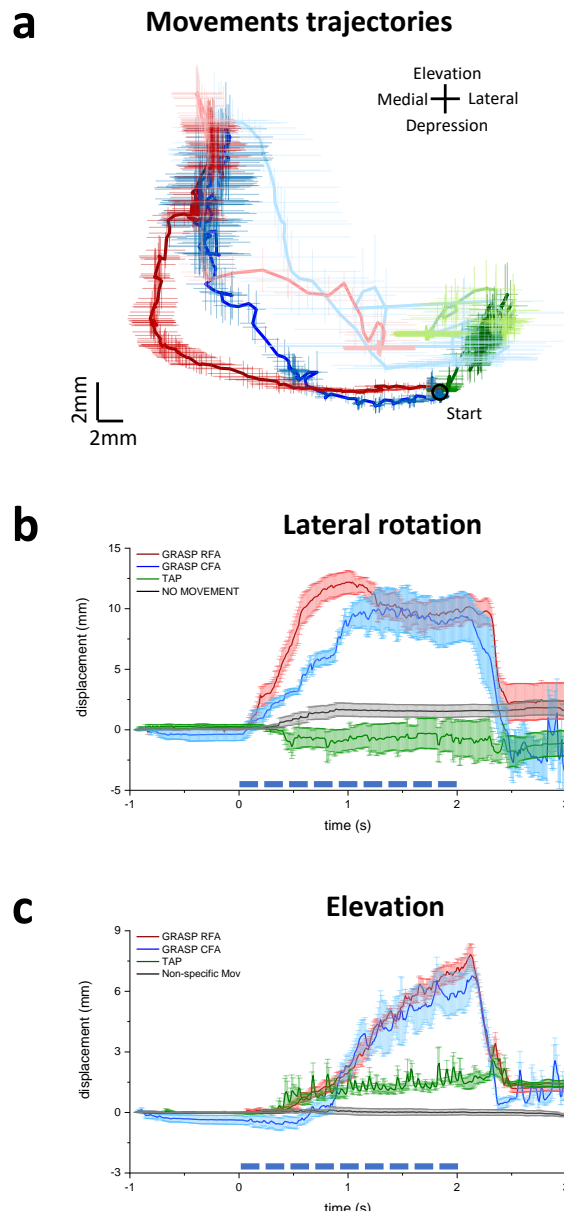


Figure 3.19: Optogenetically-evoked complex movements trajectories (a) Reconstruction of the mean trajectories per movement category evoked by 2 seconds of optogenetic stimulation of specific LBMM (red, GRASP RFA. Blue, GRASP CFA. Green, TAP. Light grey, non-specific movement). The darkest trace shows the movement trajectory during the stimulus period (2s), the lightest trace shows the movement trajectory post stimulation (1 s). Dark circle indicates the forelimb start point. Error bars are SEM. (b) Mean forelimb displacement along the x-axis for movements showed in a. Dashed blue line indicates the stimulus period. (c) Mean forelimb displacement along the y-axis for movements showed in a. Dashed blue line indicates the stimulus period.

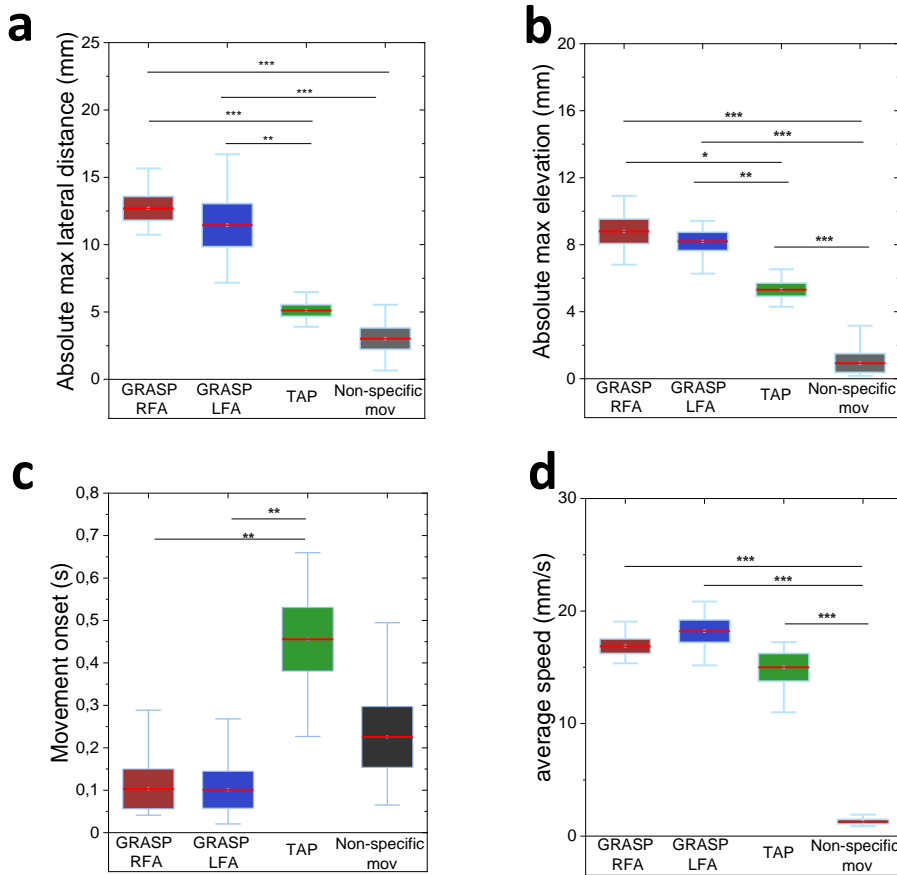


Figure 3.20: Optogenetically-evoked GRASP RFA and GRASP LFA are characterized by similar dynamics in space. (a) Box and whisker plots show the absolute maximum distance along the x-axis per movement category (red, GRASP RFA; Blue, GRASP CFA; Green, TAP; Light grey, non-specific movement). (b) Comparison of the absolute maximum elevation along the y-axis per movement category showed in a. (c) Onset profile per movement category showed in a. (d) Average speed recorded during the stimulus period (2 seconds) per movement category. Asterisks indicate significances: * $P < 0.05$, ** $P < 0.01$, *** $P < 0.001$ (P-value adjusted according to Bonferroni).

no-movement-evoking sites showed a drastically reduced spread of activation, compared with the results obtained by stimulation of complex movements-evoking sites, coupled with an unclear direction of propagation (fig.3.21d). Overall, these results revealed that different complex movements were linked with specific spatiotemporal patterns of activity propagation, reinforcing the hypothesis that LFA relates to a specific grasping evoking module. In addition, these results showed that movement-related cortical areas stimulation led to a larger flow of activation compared to non-movements-evoking areas, suggesting the persistence of a more complex cortico-cortical connectivity associated with movement execution.

3.3.6. Connectivity features associated with evoked complex movements are disrupted by excitatory synaptic block

Spatiotemporal analysis showed in the past chapters suggested a progressive engagement of specific regions in the motor cortex underlying complex movements execution. A common strategy to dissect the role of different functional nodes in a neuronal network is the pharmacological synaptic transmission interference, in particular using glutamatergic excitatory transmission antagonist (Vinokurova et al. 2018). To investigate both the module local connectivity and the reciprocal modules interaction during optogenetic-evoked movement execution, we performed a module-specific block of the excitatory synaptic transmission using topical application of the AMPA/kainate receptor antagonist 6-cyano-7-nitroquinoxaline-2,3-dione (CNQX) on the cortical surface (fig3.22a) (Harrison et al. 2012; Spalletti et al. 2017). Our results showed that CNQX application in RFA reduced the extension of the GRASP RFA activated

area (fig3.22b; Activated area_{vehicle} = $0.058 \pm 0.013 \text{ mm}^2$ vs 30' Activated area_{CNQX} = $0.026 \pm 0.014 \text{ mm}^2$; $p = 0.043$; $n = 3$) and slightly slows down the activation dynamics (fig3.22c; Peak amp_{vehicle} = $14.72 \pm 4.20 \Delta F/F$; Peak amp_{CNQX} = $11.62 \pm 3.66 \Delta F/F$, $p = 0.042$; $n = 3$). Similar results were obtained by applying CNQX in CFA (fig3.22b-c; Activated are_{vehicle} = $0.12 \pm 0.01 \text{ mm}^2$ vs 30' Activated area_{CNQX} = $0.093 \pm 0.026 \text{ mm}^2$; $p = 0.044$; Peak amp_{vehicle} = $25.80 \pm 1.31 \Delta F/F$; Peak amp_{CNQX} = $21.26 \pm 0.63 \Delta F/F$, $p = 0.044$; $n = 3$). Moreover, the effect of the local block of the excitatory synaptic transmission on the movement-specific spatiotemporal features of cortical activation (fig3.23a) was assessed analyzing the median (med) and the interquartile range (IQR) of the pixel rank distribution on a ROI obtained by overlapping the light-based motor map, before and after CNQX application (fig3.23b; GRASP-med_{vehicle} = 3.5; GRASP-med_{CNQX} = 4.0; GRASP-IQR_{vehicle} = 3.0; GRASP-IQR_{CNQX} = 4.5; TAP-med_{vehicle} = 1.5; TAP-med_{CNQX} = 2.0; TAP-IQR_{vehicle} = 0.5; TAP-IQR_{CNQX} = 1.0; $p = 0.0001$; $n = 3$). These results highlight an increase in both the median and IQR after the pharmacological interference for both movements suggesting a slower and more disorganized propagation of the cortical activity respectively. Interestingly, these results correlate with the behavioral outcome disruption caused by the pharmacological interference (fig.3.23c). Indeed, as previously reported by Harrison et al., 2012, CNQX application leads to faults and distortions in movement execution, until the complete extinction of a clearly recognizable complex movement. As summarized in fig.3.23c CNQX application in RFA resulted in a block of grasping-like execution while preserving the CFA-evoked locomotion-like movement and vice versa. Taken together these results demonstrated that optogenetic stimulation of movement representation areas was not enough to generate a correct movement execution but rather an effective cortico-cortical connectivity was required to evoke motor behaviours and that GRASP RFA and TAP were driven by two independent cortical modules.

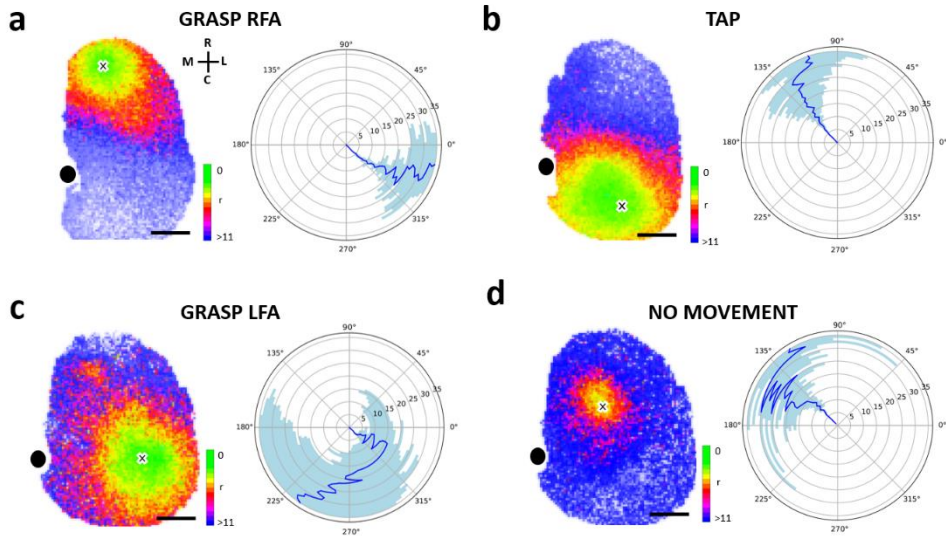
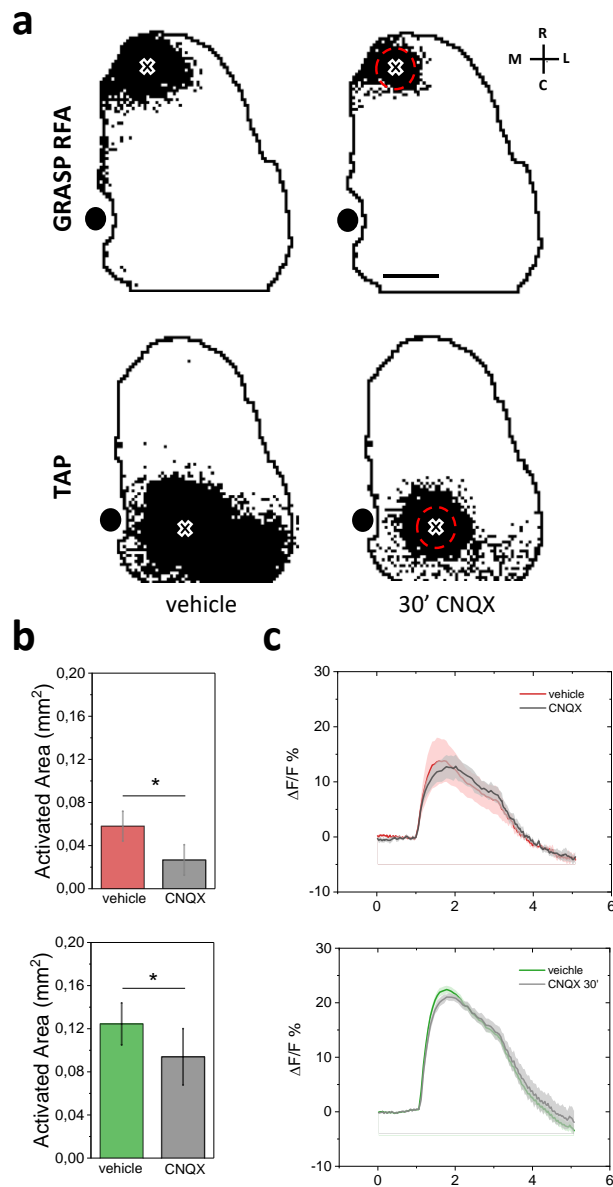


Fig.3.21: Cortical activity propagation analysis reveals movements-specific spatiotemporal activation maps and flow direction. (a) Left panel, average map of the spatiotemporal activity propagation during GRASP RFA stimulation. Right, polar plot, centred on the stimulation site, showing the average propagation direction. Radius-dependent circular mean and circular standard deviation in blue. As in (a) spatiotemporal activity propagation maps and polar plots are shown in (b), (c) and (d) for TAP, GRASP LFA and in a no-evoking-movement site respectively. Black dot represents bregma. Scale bars = 1 mm. Color bar = pixel ranks from 0 to >11.

**Figure**

3.22: Local connectivity is disturbed by excitatory synaptic block. (a) Representative MIP showing cortical activation during vehicles (left) and 30' after CNQX application (right) in RFA (top) and CFA (bottom). The cross represents the stimulus site. The red dot shows the CNQX injection site. (b) Quantification of the effect of CNQX topical application on MSAM extension in RFA (top) and CFA (bottom). (c) Averaged evoked calcium transients profile in vehicle and following CNQX topical application in RFA (top) and CFA (bottom). Shadows represent the s.e.m. Asterisks indicate significances: * $P < 0.05$.

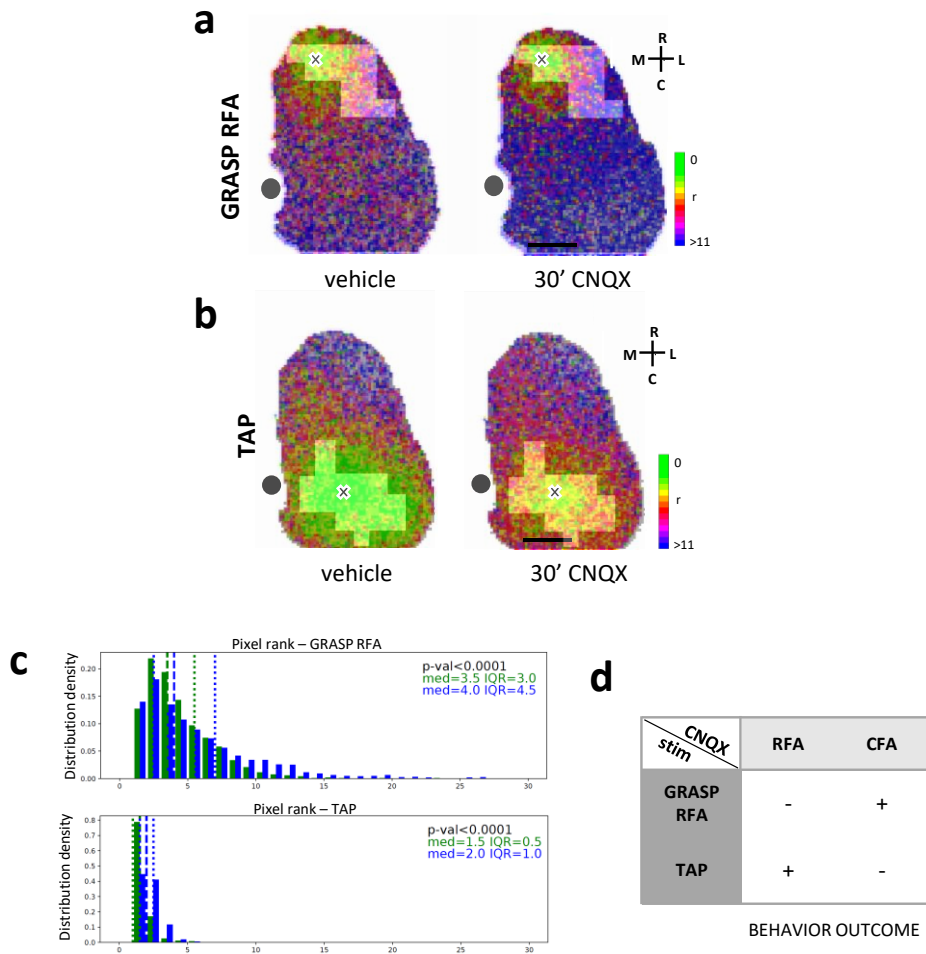


Figure 3.23: Excitatory synaptic block leads to complex movement interference. Representative activity propagation maps of GRASP RFA (**a**) and TAP (**b**) showing the effect of CNQX topical application. Bright areas represent the LBMM. Scale bar = 1 mm. Color bar = pixel ranks from 0 to <11. Grey dot represents bregma. (**c**) Pixel rank distribution of the region corresponding to the LBMM (bright) for GRASP RFA (top) and TAP (bottom), before (green) and after (blue) CNQX topical application ($n = 3$). Med: median, IQR: interquartile range. Wilcoxon signed-rank test. (**d**) Table summarizing the behavioral outcome of different combinations of CNQX application and optogenetic stimulation sites. Data are shown as mean \pm s.e.m.,

3.3.7. LFA and RFA are two independent cortical modules

Connectivity analysis suggests that the three identified functional modules activate distinct cortical regions during evoked movement execution. Moreover, the excitatory synaptic block experiments confirmed that GRASP RFA and TAP are represented by two independent modules in the motor cortex. In order to further study the relationship between LFA and RFA we stimulated LFA during RFA pharmacological block (fig3.24a). In this case, there was no significant difference in activated area dimension (Activated area_{vehicle} = 0.12 ± 0.01 mm² vs 30° Activated area_{CNQX} = 0.11 ± 0.02 mm²; $p = 0.75$; $n = 3$) and in activation dynamics (data not shown)(fig.3.24b-c). Moreover, the RFA pharmacological block did not modify the pixel rank distribution (GRASP LFA-med_{RFA-vehicle} = 2.0; GRASP LFA-med_{RFA-CNQX} = 2.0; GRASP LFA-IQR_{RFA-vehicle} = 1.0; GRASP LFA-IQ_{RFA-CNQX} = 1.0; $p = 0.0001$; $n = 3$) of the LFA spatiotemporal activation map (fig.3.23d-e). Interestingly, all the preserved cortical connectivity features of the LFA stimulation correlated with the successful execution of the grasping-like movement following LFA stimulation, while the blocked RFA failed to express grasping behaviour (fig3.24f). These results strongly suggest that the LFA expresses the grasping-like movement independently from the RFA connectivity.

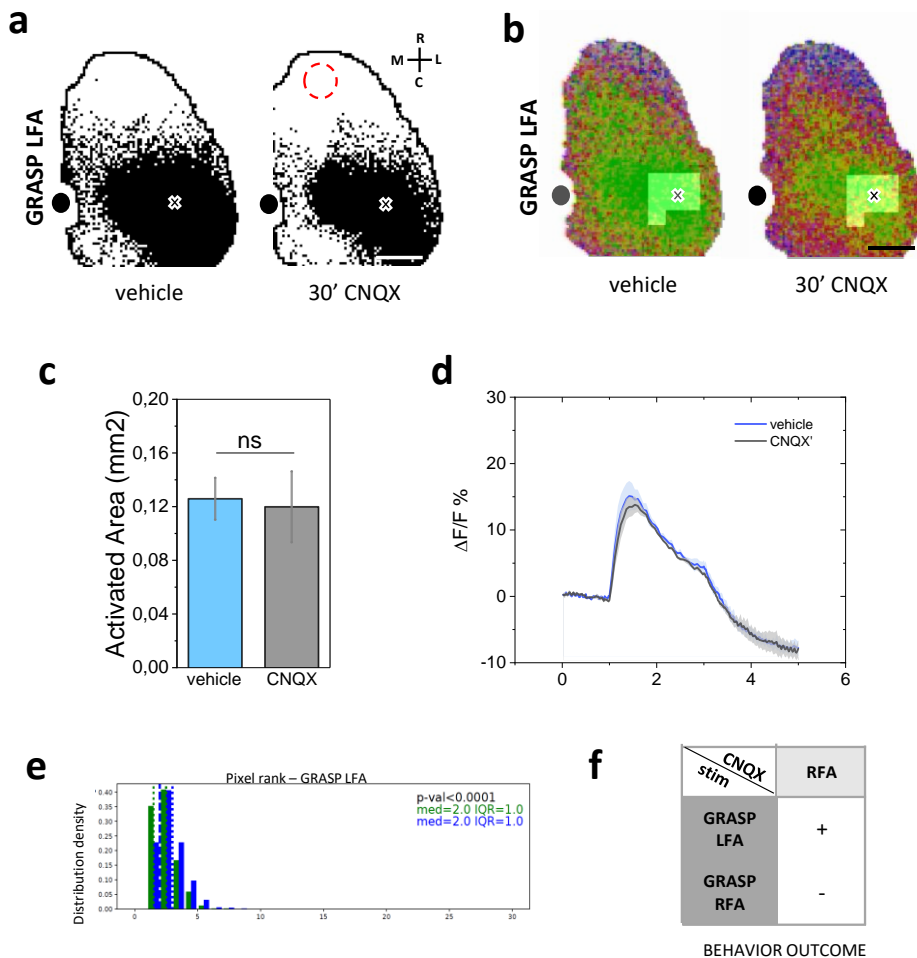


Figure 3.24: LFA grasping expression is independent from RFA connectivity. (a) Representative MIPs showing cortical activation during optogenetic stimulus in LFA during RFA application of vehicle (left) and CNQX (right). (b) Quantification of the activated area extension. (c) Averaged calcium response to optogenetic stimulus in vehicle (blue) and 30' after CNQX application in RFA (grey). (d) Representative maps of the relative spatio-temporal progression of GRASP LFA cortical activation before and 30' after CNQX in RFA. (e) Distribution of pixel rank values of the relative spatio-temporal progression of cortical activation inside the light-based GRASP LFA map before (green) and after (blue) CNQX application in RFA. Med: median, IQR: interquartile range. Wilcoxon signed-rank test. (f) Table summarizing the behavioral outcome. Data are presented as means \pm s.e.m.

4

Discussion

In this thesis, by exploiting a large-scale all-optical approach we showed clear evidence of the functionally independent organization of different modules in the motor cortex, demonstrating their direct contribution to well-defined complex movements. Furthermore, we found that evoking movements by cortical stimulation required an effective local connectivity which involves a high percentage of its related light-based motor map. Importantly, we identified a third functionally independent cortical module, named LFA, suggesting that the lateralization of RFA-related LBMMs may involve two defined cortical modules characterized by the same connections at the corticospinal level.

4.1. jRCaMP1a as the best red-shifted calcium indicator for large-scale cortical studies

First, we performed *in vivo* and *ex vivo* characterization of four red-shifted GECIs (jRCaMP1a, jRCaMP1b, jRGECO1a, jRGECO1b) AAV-transduced in cortical neurons. Red-GECIs transfection stability was examined in awake, head-fixed mice over weeks after the injection. Although jRCaMP1b failed to exhibit significant response compared to the background activity, the other three indicators stably tracked cortical activity dynamics across weeks. We showed only a slight, statistically non-significant, reduction of average $\Delta F/F$ signal along four weeks. Even if mice were acclimated to the environment for a few minutes before each imaging session, the decrease might still be due to changes in animal emotional state over days and weeks (fig3.2). Previous studies have analyzed red-shifted GECIs sensitivity in cultured neurons or in mice using 2P microscopy (Forli et al. 2018; Dana et al. 2016; Akerboom et al. 2013). These studies did not demonstrate transfection stability across time in wide-field configuration. We

showed instead that red-shifted GECIs can be successfully used for long-term mesoscale studies of neuronal activity. jRGECO1a indicator (mApple based) showed the highest response amplitude (fig3.2), in agreement with previous studies in which it was identified as the most sensitive indicator with faster rise and decay kinetics than others (Akerboom, Carreras Calderón et al. 2013, Dana, Mohar et al. 2016). Nevertheless, mApple based-indicators (jRGECO1a and jRGECO1b) are not suited for use in optogenetic experiments involving blue activated opsins, due to their light-dependent photoswitching behaviour when illuminated by blue light (Akerboom, Carreras Calderón et al. 2013, Dana, Mohar et al. 2016).

Mesoscale imaging of different brain regions simultaneously requires a wide coverage of the cortex with fluorescence indicators. Transgenic lines would be one of the best choices to achieve this result. However, only a few indicators are associated with a transgenic line. Consequently, viral transduction is the only option in those cases. Here, we demonstrated that for two out of four indicators (jRCaMP1a and jRGECO1b) the local injection of 500nl of viral construct allowed to transfect a cortical area of approximately 3,7mm *in vivo* (fig3.3b) and 2,6mm *ex vivo* (fig3.4b) on the rostro-caudal plane, which was wide enough to perform imaging on several functional regions, covering entirely the motor cortices. Moreover, jRCaMP1a exhibited both the brightest *in vivo* basal level of fluorescence (fig3.3c) and the best *ex vivo* signal-to-noise ratio (fig3.4c), which is associable with a high *in situ* transduction level. Our result agrees with previous two-photon studies where jRCaMP1a was identified as the brightest indicator in the calcium-bound state (Dana, Mohar et al. 2016,. Taken together all these results allowed us to identify jRCaMP1a as the most suitable indicator for mesoscale studies of *in vivo* cortical activity, especially if imaging is associated with optogenetic stimulation.

Since jRCaMP1a transfection allowed the direct visualization of multiple cortical regions, we tracked the spatiotemporal features of the calcium transients across several functional areas over one hemisphere. We took advantage of a goal-

directed motor task involving the retraction of the contralateral forelimb, to evaluate the jRCaMP1a sensitiveness under different behavioral states. The cortical areas analyzed were: (i) M1. The primary motor cortex is associated with movement directionality, direct muscle control, pattern generation and high-level coordinated transformations during movement generation and execution (Papale and Hooks 2018; Omrani et al. 2017; Shenoy K. V. et al. 2013; Graziano M.S.A. et al. 2002); (ii) M2. The secondary motor cortex is the main drive for goal-directed movement and plays a fundamental role in learning and orchestration of complex movements (Makino et al. 2017). It receives sensory afferences and has reciprocal connection with retrosplenial cortex (Barthas and Kwan 2017); (iii) S1FL. Sensory feedbacks from S1FL to M1 are considered critical in driving learned movements (Petrof et al. 2015; Mathis et al. 2017); (iv) RS is involved in motor control and sensorimotor integration too (Makino et al. 2017; Vann et al. 2009); (v) S1BF is principally involved in whisker-dependent behaviors, thus functional activity in this region should not be primarily involved in forelimb pulling movements (Petersen 2007). Results confirm the involvement of the retrosplenial and sensorimotor regions in movement control, in line with previously studies (Mathis et al. 2017; Omrani et al. 2016). The correlation matrices showed that S1BF has the lowest correlation degree with the other functional areas during active forelimb retraction (fig3.6b). We also revealed a global increase in the correlation index values during the task compared to the resting state for each ROIs pair. Interestingly, our results demonstrated that jRCaMP1a can be successfully applied to study the cortical dynamics in several functional areas simultaneously, enabling the differentiation across cortical regions in the response evoked by a motor-task (fig3.6b). In the final phase of this study, we performed a preliminar correlation of the neuronal activity in M1 with the force applied during the active retraction phase of the motor task. Past studies showed that the activity of corticomotoneuronal cells increased linearly with the modulation of the force level (Cheney and Fetz 1980). According to these studies, we observed a strong linear correlation of M1 neuronal dynamics and the force applied by the mouse (fig3.6c).

Since the viral transfection labels neurons throughout the entire cortex and given that wide-field microscopy cannot provide any optical sectioning, the contribution of each layer to the cortical activity detected is hardly quantifiable. Nevertheless, the highest contribution probably comes from superficial layers of the cortex, since photons originating from deep layers are likely to be scattered away by the tissue before reaching the detector.

In conclusion, we demonstrated that jRCaMP1a transfection with AAV9 is wide, covering a large portion of one hemisphere and shows a high signal to noise ratio that allows simultaneous recording of resting state and motor-evoked cortical activity over several functional areas. Due to the minimized crosstalk of red-shifted GECIs (m-Ruby based) with blue opsins, these findings open a new avenue for the longitudinal imaging of optogenetically manipulated neuronal circuits over large portions of the cortex.

4.2. All-optical crosstalk-free manipulation and readout of cortical dynamics

We developed a one-photon all-optical strategy for detecting large-scale stimulated cortical dynamics *in vivo* by combining simultaneous light-sensitive opsin excitation (ChR2) and red-shifted GECI imaging (jRCaMP1a). To this aim, we first validated our strategy and achieved a widespread and stable transduction of both optogenetic actuator and fluorescence reporter over one hemisphere by exploiting a double injection of two AAV viruses. Consistent with our previous study (Montagni et al., 2018), we demonstrated a stable expression of both ChR2 and jRCaMP1a over the motor cortices of the right hemisphere along several weeks (fig3.7), which allowed to monitor and manipulate neuronal activity from multiple cortical regions simultaneously and longitudinally *in vivo*. Moreover, we finely quantified the expression profile of synapsin-targeted jRCaMP1a in cortical neurons showing that around 70% of all NeuN labelled cells were jRCaMP1a⁺ (fig3.8). Therefore, high transduction efficiency is achieved using our delivery system. At present, there are very few single-photon all-optical strategies available with a sufficient spectral separation of the actuator from the reporter. Red-shifted GECIs were successfully combined with ChR2 to develop a two-photon all-optical approach (Forli et al. 2018) which showed significantly reduced crosstalk compared to other previously developed systems. For the first time we applied this all-optical approach for mapping large-scale cortical activity patterns at the mesoscale level. In our one-photon approach, we confirmed the low crosstalk between indicator and actuator. Indeed, although voltage-clamp electrophysiological data showed subthreshold depolarization of ChR2-expressing cells (Soor et al. 2019), according with previous studies (Forli et al. 2018) we did not detect relevant neurophysiological alteration caused by imaging cross-

activation (fig3.9). The absence of blue light-evoked activity in jRCaMP1a⁺/ChR2⁻ expressing cells *in vivo* (fig3.10) confirmed the absence of a crosstalk between the actuator and the fluorescence reporter.

In conclusion, the combination of ChR2 and jRCaMP1a with wide-field fluorescence microscopy provides a stable and crosstalk-free one-photon all-optical system for simultaneous manipulation and readout of the same neuronal circuit. This approach provides a new perspective to casually investigate the cortical activity patterns that drive light-evoked complex behaviours as described in the next chapter.

4.3. Cortical modules are not functionally organized in a hierarchical premotor-motor organization

One of the main conclusions of the work presented here, resulting from our novel combination of optical techniques, is the finding and characterization of a novel motor area. The first step towards this result was the application of the mesoscale all-optical approach developed in the past chapters to causally investigate the neuronal activity patterns in RFA and CFA driving two optogenetically-evoked complex movements in awake head-fixed mice. Indeed, previous studies showed that two segregated classes of forelimb movements can be evoked by stimulating different cortical sites in mice expressing the optogenetic actuator ChR2 in the motor cortex: RFA stimulation induces forepaw-to-mouth movements (GRASP), while CFA stimulation evoke locomotion-like movements (TAP) (Ayling et al. 2009; Hira et al. 2009; Hira et al. 2015). The present study is the first that evaluates cortical activation patterns elicited by optogenetic stimulation and associates them with the complex movements described above, evidencing a new grasping representation area: the Lateral Forelimb Area (LFA).

We initially identified a mouse-specific minimum laser power required to elicit a clear GRASP or TAP, observing that the maximum intensity of the evoked-calcium response increased with the stimulus intensity (fig3.10c; fig3.11). We showed that the behavioural effect of cortical stimulation and the intensity of the evoked-calcium response are linked to the laser power: there was a mouse-specific minimum laser power required to elicit a clear GRASP or TAP (fig3.11). However, the individual variability observed in the minimum laser power required to evoke the forelimb movement is not mirrored by variability in the induced cortical activation, which is instead stereotyped and reproducible across mice (fig3.11).

These results suggest a cortical activation threshold linked to movement execution independent from the absolute stimulation intensity, which could be instead ascribed to biological and ChR2 expression variability (fig3.12b). Subsequently, we defined the cortical representation of the light-based motor maps related to GRASP and TAP movements (fig3.12c). As expected, our GRASP and TAP LBMMs covered the corresponding motor functional areas, RFA and CFA respectively. Nevertheless, we noticed that the RFA was smaller than the LBMM we identified as GRASP evoking area (Tennant et al. 2011). However, our results are in line with previous studies (Harrison, Ayling, and Murphy 2012; Hira et al. 2015) in which the LBMMs are contiguous and equal in extension (fig3.14). Interestingly, the lateral portion of the GRASP light-based motor map we found matches the one shown by Harrison and colleagues (Harrison, Ayling et al. 2012) for evoking abduction movements.

Thanks to our all-optical approach, it was possible to map large-scale cortical activity patterns associated with the optogenetically-evoked complex movements, showing an intriguing relationship between the spatiotemporal patterns of neuronal activity and the stimulation site. Indeed, when cortical stimulation did not lead to complex movements there wasn't a clear spatiotemporal direction of large-scale cortical activity (fig3.13b), which was instead evident during GRASP or TAP execution (fig3.13a). Moreover, most of the time the non-specific activity patterns avoided both LBMMs previously identified. Subtracting this type of activity to that recorded during LBMMs stimulation (fig3.13c), we revealed a strong cortical activity segregation of GRASP and TAP, which covered a large part of their associated LBMMs

The evidence reviewed above indicates the presence of functionally segregated modules within the motor cortex. The motor cortex subdivision in distinct functional modules were already suggested by Hira and colleagues based on light-based motor mapping of different movements (Hira et al. 2015). However, to the best of our knowledge, the present study is the first to investigate cortical calcium dynamics underlying LBMMs formation, helping to elucidate the functional

segregation of the motor cortex. Interestingly, past VSD imaging studies suggested that ChR2 and sensory stimulation elicited similar patterns of cortical response, even if ChR2-evoked responses tended to be more diffuse than that sensory-evoked ones (Lim et al. 2012b). Further studies are therefore necessary to understand the differences between the cortical areas activated during an optogenetically-evoked and a voluntary movement.

Although there is clear evidence that GRASP and TAP movements tend to be elicited in two well defined and segregated functional areas of the motor cortex, we identified a smaller GRASP-evoking lateral cortical region (fig3.15). We named it the lateral forelimb area (LFA). Interestingly, the calcium dynamics recruited during LFA stimulation does not involve the RFA and vice versa (fig3.15), showing instead a strong spatial segregation and a high percentage of overlap with the associated LBMM (fig3.16). Furthermore, average calcium transient properties evoked in GRASP LFA mirrored those evoked in GRASP RFA or TAP (fig3.17). For GRASP RFA and GRASP LFA movements, the trajectory of the left-forelimb from its starting position was similar (fig3.19a), achieving the same distance in the medial-lateral plane and the same elevation (fig3.19; fig3.20). Furthermore, the entire stimulus train is required for the forelimb to reach its final position during GRASP RFA and GRASP LFA (fig3.19), which also showed a faster onset than TAP (fig3.20). The TAP was instead characterized by rhythmic repetitions of an oscillatory movement more spatially localized and lower in elevation than the two GRASP (fig3.19). Interestingly, TAP movements also showed an opposite directionality in the medial-lateral plane compared to GRASP in the same animal even if the average speed is the same for all the complex movements analyzed (fig3.20). It should be noted that in our study reaching the final position of the forelimb required the whole stimulus train (2 s) for GRASP movements (fig3.19) while previous studies demonstrated that ~ 300 ms were already sufficient (Harrison, Ayling et al. 2012, Hira, Terada et al. 2015).

This apparent inconsistency may be attributed both to the different stimulation frequencies applied and to the use of Chr2 transgenic lines instead of locally injected animals. However, the stimulus features do not affect movement trajectory, which reaches elevation similar to previous studies.

We also analyzed the movement dynamics elicited by no-movement-evoking cortical sites. As expected, their stimulation showed absence of complex movement patterns (fig3.20). This result, in addition to absence of complex cortico-cortical connectivity (fig3.13) and a drastically reduced spread of activation (fig3.21), allow us to associate these cortical activity patterns to forelimbs-unrelated behaviours, such as whiskers or tongue movements or no movement at all. Consequently, we concluded that subtracting this type of activity to that recorded during LBMMs stimulation represented an effective way to reveal the cortical activity strictly associated with the forelimb movement.

In conclusion, the present study firstly supports the hypothesis of independent cortical modules evoking defined complex movements in accordance with previous studies (Harrison, Ayling et al. 2012, Hira, Terada et al. 2015). Secondly, our results support the idea that the LFA is not only a lateral extension of the RFA but represents a distinct GRASP module. Indeed, contrary to what showed for large-scale cortical dynamics, there are no differences in the GRASP RFA or GRASP LFA evoked-performance at behavioural level.

Therefore, to directly test the engagement of specific functional motor regions to different movement executions we also explored the spatial and temporal organization of evoked cortical activity patterns, revealing that each complex movement were linked to individual spatiotemporal patterns of propagation (fig3.21). Our results fit well with previous studies, indeed, the output layer of the motor cortex has independent descending corticospinal projections, which originate from a subtype of pyramidal tract (PT) neurons, named corticospinal motor neurons (CSNs) (Harris and Shepherd 2015; Baker et al. 2018; Economo et al. 2018). CNSs were found in RFA, CFA and in a small circumscribed cluster in a third area in the secondary somatosensory cortex (Wang et al. 2017; Wise et al.

1979). In the spinal cord, CSN axons from this third area mainly overlap with the RFA-CSNs premotor neurons (Wang, Liu et al. 2017). Other studies reported similar results: M1 and S2, although anatomically and functionally distinct, show CSNs in layer 5B whose axons partially converge in the spinal cord (Suter and Shepherd 2015). Moreover, a lateralization of the grasping light-based motor maps was already shown (Harrison, Ayling, and Murphy 2012), but the strong segregation of the neuronal activity linked to the lateral portion of these maps was unexpected and reinforces our hypothesis of a distinct module. However, it should be noticed that due to the lack of optical sectioning in our large-scale one-photon all-optical system, it is difficult to know either 1) how deep in the tissue blue light used for optogenetic stimulation can penetrate and 2) the source of the fluorescence signal (likely a convolution of the signals coming from dendrites from layer 5 pyramidal neurons and layer 2/3 somas and neurites). Further studies will be required to clarify these points and to understand in depth the behaviorally relevant activation pathways.

Finally, to determine whether the cortical modules we found were hierarchically organized, we performed a module-specific pharmacological inhibition of the excitatory synaptic transmission. Interestingly, by blocking the GRASP RFA module it was no longer possible to evoke the related movement (fig3.22) but the locomotion-like movement (TAP) was preserved and vice versa (fig3.23). Our results are in line with previous studies which support the idea of two functionally and anatomically independent modules (Hira et al. 2015; Harrison, Ayling, et al 2012). In addition, taking advantage of our all-optical system we also investigated how pharmacological inhibition affects large-scale evoked-cortical activity dynamics, showing a significant reduction of the activated area coupled to a slower and more disorganized patterns of local propagation. Consequently, our study suggests that a site-specific activation is not sufficient for correct movement execution but rather a complex local interaction within the movement-specific module is required.

We also demonstrated the reciprocal interactions and the hierarchical roles of GRASP RFA and GRASP LFA modules by pharmacologically blocking the GRASP RFA module and stimulating the GRASP LFA. Surprisingly, the activated LFA area did not show changes in its dimension after pharmacological inhibition and there were no perturbations in the local propagation pattern. Interestingly, all the preserved cortical connectivity features of the LFA stimulation correlated with the successful execution of the grasping-like movement following LFA stimulation while, as we showed before, the block of RFA failed to express grasping behaviour.

5

References

- Akerboom, J., N. Carreras Calderón, L. Tian, S. Wabnig, M. Prigge, J. Tolö, A. Gordus, M. B. Orger, K. E. Severi, J. J. Macklin, R. Patel, S. R. Pulver, T. J. Wardill, E. Fischer, C. Schüler, T. Chen, K. S. Sarkisyan, J. S. Marvin, C. I. Bargmann, D. S. Kim, S. Kügler, L. Lagnado, P. Hegemann, A. Gottschalk, E. R. Schreiter, and L. L. Looger. 2013. 'Genetically encoded calcium indicators for multi-color neural activity imaging and combination with optogenetics', *Frontiers in Molecular Neuroscience*, 6.
- Allegra Mascaro, A. L., E. Conti, S. Lai, A. P. Di Giovanna, C. Spalletti, C. Alia, A. Panarese, A. Scaglione, L. Sacconi, S. Micera, M. Caleo, and F. S. Pavone. 2019. 'Combined Rehabilitation Promotes the Recovery of Structural and Functional Features of Healthy Neuronal Networks after Stroke', *Cell Rep*, 28: 3474-85 e6.
- Ayling, O. G., T. C. Harrison, J. D. Boyd, A. Goroshkov, and T. H. Murphy. 2009. 'Automated light-based mapping of motor cortex by photoactivation of channelrhodopsin-2 transgenic mice', *Nat Methods*, 6: 219-24.
- Badea, T. C., H. Dana, O. Novak, M. Guardado-Montesino, J. W. Franssen, A. Hu, B. G. Borghuis, C. Guo, D. S. Kim, and K. Svoboda. 2018. 'Thy1 transgenic mice expressing the red fluorescent calcium indicator jRGECO1a for neuronal population imaging in vivo', *Plos One*, 13.
- Baker, A., B. Kalmbach, M. Morishima, J. Kim, A. Juavinett, N. Li, and N. Dembrow. 2018. 'Specialized Subpopulations of Deep-Layer Pyramidal Neurons in the Neocortex: Bridging Cellular Properties to Functional Consequences', *J Neurosci*, 38: 5441-55.
- Baker, B. J., E. K. Kosmidis, D. Vucinic, C. X. Falk, L. B. Cohen, M. Djuricic, and D. Zecevic. 2005. 'Imaging Brain Activity With Voltage- and Calcium-Sensitive Dyes', *Cellular and Molecular Neurobiology*, 25: 245-82.
- Barthas, Florent, and Alex C. Kwan. 2017. 'Secondary Motor Cortex: Where Sensory Meets Motor in the Rodent Frontal Cortex', *Trends in Neurosciences*, 40: 181-93.
- Bauer, A. Q, A. W Kraft, G. A Baxter, P. W Wright, M. D Reisman, A. R Bice, J. J Park, M. R Bruchas, A. Z Snyder, J. Lee, and J. P. Culver. 2017. 'Effective Connectivity Measured Using Optogenetically Evoked Hemodynamic Signals Exhibits Topography Distinct from Resting State Functional Connectivity in the Mouse', *Cerebral Cortex*, 28: 370-86.

- Berndt, A., P. Schoenenberger, J. Mattis, K. M. Tye, K. Deisseroth, P. Hegemann, and T. G. Oertner. 2011. 'High-efficiency channelrhodopsins for fast neuronal stimulation at low light levels', *Proc Natl Acad Sci U S A*, 108: 7595-600.
- Billinton, N., and A. W. Knight. 2001. 'Seeing the Wood through the Trees: A Review of Techniques for Distinguishing Green Fluorescent Protein from Endogenous Autofluorescence', *Analytical Biochemistry*, 291: 175-97.
- Bin, H., Y. Lin, C. Wilke, and Y. Han. 2011. 'Electrophysiological Imaging of Brain Activity and Connectivity—Challenges and Opportunities', *IEEE Transactions on Biomedical Engineering*, 58: 1918-31.
- Bonazzi, R. Viaro, E. Lodi, R. Canto, C. Bonifazzi, and G. Franchi. 2013. 'Complex Movement Topography and Extrinsic Space Representation in the Rat Forelimb Motor Cortex as Defined by Long-Duration Intracortical Microstimulation', *Journal of Neuroscience*, 33: 2097-107.
- Boychuk, J. A., D. L. Adkins, and J. A. Kleim. 2011. 'Distributed versus focal cortical stimulation to enhance motor function and motor map plasticity in a rodent model of ischemia', *Neurorehabil Neural Repair*, 25: 88-97.
- Brecht, M. 2011. 'Movement, confusion, and orienting in frontal cortices', *Neuron*, 72: 193-6.
- Brock, A. A., R. M. Friedman, R. H. Fan, and A. W. Roe. 2013. 'Optical imaging of cortical networks via intracortical microstimulation', *J Neurophysiol*, 110: 2670-8.
- Brown, A. R., and G. C. Teskey. 2014. 'Motor cortex is functionally organized as a set of spatially distinct representations for complex movements', *J Neurosci*, 34: 13574-85.
- Burns, S.P., D. Xing, and R.M. Shapley. 2010. 'Comparisons of the Dynamics of Local Field Potential and Multiunit Activity Signals in Macaque Visual Cortex', *The Journal of Neuroscience*, 30: 13739.
- Cheney, P. D., and E. E. Fetz. 1980. 'Functional classes of primate corticomotoneuronal cells and their relation to active force', *J Neurophysiol*, 44: 773-91.
- Conti, E., A. L. Allegra Mascaro, and F. S. Pavone. 2019. 'Large Scale Double-Path Illumination System with Split Field of View for the All-Optical Study of Inter-and Intra-Hemispheric Functional Connectivity on Mice', *Methods Protoc*, 2.

- Cramer, J. V., B. Gesierich, S. Roth, M. Dichgans, M. During, and A. Liesz. 2019. 'In vivo widefield calcium imaging of the mouse cortex for analysis of network connectivity in health and brain disease', *Neuroimage*, 199: 570-84.
- Dagleish, H. , L. Russell, A. Packer, A. Roth, O. M. Gauld, F. Greenstreet, E. J. Thompson, and M. Häusser. 2020. 'How many neurons are sufficient for perception of cortical activity? '.
- Dana, H., B. Mohar, Y. Sun, S. Narayan, A. Gordus, J. P. Hasseman, G. Tsegaye, G. T. Holt, A. Hu, D. Walpita, R. Patel, J. J. Macklin, C. I. Bargmann, M. B. Ahrens, E. R. Schreiter, V. Jayaraman, L. L. Looger, K. Svoboda, and D. S. Kim. 2016. 'Sensitive red protein calcium indicators for imaging neural activity', *Elife*, 5.
- Dana, H., Y. Sun, B. Mohar, B. K. Hulse, A. M. Kerlin, J. P. Hasseman, G. Tsegaye, A. Tsang, A. Wong, R. Patel, J. J. Macklin, Y. Chen, A. Konnerth, V. Jayaraman, L. L. Looger, E. R. Schreiter, K. Svoboda, and D. S. Kim. 2019. 'High-performance calcium sensors for imaging activity in neuronal populations and microcompartments', *Nature Methods*, 16: 649-57.
- de Kernier, I., A. Ali-Cherif, N. Rongeat, O. Cioni, S. Morales, J. Savatier, S. Monneret, and P. Blandin. 2019. 'Large field-of-view phase and fluorescence mesoscope with microscopic resolution', *J Biomed Opt*, 24: 1-9.
- Deffeyes, J. E., B. Touvykine, S. Quessy, and N. Dancause. 2015. 'Interactions between rostral and caudal cortical motor areas in the rat', *J Neurophysiol*, 113: 3893-904.
- Deo, C., and L. D. Lavis. 2018. 'Synthetic and genetically encoded fluorescent neural activity indicators', *Current Opinion in Neurobiology*, 50: 101-08.
- Donoghue, J. P., and J. N. Sanes. 1988. 'Organization of adult motor cortex representation patterns following neonatal forelimb nerve injury in rats', *The Journal of Neuroscience*, 8: 3221.
- Donoghue, J.P., and S.P. Wise. 1982. 'The motor cortex of the Rat: Cytoarchitecture and Microstimulation Mapping', *The Journal of Comparative Neurology*, 212: 76-88.
- Dunst, S., and P. Tomancak. 2019. 'Imaging Flies by Fluorescence Microscopy: Principles, Technologies, and Applications', *Genetics*, 211: 15-34.

- Ebbesen, C. L., M. N. Insanally, C. D. Kopec, M. Murakami, A. Saiki, and J. C. Erlich. 2018. 'More than Just a "Motor": Recent Surprises from the Frontal Cortex', *J Neurosci*, 38: 9402-13.
- Economo, M. N., S. Viswanathan, B. Tasic, E. Bas, J. Winnubst, V. Menon, L. T. Graybiel, T. N. Nguyen, K. A. Smith, Z. Yao, L. Wang, C. R. Gerfen, J. Chandrashekar, H. Zeng, L. L. Looger, and K. Svoboda. 2018. 'Distinct descending motor cortex pathways and their roles in movement', *Nature*, 563: 79-84.
- Egawa, T., K. Hanaoka, Y. Koide, S. Ujita, N. Takahashi, Y. Ikegaya, N. Matsuki, T. Terai, T. Ueno, T. Komatsu, and T. Nagano. 2011. 'Development of a Far-Red to Near-Infrared Fluorescence Probe for Calcium Ion and its Application to Multicolor Neuronal Imaging', *Journal of the American Chemical Society*, 133: 14157-59.
- Eickelbeck, D., Karapinar R., Herlitze S., and Spoida K. 2018. 'Optogenetic Approaches for Controlling Neuronal Activity and Plasticity.' in, *Handbook of in Vivo Neural Plasticity Techniques*.
- Emiliani, V., A. E. Cohen, K. Deisseroth, and M. Hausser. 2015. 'All-Optical Interrogation of Neural Circuits', *J Neurosci*, 35: 13917-26.
- Forli, A., D. Vecchia, N. Binini, F. Succol, S. Bovetti, C. Moretti, F. Nespoli, M. Mahn, C. A. Baker, M. M. Bolton, O. Yizhar, and T. Fellin. 2018. 'Two-Photon Bidirectional Control and Imaging of Neuronal Excitability with High Spatial Resolution In Vivo', *Cell Rep*, 22: 3087-98.
- Förster, D., M. Dal Maschio, E. Laurell, and H. Baier. 2017. 'An optogenetic toolbox for unbiased discovery of functionally connected cells in neural circuits', *Nature Communications*, 8: 116.
- Foust, K. D., E. Nurre, C. L. Montgomery, A. Hernandez, C. M. Chan, and B. K. Kaspar. 2009. 'Intravascular AAV9 preferentially targets neonatal neurons and adult astrocytes', *Nat Biotechnol*, 27: 59-65.
- Fujiwara, T. K., K. Iwasawa, Z. Kalay, T. A. Tsunoyama, Y. Watanabe, Y. M. Umemura, H. Murakoshi, K. G. Suzuki, Y. L. Nemoto, N. Morone, and A. Kusumi. 2016. 'Confined diffusion of transmembrane proteins and lipids induced by the same actin meshwork lining the plasma membrane', *Mol Biol Cell*, 27: 1101-19.
- Gombash, S.E., C.J. Cowley, J.A. Fitzgerald, J.C.E. Hall, C. Mueller, F.L. Christofi, and K.D. Foust. 2014. 'Intravenous AAV9 efficiently

- transduces myenteric neurons in neonate and juvenile mice', *Frontiers in Molecular Neuroscience*, 7.
- Graziano, M.S.A., Taylor C.S.R., and Moore T. 2002. 'Complex Movements Evoked by Microstimulation of Precentral Cortex', *Neuron*, 34: 841-51.
- Graziano M.S.A. et al. 2002. 'Complex movements evoked by microstimulation of Precentral Cortex', *Neuron*, 34: 10.
- Grinvald, A., R.D. Frostig, E. Lieke, and R. Hildesheim. 1988. 'Optical Imaging of Neuronal Activity', *Physiological Reviews*.
- Gross, C. G. 2007. 'The discovery of motor cortex and its background', *J Hist Neurosci*, 16: 320-31.
- Grossman, N., V. Poher, M. S. Grubb, G. T. Kennedy, K. Nikolic, B. McGovern, R. Berlinguer Palmimi, Z. Gong, E. M. Drakakis, M. A. Neil, M. D. Dawson, J. Burrone, and P. Degenaar. 2010. 'Multi-site optical excitation using ChR2 and micro-LED array', *J Neural Eng*, 7: 16004.
- Guo, J.Z., A. R. Graves, W.W. Guo, J. Zheng, A. Lee, J. Rodríguez-González, N. Li, J.J. Macklin, J.W. Phillips, B.D. Mensh, K. Branson, and A.W. Hantman. 2015. 'Cortex commands the performance of skilled movement', *Elife*, 4.
- Guo, Z. V., A. C. Hart, and S. Ramanathan. 2009. 'Optical interrogation of neural circuits in *Caenorhabditis elegans*', *Nature Methods*, 6: 891-96.
- Guo, Z. V., N. Li, D. Huber, E. Ophir, D. Gutnisky, J. T. Ting, G. Feng, and K. Svoboda. 2014. 'Flow of cortical activity underlying a tactile decision in mice', *Neuron*, 81: 179-94.
- Guru, A., R. J. Post, Y. Y. Ho, and M. R. Warden. 2015. 'Making Sense of Optogenetics', *Int J Neuropsychopharmacol*, 18: pyv079.
- Hagner, M. 2012. 'The electrical excitability of the brain: toward the emergence of an experiment', *J Hist Neurosci*, 21: 237-49.
- Harris, K. D., and G. M. Shepherd. 2015. 'The neocortical circuit: themes and variations', *Nat Neurosci*, 18: 170-81.
- Harrison, T. C., O. G. Ayling, and T. H. Murphy. 2012. 'Distinct cortical circuit mechanisms for complex forelimb movement and motor map topography', *Neuron*, 74: 397-409.
- Hausser, M. 2014. 'Optogenetics: the age of light', *Nat Methods*, 11: 1012-4.
- Helmchen, F., and W. Denk. 2005. 'Deep tissue two-photon microscopy', *Nat Methods*, 2: 932-40.

- Hight, A.E., E. D. Kozin, K. Darrow, A. Lehmann, E. Boyden, M. C. Brown, and D. J. Lee. 2015. 'Superior temporal resolution of Chronos versus channelrhodopsin-2 in an optogenetic model of the auditory brainstem implant', *Hearing Research*, 322: 235-41.
- Hira, R., N. Honkura, J. Noguchi, Y. Maruyama, G. J. Augustine, H. Kasai, and M. Matsuzaki. 2009. 'Transcranial optogenetic stimulation for functional mapping of the motor cortex', *Journal of Neuroscience Methods*, 179: 258-63.
- Hira, R., F. Ohkubo, K. Ozawa, Y. Isomura, K. Kitamura, M. Kano, H. Kasai, and M. Matsuzaki. 2013. 'Spatiotemporal dynamics of functional clusters of neurons in the mouse motor cortex during a voluntary movement', *J Neurosci*, 33: 1377-90.
- Hira, R., F. Ohkubo, Y. R. Tanaka, Y. Masamizu, G. J. Augustine, H. Kasai, and M. Matsuzaki. 2013. 'In vivo optogenetic tracing of functional corticocortical connections between motor forelimb areas', *Front Neural Circuits*, 7: 55.
- Hira, R., S. Terada, M. Kondo, and M. Matsuzaki. 2015. 'Distinct Functional Modules for Discrete and Rhythmic Forelimb Movements in the Mouse Motor Cortex', *J Neurosci*, 35: 13311-22.
- Hires, S. A., L. Tian, and L. L. Looger. 2008. 'Reporting neural activity with genetically encoded calcium indicators', *Brain Cell Biol*, 36: 69-86.
- Homma, R., B. J. Baker, L. Jin, O. Garaschuk, A. Konnerth, L. B. Cohen, and D. Zeccevic. 2009. 'Wide-field and two-photon imaging of brain activity with voltage- and calcium-sensitive dyes', *Philos Trans R Soc Lond B Biol Sci*, 364: 2453-67.
- Hosp, J. A., K. Molina-Luna, B. Hertler, C. O. Atiemo, A. Stett, and A. R. Luft. 2008. 'Thin-film epidural microelectrode arrays for somatosensory and motor cortex mapping in rat', *J Neurosci Methods*, 172: 255-62.
- Imanishi, Y., K. H. Lodowski, and Y. Koutalos. 2007. 'Two-photon microscopy: shedding light on the chemistry of vision', *Biochemistry*, 46: 9674-84.
- Inoue, M., A. Takeuchi, S. Horigane, M. Ohkura, K. Gengyo-Ando, H. Fujii, S. Kamijo, S. Takemoto-Kimura, M. Kano, J. Nakai, K. Kitamura, and H. Bito. 2015. 'Rational design of a high-affinity, fast, red calcium indicator R-CaMP2', *Nature Methods*, 12: 64-70.
- Jiao, Z. F., C. F. Shang, Y. F. Wang, Z. Yang, C. Yang, F. N. Li, J. Z. Xie, J. W. Pan, L. Fu, and J. L. Du. 2018. 'All-optical imaging and

- manipulation of whole-brain neuronal activities in behaving larval zebrafish', *Biomed Opt Express*, 9: 6154-69.
- Kalanithi, P. S. A., and D. Purger. 2017. 'Optogenetics.' in, *Innovative Neuromodulation*.
- Karl, J.M., and I.Q. Whishaw. 2013. 'Different Evolutionary Origins for the Reach and the Grasp: An Explanation for Dual Visuomotor Channels in Primate Parietofrontal Cortex', *Frontiers in Neurology*, 4.
- Kerr, J. N., and W. Denk. 2008. 'Imaging in vivo: watching the brain in action', *Nat Rev Neurosci*, 9: 195-205.
- Kim, C. K., A. Adhikari, and K. Deisseroth. 2017. 'Integration of optogenetics with complementary methodologies in systems neuroscience', *Nat Rev Neurosci*, 18: 222-35.
- Kim, D., T. Q. Duong, and S. Kim. 2000. 'High-resolution mapping of iso-orientation columns by fMRI', *Nature Neuroscience*, 3: 164-69.
- Kimura, R., A. Saiki, Y. Fujiwara-Tsukamoto, Y. Sakai, and Y. Isomura. 2017. 'Large-scale analysis reveals populational contributions of cortical spike rate and synchrony to behavioural functions', *J Physiol*, 595: 385-413.
- Klapoetke, N.C., Y. Murata, S.S. Kim, S.R. Pulver, A. Birdsey-Benson, Y.K. Cho, T.K. Morimoto, A.S. Chuong, E.J. Carpenter, Z. Tian, J. Wang, Y. Xie, Z. Yan, Y. Zhang, B.Y. Chow, B. Surek, M. Melkonian, V. Jayaraman, M. Constantine-Paton, G.K. Wong, and E.S. Boyden. 2014. 'Independent optical excitation of distinct neural populations', *Nature Methods*, 11: 338-46.
- Kunori, N., and I. Takashima. 2016. 'High-order motor cortex in rats receives somatosensory inputs from the primary motor cortex via cortico-cortical pathways', *Eur J Neurosci*, 44: 2925-34.
- Lee, S., C. Tsou, P. Huang, P. Cheng, C. Liao, Z. Liao, H. Lee, C. Lin, and C. Hsieh. 2019. '22.7 A Programmable Wireless EEG Monitoring SoC with Open/Closed-Loop Optogenetic and Electrical Stimulation for Epilepsy Control', *ISSCC*: 372-74.
- Li, Jing, and Thomas M. Daly. 2002. 'Adeno-associated virus-mediated gene transfer to the neonatal brain', *Methods*, 28: 203-07.
- Li, N., S. Chen, Z. V. Guo, H. Chen, Y. Huo, H. K. Inagaki, G. Chen, C. Davis, D. Hansel, C. Guo, and K. Svoboda. 2019. 'Spatiotemporal constraints on optogenetic inactivation in cortical circuits', *Elife*, 8.

- Liang, R., G.J. Broussard, and L. Tian. 2015. 'Imaging Chemical Neurotransmission with Genetically Encoded Fluorescent Sensors', *ACS Chemical Neuroscience*, 6: 84-93.
- Lim, H. Diana, J. Ledue, M. H. Mohajerani, M. P. Vanni, and T. H. Murphy. 2013. 'Optogenetic approaches for functional mouse brain mapping', *Frontiers in Neuroscience*, 7.
- Lim, D. H., J. M. LeDue, M. H. Mohajerani, and T. H. Murphy. 2014. 'Optogenetic mapping after stroke reveals network-wide scaling of functional connections and heterogeneous recovery of the peri-infarct', *J Neurosci*, 34: 16455-66.
- Lim, D. H., M. H. Mohajerani, J. Ledue, J. Boyd, S. Chen, and T. H. Murphy. 2012a. 'In vivo Large-Scale Cortical Mapping Using Channelrhodopsin-2 Stimulation in Transgenic Mice Reveals Asymmetric and Reciprocal Relationships between Cortical Areas', *Front Neural Circuits*, 6: 11.
- Lim, D., M. Mohajerani, J. LeDue, J. Boyd, S. Chen, and T. Murphy. 2012b. 'In vivo Large-Scale Cortical Mapping Using Channelrhodopsin-2 Stimulation in Transgenic Mice Reveals Asymmetric and Reciprocal Relationships between Cortical Areas', *Frontiers in Neural Circuits*, 6.
- Lin, J. Y. 2011. 'A user's guide to channelrhodopsin variants: features, limitations and future developments', *Exp Physiol*, 96: 19-25.
- Lin, M. Z., and M. J. Schnitzer. 2016. 'Genetically encoded indicators of neuronal activity', *Nat Neurosci*, 19: 1142-53.
- Liu, Y. Z., C. Renteria, C. D. Courtney, B. Ibrahim, S. You, E. J. Chaney, R. Barkalifa, R. R. Iyer, M. Zurauskas, H. Tu, D. A. Llano, C. A. Christian-Hinman, and S. A. Boppart. 2020. 'Simultaneous two-photon activation and imaging of neural activity based on spectral-temporal modulation of supercontinuum light', *Neurophotonics*, 7: 045007.
- Ma, Y., M. A. Shaik, S. H. Kim, M. G. Kozberg, D. N. Thibodeaux, H. T. Zhao, H. Yu, and E. M. Hillman. 2016. 'Wide-field optical mapping of neural activity and brain haemodynamics: considerations and novel approaches', *Philos Trans R Soc Lond B Biol Sci*, 371.
- Makino, H., C. Ren, H. Liu, A.N. Kim, N. Kondapaneni, X. Liu, D. Kuzum, and T. Komiyama. 2017. 'Transformation of Cortex-wide Emergent Properties during Motor Learning', *Neuron*, 94: 880-90.e8.

- Mancuso, J. J., J. Kim, S. Lee, S. Tsuda, N. B. Chow, and G. J. Augustine. 2011. 'Optogenetic probing of functional brain circuitry', *Exp Physiol*, 96: 26-33.
- Mansoori, B. K., L. Jean-Charles, B. Touvykine, A. Liu, S. Quessy, and N. Dancause. 2014. 'Acute inactivation of the contralesional hemisphere for longer durations improves recovery after cortical injury', *Exp Neurol*, 254: 18-28.
- Mardia. 1999. 'Tests of uniformity and tests of goodness-of-fit. Directional Statistics.', *New York: Wiley*: 93-118.
- Mathis, M.W., A. Mathis, and N. Uchida. 2017. 'Somatosensory Cortex Plays an Essential Role in Forelimb Motor Adaptation in Mice', *Neuron*, 93: 1493-503.e6.
- Mehring, C., J. Rickert, E. Vaadia, S.C. de Oliveira, A. Aertsen, and S. Rotter. 2003. 'Inference of hand movements from local field potentials in monkey motor cortex', *Nature Neuroscience*, 6: 1253-54.
- Miyashita, T., Y. R. Shao, J. Chung, O. Pourzia, and D. E. Feldman. 2013. 'Long-term channelrhodopsin-2 (ChR2) expression can induce abnormal axonal morphology and targeting in cerebral cortex', *Front Neural Circuits*, 7: 8.
- Mohajerani, M. H., D. A. McVea, M. Fingas, and T. H. Murphy. 2010. 'Mirrored Bilateral Slow-Wave Cortical Activity within Local Circuits Revealed by Fast Bihemispheric Voltage-Sensitive Dye Imaging in Anesthetized and Awake Mice', *The Journal of Neuroscience*, 30: 3745.
- Montagni, E., F. Resta, E. Conti, A. Scaglione, M. Pasquini, S. Micera, A.L.A. Mascaro, and F.S. Pavone. 2019. 'Wide-field imaging of cortical neuronal activity with red-shifted functional indicators during motor task execution', *Journal of Physics D: Applied Physics*, 52.
- Montagni, E., F. Resta, A.L.A. Mascaro, and F.S. Pavone. 2019. 'Optogenetics in Brain Research: From a Strategy to Investigate Physiological Function to a Therapeutic Tool', *Photonics*, 6.
- Morandell, K., and D. Huber. 2017. 'The role of forelimb motor cortex areas in goal directed action in mice', *Sci Rep*, 7: 15759.
- Nagai, Takeharu, Kazuki Horikawa, Kenta Saito, and Tomoki Matsuda. 2014. 'Genetically encoded Ca²⁺ indicators; expanded affinity range, color hue and compatibility with optogenetics', *Frontiers in Molecular Neuroscience*, 7.

- Nagel, G., M. Brauner, J. F. Liewald, N. Adeishvili, E. Bamberg, and A. Gottschalk. 2005. 'Light activation of channelrhodopsin-2 in excitable cells of *Caenorhabditis elegans* triggers rapid behavioral responses', *Curr Biol*, 15: 2279-84.
- Nagel, G., T. Szellas, W. Huhn, S. Kateriya, N. Adeishvili, P. Berthold, D. Ollig, P. Hegemann, and E. Bamberg. 2003. 'Channelrhodopsin-2, a directly light-gated cation-selective membrane channel', *Proceedings of the National Academy of Sciences*, 100: 13940.
- Nakamichi, Y., K. Okubo, T. Sato, M. Hashimoto, and M. Tanifuji. 2019. 'Optical intrinsic signal imaging with optogenetics reveals functional cortico-cortical connectivity at the columnar level in living macaques', *Scientific Reports*, 9: 6466.
- Nwaneshiudu, A., C. Kuschal, F. H. Sakamoto, R. R. Anderson, K. Schwarzenberger, and R. C. Young. 2012. 'Introduction to confocal microscopy', *J Invest Dermatol*, 132: e3.
- Oda, K., J. Vierock, S. Oishi, S. Rodriguez-Rozada, R. Taniguchi, K. Yamashita, J. S. Wiegert, T. Nishizawa, P. Hegemann, and O. Nureki. 2018. 'Crystal structure of the red light-activated channelrhodopsin Chrimson', *Nature Communications*, 9: 3949.
- Oh, J., C. Lee, and B. K. Kaang. 2019. 'Imaging and analysis of genetically encoded calcium indicators linking neural circuits and behaviors', *Korean J Physiol Pharmacol*, 23: 237-49.
- Oheim, M., E. Beaupaire, E. Chaigneau, J. Mertz, and S. Charpak. 2001. 'Two-photon microscopy in brain tissue: parameters influencing the imaging depth', *Journal of Neuroscience Methods*, 111: 29-37.
- Olofsson, N., I. Lazaridis, K. Meletis, and M. Carlén. 2015. 'Lasers, Optics Enhance Optogenetics Studies'.
- Omrani, M., M. T. Kaufman, N. G. Hatsopoulos, and P. D. Cheney. 2017. 'Perspectives on classical controversies about the motor cortex', *J Neurophysiol*, 118: 1828-48.
- Omrani, M., C. D. Murnaghan, J. A. Pruszynski, and S. H. Scott. 2016. 'Distributed task-specific processing of somatosensory feedback for voluntary motor control', *Elife*, 5: e13141.
- Oron, D., E. Papagiakoumou, F. Anselmi, and V. Emiliani. 2012. 'Two-photon optogenetics', *Prog Brain Res*, 196: 119-43.
- Packer, A. M., B. Roska, and M. Hausser. 2013. 'Targeting neurons and photons for optogenetics', *Nat Neurosci*, 16: 805-15.

- Packer, A.A.X., L.A.X. Russell, H. W. Dalgleish, and M. Häusser. 2015. 'Simultaneous all-optical manipulation and recording of neural circuit activity with cellular resolution in vivo'.
- Papagiakoumou, E. 2013. 'Optical developments for optogenetics', *Biol Cell*, 105: 443-64.
- Papagiakoumou, E., A. Bègue, B. Leshem, O. Schwartz, B.M. Stell, J. Bradley, D. Oron, and V. Emiliani. 2013. 'Functional patterned multiphoton excitation deep inside scattering tissue', *Nature Photonics*, 7: 274-78.
- Papale, A. E., and B. M. Hooks. 2018. 'Circuit Changes in Motor Cortex During Motor Skill Learning', *Neuroscience*, 368: 283-97.
- Paredes, R. M., J. C. Etzler, L. T. Watts, W. Zheng, and J. D. Lechleiter. 2008. 'Chemical calcium indicators', *Methods*, 46: 143-51.
- Park, K. S., J. G. Shin, M. M. Qureshi, E. Chung, and T. J. Eom. 2018. 'Deep brain optical coherence tomography angiography in mice: in vivo, noninvasive imaging of hippocampal formation', *Sci Rep*, 8: 11614.
- Pawley. 2006. 'Fundamental Limits in Confocal Microscopy. In: Pawley J. (eds) Handbook Of Biological Confocal Microscopy.', *Springer, Boston, MA*.
- Paxinos, George, and Keith BJ Franklin. 2019. *Paxinos and Franklin's the mouse brain in stereotaxic coordinates* (Academic press).
- Perez, K. V., and T. Nagai. 2013. 'Genetically encoded Ca(2+) indicators: properties and evaluation', *Biochim Biophys Acta*, 1833: 1787-97.
- Petersen, C. C. 2007. 'The functional organization of the barrel cortex', *Neuron*, 56: 339-55.
- Petrof, I., A. N. Viaene, and S. M. Sherman. 2015. 'Properties of the primary somatosensory cortex projection to the primary motor cortex in the mouse', *J Neurophysiol*, 113: 2400-7.
- Porumb, T., P. Yau, S.T. Harvey, and M. Ikura. 1994. 'A calmodulin-target peptide hybrid molecule with unique calcium-binding properties', *Protein Engineering*, 7.
- Prigge, M., F. Schneider, S. P. Tsunoda, C. Shilyansky, J. Wietek, K. Deisseroth, and P. Hegemann. 2012. 'Color-tuned channelrhodopsins for multiwavelength optogenetics', *J Biol Chem*, 287: 31804-12.
- Raimondo, J. V., L. Kay, T. J. Ellender, and C. J. Akerman. 2012. 'Optogenetic silencing strategies differ in their effects on inhibitory synaptic transmission', *Nat Neurosci*, 15: 1102-4.

- Ramanathan D., Conner J.M., and Tuszynski H.M. 2006. 'A form of motor cortical plasticity that correlates with recovery of function after brain injury', *PNAS*, 103: 11370-75.
- Rao, J., A. Dragulescu-Andrasi, and H. Yao. 2007. 'Fluorescence imaging in vivo: recent advances', *Current Opinion in Biotechnology*, 18: 17-25.
- Richard, O.S., and M. Philippe. 2011. 'Adeno-Associated Virus (Methods and Protocols)'.
Riehle, A., S. Wirtsohn, S. Gruen, and T. Brochier. 2013. 'Mapping the spatio-temporal structure of motor cortical LFP and spiking activities during reach-to-grasp movements', *Frontiers in Neural Circuits*, 7.
- Rossano, A. J., A. K. Chouhan, and G. T. Macleod. 2013. 'Genetically encoded pH-indicators reveal activity-dependent cytosolic acidification of Drosophila motor nerve termini in vivo', *The Journal of Physiology*, 591: 1691-706.
- Saiki, A., R. Kimura, T. Samura, Y. Fujiwara-Tsukamoto, Y. Sakai, and Y. Isomura. 2014. 'Different modulation of common motor information in rat primary and secondary motor cortices', *Plos One*, 9: e98662.
- Scanziani, M., and M. Häusser. 2009. 'Electrophysiology in the age of light', *Nature*, 461: 930-39.
- Scott, B. B., S. Y. Thiberge, C. Guo, D. G. R. Tervo, C. D. Brody, A. Y. Karpova, and D. W. Tank. 2018. 'Imaging Cortical Dynamics in GCaMP Transgenic Rats with a Head-Mounted Widefield Macroscopy', *Neuron*, 100: 1045-58 e5.
- Shaw, Peter J. 2006. 'Comparison of Widefield/Deconvolution and Confocal Microscopy for Three-Dimensional Imaging.' in James B. Pawley (ed.), *Handbook Of Biological Confocal Microscopy* (Springer US: Boston, MA).
- Sheffield, M. E. J., M. D. Adoff, and D. A. Dombeck. 2017. 'Increased Prevalence of Calcium Transients across the Dendritic Arbor during Place Field Formation', *Neuron*, 96: 490-504 e5.
- Shenoy K. V. et al. 2013. 'Cortical control of arm movements: a dynamical systems perspective', *Annu Rev Neurosci*, 36: 337-59.
- Silasi, G., J. D. Boyd, J. Ledue, and T. H. Murphy. 2013. 'Improved methods for chronic light-based motor mapping in mice: automated movement tracking with accelerometers, and chronic

- EEG recording in a bilateral thin-skull preparation', *Front Neural Circuits*, 7: 123.
- Silasi, G., D. Xiao, M. P. Vanni, A. C. Chen, and T. H. Murphy. 2016. 'Intact skull chronic windows for mesoscopic wide-field imaging in awake mice', *J Neurosci Methods*, 267: 141-9.
- Singleton, Anna. 2014. 'The Development of Complex Movement Motor Maps Using Long Duration Intracortical Microstimulation (LD-ICMS) in Rats', *University of Calgary*.
- Soma, S., A. Saiki, J. Yoshida, A. Rios, M. Kawabata, Y. Sakai, and Y. Isomura. 2017. 'Distinct Laterality in Forelimb-Movement Representations of Rat Primary and Secondary Motor Cortical Neurons with Intratelencephalic and Pyramidal Tract Projections', *J Neurosci*, 37: 10904-16.
- Soor, N. S., P. Quicke, C. L. Howe, K. T. Pang, M. A. A. Neil, S. R. Schultz, and A. J. Foust. 2019. 'All-optical crosstalk-free manipulation and readout of Chronos-expressing neurons', *J Phys D Appl Phys*, 52: 104002.
- Spalletti, C., C. Alia, S. Lai, A. Panarese, S. Conti, S. Micera, and M. Caleo. 2017. 'Combining robotic training and inactivation of the healthy hemisphere restores pre-stroke motor patterns in mice', *Elife*, 6: e28662.
- Spalletti, C., S. Lai, M. Mainardi, A. Panarese, A. Ghionzoli, C. Alia, L. Gianfranceschi, C. Chisari, S. Micera, and M. Caleo. 2013. 'A Robotic System for Quantitative Assessment and Poststroke Training of Forelimb Retraction in Mice', *Neurorehabilitation and Neural Repair*, 28: 188-96.
- Steinmetz, N. A., C. Buetfering, J. Lecoq, C. R. Lee, A. J. Peters, E. A. K. Jacobs, P. Coen, D. R. Ollerenshaw, M. T. Valley, S. E. J. de Vries, M. Garrett, J. Zhuang, P. A. Groblewski, S. Manavi, J. Miles, C. White, E. Lee, F. Griffin, J. D. Larkin, K. Roll, S. Cross, T. V. Nguyen, R. Larsen, J. Pendergraft, T. Daigle, B. Tasic, C. L. Thompson, J. Waters, S. Olsen, D. J. Margolis, H. Zeng, M. Hausser, M. Carandini, and K. D. Harris. 2017. 'Aberrant Cortical Activity in Multiple GCaMP6-Expressing Transgenic Mouse Lines', *eneuro*, 4: ENEURO.0207-17.2017.
- Stepanenko, O. V., V.V. Verkhusha, M.I. Kuznetsova, N.V. Uversky, and K.K. Turoverov. 2018. 'Fluorescent proteins as biomarkers and biosensors: throwing color lights on molecular and cellular processes', *Curr Protein Pept Sci.*, 9: 338–69.

- Suter, B. A., and G. M. Shepherd. 2015. 'Reciprocal interareal connections to corticospinal neurons in mouse M1 and S2', *J Neurosci*, 35: 2959-74.
- Suzuki, J., K. Kanemaru, and M. Iino. 2016. 'Genetically Encoded Fluorescent Indicators for Organellar Calcium Imaging', *Biophysical Journal*, 111: 1119-31.
- Svoboda, K., and S. M. Block. 1994. 'Biological Applications of Optical Forces', *Annual Review of Biophysics and Biomolecular Structure*, 23: 247-85.
- Szabo, V., C. Ventalon, V. De Sars, J. Bradley, and V. Emiliani. 2014. 'Spatially Selective Holographic Photoactivation and Functional Fluorescence Imaging in Freely Behaving Mice with a Fiberscope', *Neuron*, 84: 1157-69.
- Tennant, K. A., D. L. Adkins, N. A. Donlan, A. L. Asay, N. Thomas, J. A. Kleim, and T. A. Jones. 2011. 'The organization of the forelimb representation of the C57BL/6 mouse motor cortex as defined by intracortical microstimulation and cytoarchitecture', *Cereb Cortex*, 21: 865-76.
- Torricelli, A., D. Contini, A. Dalla Mora, A. Pifferi, R. Re, L. Zucchelli, M. Caffini, A. Farina, and L. Spinelli. 2014. 'Neurophotonics: non-invasive optical techniques for monitoring brain functions', *Funct Neurol*, 29.
- Tsien, Roger Y. 1998. 'THE GREEN FLUORESCENT PROTEIN', *Annual Review of Biochemistry*, 67: 509-44.
- Turrini, L., C. Fornetto, G. Marchetto, M. C. Müllenbroich, N. Tiso, A. Vettori, F. Resta, A. Masi, G. Mannaioni, F. S. Pavone, and F. Vanzi. 2017. 'Optical mapping of neuronal activity during seizures in zebrafish', *Scientific Reports*, 7: 3025.
- Van der Linden, A., N. Van Camp, P. Ramos-Cabrera, and M. Hoehn. 2007. 'Current status of functional MRI on small animals: application to physiology, pathophysiology, and cognition', *NMR Biomed*, 20: 522-45.
- Vann, S. D., J. P. Aggleton, and E. A. Maguire. 2009. 'What does the retrosplenial cortex do?', *Nature Reviews Neuroscience*, 10: 792-802.
- Vanni, M. P., A. W. Chan, M. Balbi, G. Silasi, and T. H. Murphy. 2017. 'Mesoscale Mapping of Mouse Cortex Reveals Frequency-Dependent Cycling between Distinct Macroscale Functional Modules', *J Neurosci*, 37: 7513-33.

- Vinokurova, D., A. V. Zakharov, J. Lebedeva, G. F. Burkhanova, K. A. Chernova, N. Lotfullina, R. Khazipov, and G. Valeeva. 2018. 'Pharmacodynamics of the Glutamate Receptor Antagonists in the Rat Barrel Cortex', *Frontiers in Pharmacology*, 9.
- Wang, X., Y. Liu, X. Li, Z. Zhang, H. Yang, Y. Zhang, P. R. Williams, N. S. A. Alwahab, K. Kapur, B. Yu, Y. Zhang, M. Chen, H. Ding, C. R. Gerfen, K. H. Wang, and Z. He. 2017. 'Deconstruction of Corticospinal Circuits for Goal-Directed Motor Skills', *Cell*, 171: 440-55 e14.
- Warren, D.L., Q. Guang, T.J. Sferra, R. Clark, R. Chen, and P.R. Johnson. 1999. 'Adeno-Associated Virus-Mediated Gene Transfer to the Brain: Duration and Modulation of Expression ', *Human Gene Therapy*, 10: 201-13.
- Watanabe, H., H. Sano, S. Chiken, K. Kobayashi, Y. Fukata, M. Fukata, H. Mushiake, and A. Nambu. 2020. 'Forelimb movements evoked by optogenetic stimulation of the macaque motor cortex', *Nat Commun*, 11: 3253.
- Weisenburger, S., and A. Vaziri. 2018. 'A Guide to Emerging Technologies for Large-Scale and Whole-Brain Optical Imaging of Neuronal Activity', *Annu Rev Neurosci*, 41: 431-52.
- Wiegert, J. S., M. Mahn, M. Prigge, Y. Printz, and O. Yizhar. 2017. 'Silencing Neurons: Tools, Applications, and Experimental Constraints', *Neuron*, 95: 504-29.
- Wilson, N. R., C. A. Runyan, F. L. Wang, and M. Sur. 2012. 'Division and subtraction by distinct cortical inhibitory networks in vivo', *Nature*, 488: 343-48.
- Wise, S.P., E.A. Murray, and Coulter J.D. 1979. 'Somatotopic organization of corticospinal and corticotrigeminal neurons in the rat', *Neuroscience*, 4: 8.
- Wu, F., E. Stark, P. C. Ku, K. D. Wise, G. Buzsaki, and E. Yoon. 2015. 'Monolithically Integrated muLEDs on Silicon Neural Probes for High-Resolution Optogenetic Studies in Behaving Animals', *Neuron*, 88: 1136-48.
- Yang, Fan, Larry G. Moss, and George N. Phillips. 1996. 'The molecular structure of green fluorescent protein', *Nature Biotechnology*, 14: 1246-51.
- Yang, H. H., and F. St-Pierre. 2016. 'Genetically Encoded Voltage Indicators: Opportunities and Challenges', *Journal of Neuroscience*, 36: 9977-89.

- Yang, M., C. Chang, and L. Chen. 2017. 'Blue light induced reactive oxygen species from flavin mononucleotide and flavin adenine dinucleotide on lethality of HeLa cells', *Journal of Photochemistry and Photobiology B: Biology*, 173: 325-32.
- Yang, W., L. Carrillo-Reid, Y. Bando, D. S. Peterka, and R. Yuste. 2018. 'Simultaneous two-photon imaging and two-photon optogenetics of cortical circuits in three dimensions', *Elife*, 7: e32671.
- Young, N. A., J. Vuong, and G. C. Teskey. 2012. 'Development of motor maps in rats and their modulation by experience', *J Neurophysiol*, 108: 1309-17.
- Zeng, H., and L. Madisen. 2012. 'Mouse transgenic approaches in optogenetics', *Prog Brain Res*, 196: 193-213.
- Zhang, F., L. P. Wang, M. Brauner, J. F. Liewald, K. Kay, N. Watzke, P. G. Wood, E. Bamberg, G. Nagel, A. Gottschalk, and K. Deisseroth. 2007. 'Multimodal fast optical interrogation of neural circuitry', *Nature*, 446: 633-9.
- Zhang, J., K. Y. Zhang, L. B. Zhang, W. W. Zhang, H. Feng, Z. X. Yao, B. Hu, and H. Chen. 2019. 'A method for combining multiple-units readout of optogenetic control with natural stimulation-evoked eyeblink conditioning in freely-moving mice', *Sci Rep*, 9: 1857.
- Zhou, W., P. Yan, J. P. Wuskell, L. M. Loew, and S. D. Antic. 2007. 'Intracellular long-wavelength voltage-sensitive dyes for studying the dynamics of action potentials in axons and thin dendrites', *Journal of Neuroscience Methods*, 164: 225-39.